Tampere University of Applied Sciences

Underbody Design for a Formula Student vehicle

Design Process & Analysis of TFS24 Underbody Concept

Samuli Harjula

BACHELOR'S THESIS
May 2024

Degree Programme in Mechanical Engineering
Product Development & Production Engineering

ABSTRACT

Tampereen ammattikorkeakoulu
Tampere University of Applied Sciences
Degree Programme in Mechanical Engineering
Product Development & Production Engineering

SAMULI HARJULA:
Underbody Design for a Formula Student Vehicle
Design Process and Analysis of TFS24 Underbody Concept

Bachelor's thesis 100 pages, appendices 6 pages
May 2024

The purpose of this thesis was the design and analysis of an underbody concept for the TFS24 prototype of Tampere Formula Student motorsports team. The main goals for the underbody were to increase the total downforce generated and to move the aerodynamic balance closer to the rear axle of the vehicle, compared to the previous prototype. The active aerodynamics with thrusters were studied and an option to implement active underbody in the future was considered during the design.

The aerodynamic design was done iteratively using computational fluid dynamics, consisting of over a hundred simulations in total. The iterations were analysed both numerically and visually and the results were evaluated using lap-time simulations.

The underbody concept achieved a 47% increase in downforce and a 39% improvement in its centre of pressure. These improvements decreased the simulated lap times of the vehicle, therefore increasing the potential placings in the competitions.

Several areas for development can be obtained from the results, including further optimising performance and the centre of pressure of the underbody and manufacturability aspects. The preliminary studies of active aerodynamics indicated significant improvements in performance and more detailed studies should be performed for harnessing its full potential.

Key words: aerodynamics, ground effect, underbody, downforce, tampere formula student, CFD

ACKNOWLEDGEMENTS

Firstly, I would like to acknowledge that none of this would be possible without the current members and active alumni of Tampere Formula Student, who drive the success and continuous development of the team. Thanks to this team, I have been able to prepare myself well for the challenges that await me as an engineer. This team has provided me with a comprehensive experience regarding vehicle performance. The enthusiastic approach of the team members for motorsport has been truly encouraging.

Special thanks to Jussi Mononen and Arttu Vihavainen for their extensive careers and valuable guidance for the team during all these years. Additionally, I would like to thank my family and closest ones for their support during my studies and the never-ending days with the formula.

Tampere 14.5.2024.

Samuli Harjula

CONTENTS

ABBREVIATIONS AND TERMS

Aero balance	Aerodynamic Balance
Aero package	Aerodynamic Package
AoA	Angle of Attack
CAD	Computer Aided Design
CNC	Computer Numerical Control
EDF	Electric Ducted Fan
FMECA	Failure Mode, Effects, and Criticality Analysis
NACA	National Advisory Committee for Aeronautics
PLA	Polylactic Acid
SST	Shear Stress Transport
SWOT	Strengths, Weaknesses, Opportunities, Threats
TFS	Tampere Formula Student
UB	Underbody

1 INTRODUCTION

This Bachelor's thesis reviews design process of a ground effect underbody, which is to be implemented to Tampere Formula Student's season 2024 prototype vehicle, nicknamed TFS24. Some subjects and details have been excluded due to the ongoing development of the prototype.

Design process consists of project planning, concepting, aerodynamic design with computational fluid dynamics and mechanical design of the final product. Additionally, active aerodynamics are studied briefly. Mechanical design consists of structural models and assemblies, their mountings, as well as mould design. Results and performance of the underbody are evaluated using lap time simulations. Areas for development are discussed, regarding both aerodynamic and mechanical design.

1.1 Formula student series

Formula student is a series consisting of university level student teams competing against other universities in international design competitions. Teams design, manufacture, test and compete with a single seated formula style prototype car. The ultimate purpose of the series is to improve the qualifications of students in a comprehensive project which combines theoretical and practical studies. (Formula Student Germany n.d.)

Points are gained in two disciplines in competitions, dynamic and static events. Dynamic events are evaluated by vehicle performance on track, regarding maximum longitudinal and lateral acceleration, efficiency, endurance, and overall race performance.

Assessment areas in static events include project management, technical understanding, financial planning, and so-called good engineering practices (Formula Student Germany n.d). Scoring varies between combustion and electric and

driverless classes. Points available in each event are presented in table 1, regarding competitions without driverless class.

TABLE 1. Competition scoring.

Discipline		Maximum points
Static	Business Plan	75
	Cost and Manufacturing	100
	Engineering Design	150
Dynamic	Acceleration	75
	Skid Pad	75
	Autocross	100
	Endurance	325
	Efficiency	100
	Overall	1000

In the Business Plan event, a team presents a fictious business idea related to the constructed prototype. Business model is evaluated by its credibility, structure, and delivery performance. Cost and Manufacturing event evaluates team's understanding of the prototype cost structure and management, mass production and prototyping considerations and trade-offs. Engineering Design event evaluates team's general technical knowledge, detailed understanding of race car design and design choices regarding the prototype.

The Acceleration event evaluates prototype's longitudinal acceleration over 75 metres, from a standstill position. The Skid Pad event includes a figure of eight circuit, which tests both vehicle's maximum longitudinal and lateral acceleration. The Autocross event is scored by the fastest individual lap time on a one-kilometre track. The Endurance event is the main single discipline in competitions. The Endurance event tests vehicle's reliability over 22 kilometres, including a driver change at the halfway point. Maximum points are awarded by the smallest elapsed time. The Efficiency event is performed simultaneously with the Endurance event, gauging the fuel and energy consumption relative to the elapsed Endurance time.

1.2 Tampere Formula Student team

Tampere Formula Student is a team which consists of students from both Tampere University of Applied Sciences and Tampere University. The team was founded 2006, when the association TAMK Formula Student Ry was also registered. First prototype was published in 2008 and the team has continued to develop and manufacture prototypes to compete in the series ever since.

1.3 Aerodynamics in racing

Aerodynamics is an ever-evolving significant technology, which has played a major role in racing for decades. At the early 1900s, drag reduction was a primary concern in race car aerodynamics. Larger scale aerodynamic experimentations started at the late 1960s, leading to aerodynamic underbodies and implementation of front and rear wings. (Katz 1995, I).

Nowadays, aerodynamics in racing consists of complex systems, with goals of increasing downforce, reducing drag, improving cooling, optimizing engine air intake, and adjusting vehicle's stability and aerodynamic balance in different driving situations.

2 THEORY

This section focuses on the basics of the vehicle performance, aerodynamics, and computational fluid dynamics, before proceeding to the underbody project plan and its design processes.

2.1 Vehicle performance

Vehicle performance describes a vehicle's ability to complete given course in a minimum time (Milliken & Milliken 1995, 3). Vehicle performance is about both the interaction between vehicle's subsystems and the interaction between a driver and the vehicle. An important principle of circuit racing is that "the velocity should never be constant, unless held arbitrarily for reasons of endurance, traffic, or safety, or limited by the maximum speed of the vehicle" (Milliken & Milliken 1995, 4). Thus, a driver should always accelerate at maximum rate until a turn, when the speed should be decelerated at maximum rate. After the turn, a driver should then accelerate again until the next turn.

For the vehicle to gain high accelerations while maintaining the given course, one must be supported by a capable powertrain to overcome the mass and aerodynamic drag, proper suspension geometry and setup to offer suitable handling during cornering and altitude changes and efficient aerodynamic package to reduce drag and to increase downforce to enhance tires' friction coefficient. Additionally, all these subsystems should be working seamlessly together to achieve the maximum potential of vehicle's performance.

2.2 Tire behaviour

Tires transmit all the forces generated by accelerating, cornering, braking, and aerodynamic forces excluding drag, to the ground. Therefore, understanding the basics of tire behaviour is indeed important when designing any components interacting with motion and forces.

As tires are flexible material, when a normal force, F_z, and side force, F_x *(action)*, are simultaneously applied to a tire standing on the ground, deformation of length Δx occurs. This can be seen in figure 1.

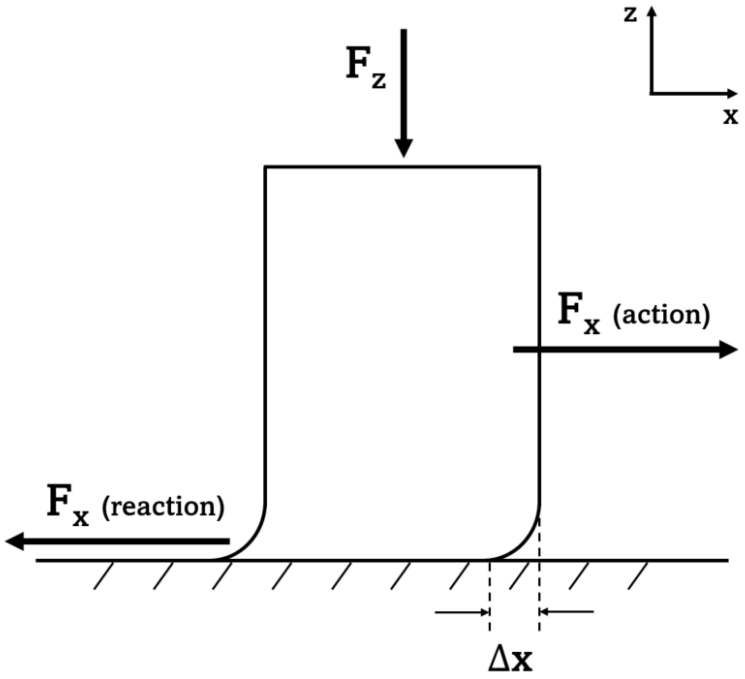

FIGURE 1. The relation between force and deformation (Katz 1995, edited).

As can be seen in the figure 2 below, deformation and resulting force increase linearly until with higher values of deformation, sliding results.

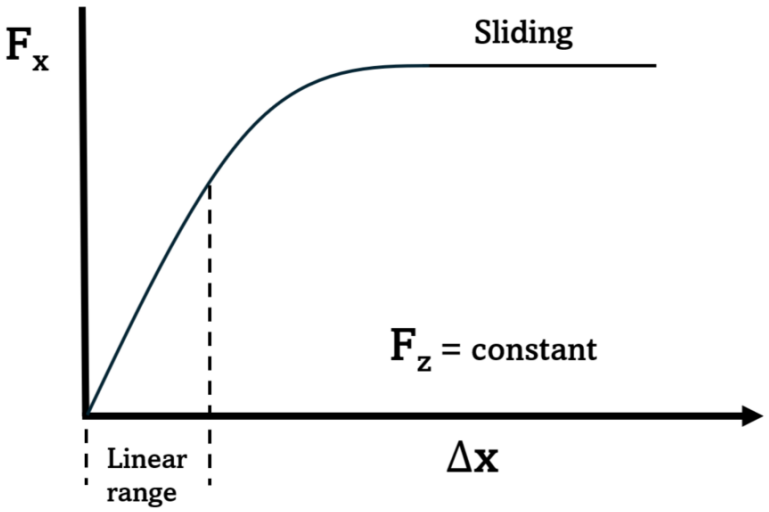

FIGURE 2. Linear deformation range and sliding (Katz 1995, edited).

A braking coefficient, μ, the ratio between the normal force and the force aligned with the vehicle's latitudinal axis is calculated as follows:

$$\mu = \frac{F_x}{F_z} \tag{1}$$

A cornering force coefficient, also μ, which describes the ratio between the normal force and the force aligned with the longitudinal axis, is calculated similarly with replacing F_x with F_y from the equation 1. These ratios resemble a commonly used friction coefficient, μ_{max}, which is the ratio between the normal force and the maximum sliding force.

As can be concluded from the equations of these coefficients, there must be some amount of deformation and slip in order for the tires to generate forces. Slip describes the difference between the velocity of the tire and the road. Additionally, during cornering the slip creates side forces, which leads to a difference between direction of heading and the actual direction of travel. This difference is described by the slip angle, β. This slip and thus the slip angle can be manipulated by changing the amount of normal force on the tire, which is visually represented in the figure 3.

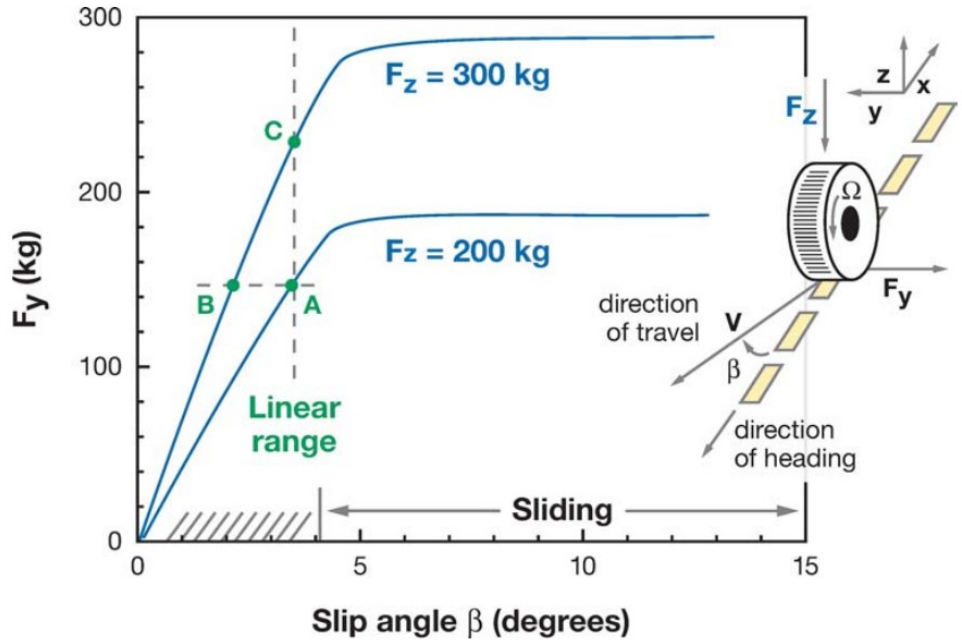

FIGURE 3. Effect of the normal force on slip angle (Katz 2006, 29).

2.3 Aerodynamics

Aerodynamics is a study of air flows surrounding objects, and the resulting motion and forces induced by these. Aerodynamic forces studied in this thesis are focused on negative lift, also known as downforce, and drag.

Aerodynamic loads significantly affect on vehicle's performance in several areas, including air resistance, braking, handling, and stability. As was presented earlier, altering the normal force on tyres affects to the vehicle's grip. Figure 4 demonstrates importance of aerodynamic downforce on vehicle's performance.

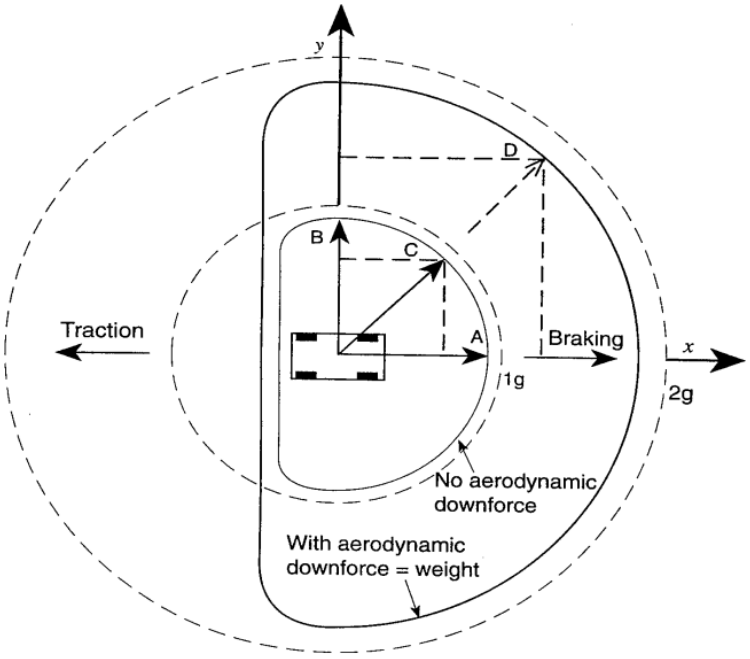

FIGURE 4. Effect of aerodynamic downforce on a tire's maximum performance (Katz 1995, 151).

2.3.1 Bernoulli's principle

A relationship between velocity and pressure in a fluid can be presented by Bernoulli's principle. In an incompressible flow, the Bernoulli's equation (2) can be formed as

$$P_1 + \frac{1}{2}\rho v_1^2 + \rho g h_1 = P_2 + \frac{1}{2}\rho v_2^2 + \rho g h_2 \quad (2)$$

Where:

P = Static pressure at given point (Pa)

ρ = Fluid density (kg/m^3)

v = Flow velocity at given point (m/s)

g = Gravitational acceleration (m/s^2)

h = Elevation of the point above a reference plane (m).

This equation can be divided into three terms shown in the figure 5 below.

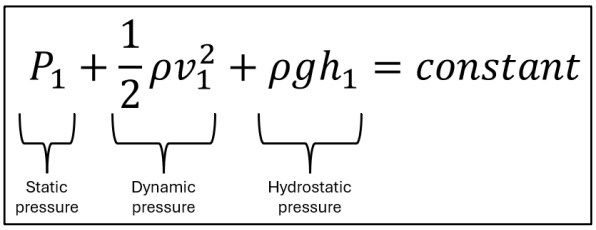

FIGURE 5. Terms of the Bernoulli's equation.

The right side of the equation can be interpreted as constant as well as the fluid density. Additionally, in race car aerodynamics, the hydrostatic pressure is negligible. Therefore, if velocity is increased, the pressure must decrease and vice versa.

When observing a fluid flowing through pipe with a constant density and no energy added nor removed from the system, the mass flow must be the same in any position of the pipe. Thus, a continuity equation (3) can be constructed as

$$v_1 A_1 = v_2 A_2 \tag{3}$$

Where:

v = velocity (m/s)

A = cross-section area (m^2).

If the cross-section varies along the pipe described above, the velocity must compensate. The pipe concerned in the figure 6. As the cross-section decreases, the

flow velocity must increase, therefore decreasing the pressure, regarding to the Bernoulli's equation (2).

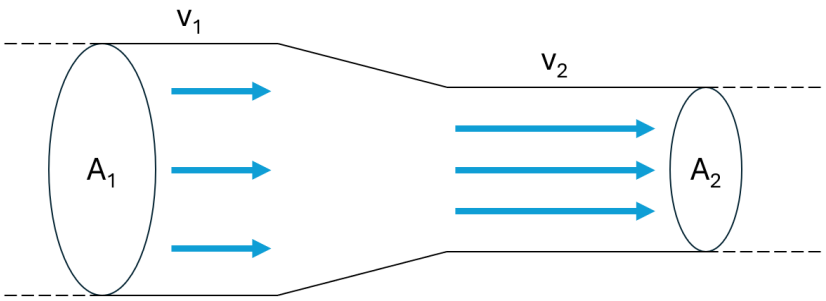

FIGURE 6. Constant density flow through pipe.

2.3.2 Boundary layer

The viscosity of a fluid, air, in this case, generates shear forces when moving along a surface of an object. Immediately after the flow interacts with the surface, a zero-velocity condition develops on the surface, also known as no-slip condition. The flow velocity recovers gradually to the free-stream velocity as the distance from the surface increases. This layer affected by no-slip condition is known as boundary layer. As the flow travels along the surface, thickness of the boundary layer increases. Figure 7 shows a uniform free-stream velocity and a simplified boundary layer formed on a flat surface (Bernard 2015, 20).

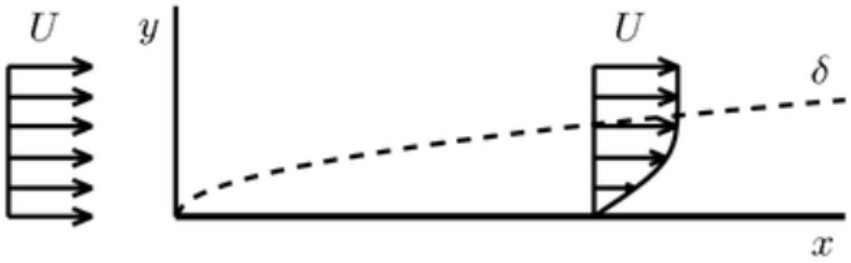

FIGURE 7. Boundary layer on a flat plate (Bernard, 2015).

This uniform flow, with all fluid particles travelling to same direction, is called laminar flow. Eventually, several instabilities in the flow will occur, which is called turbulent flow. This transition from laminar to turbulent flow occurs after traveling

a certain distance downstream or with high flow velocities, shown in figure 8. (Forster 2021.)

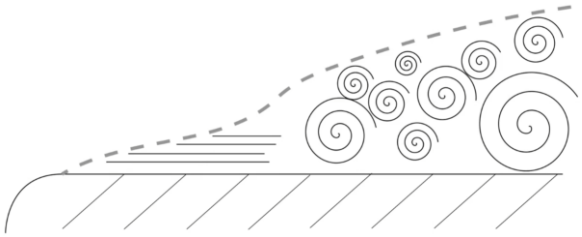

FIGURE 8. Boundary layer transition from laminar to turbulent (Forster, 2021).

Turbulent boundary layers will induce more skin friction drag than a laminar boundary layer. However, a turbulent boundary layer has more turbulent energy due to its swirling characteristics, thus having ability to attach to a surface for a longer distance than a laminar boundary layer, which is crucial to aerodynamic efficiency and performance. (Forster 2021.)

2.4 Aerofoil characteristics

Aerofoils are two-dimensional sections of wings, shaped to generate lift or to manipulate surrounding airflow for other purposes, such as feeding airflow to other components for improving aerodynamic efficiency, cooling, and for a drag and stability control.

The main parameters for defining geometry of an aerofoil are visually presented in figure 9 below. For the given aerofoil to generate negative lift, downforce, one would be inverted by its chord line.

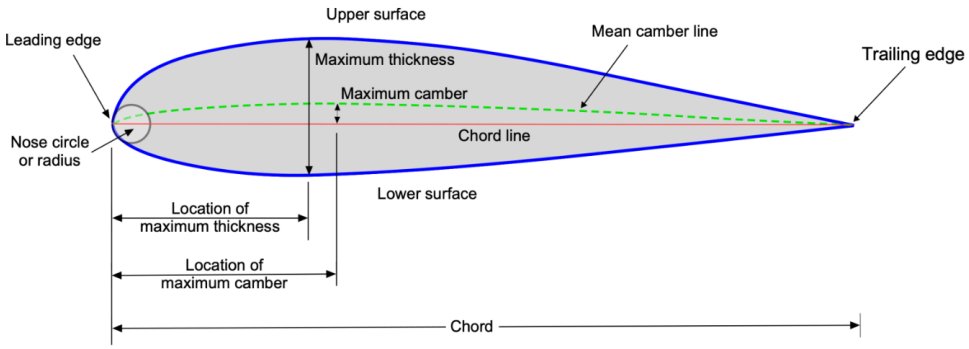

FIGURE 9. Main geometric parameters of an aerofoil (Leishman, 2024).

2.4.1 Circulation and lift generation

Contribution of circulation in lift generation can be presented by the flow pattern around a spinning cylinder. Figure 10 shows a non-spinning case on the left and a spinning case on the right. U is the free-stream velocity, S_1 and S_2 are front and rear stagnation points, Γ is the circulation, a is the velocity ratio and L is the lift.

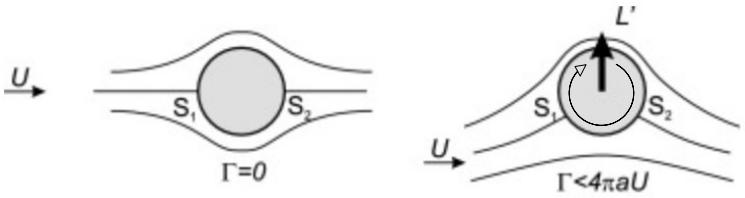

FIGURE 10. The flow pattern around a spinning cylinder (Houghton, Carpenter, Collicott & Valentine, 2015, edited).

As Γ increases, the stagnation points move down below the horizontal axis, velocity of the bottom streamline decreases and velocity of the top streamline increases. As previously discussed, velocity and pressure around the cylinder are proportional to each other. High pressure is located at the bottom of the cylinder and low pressure at the top. This pressure difference induces a pressure force, the lift, at the top side of the cylinder.

Circulation around an aerofoil generates lift similarly to a spinning cylinder described above. However, when a wing is accelerated from the rest, the circulation is not produced instantaneously. Thus, the lift generated by the wing starts from zero as well. Figure 11 presents streamlines of the flow immediately after the wing is accelerated.

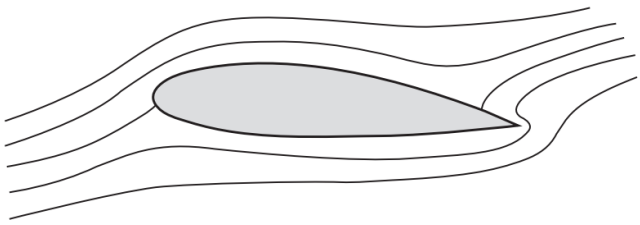

FIGURE 11. Streamlines around an aerofoil with zero circulation (Houghton & others, 2013).

The airflow at the sharp trailing edge is forced to change its direction suddenly, which results in stagnation point occurring on the upper surface. This stagnation point induces high accelerations. Significant viscous forces are produced due to these accelerations and a so-called starting vortex is generated above the trailing edge. The stagnation point moves toward the trailing edge as the circulation increases, therefore increasing the lift generated by the wing. (Houghton & others 2013, 270). The airflow around an aerofoil developed to a full circulation is shown in figure 12. This phase of circulation is also known as the Kutta Condition.

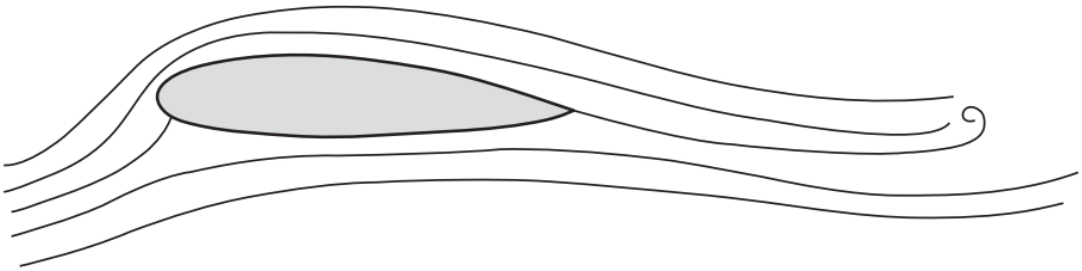

FIGURE 12. Streamlines around an aerofoil, with a full circulation (Houghton & others, 2013).

2.4.2 Wing performance

Several coefficients are used universally for analysing and comparing the performance of an aerodynamic component or system. Lift coefficient, C_L, is calculated by (4)

$$C_L = \frac{2L}{\rho v^2} \tag{4}$$

Where L is the lift force, ρ is the fluid density, and v is the flow speed. Drag coefficient, C_D, is calculated using similar equation by replacing lift force with a drag force. Lift coefficient by area, C_{LA}, is calculated by (5)

$$C_{LA} = \frac{2L}{\rho v^2 A} \tag{5}$$

Where *A* is the relevant reference area. The area can be specified as effective aerodynamic area, such as total area of wings, the frontal area of the vehicle, or other relevant value.

Angle of attack describes the angle between the chord and the direction of a free-stream velocity. Increasing the angle of attack of a wing increases its lift and drag generation. Pressure areas for low and high angles of attack are shown in figure 13.

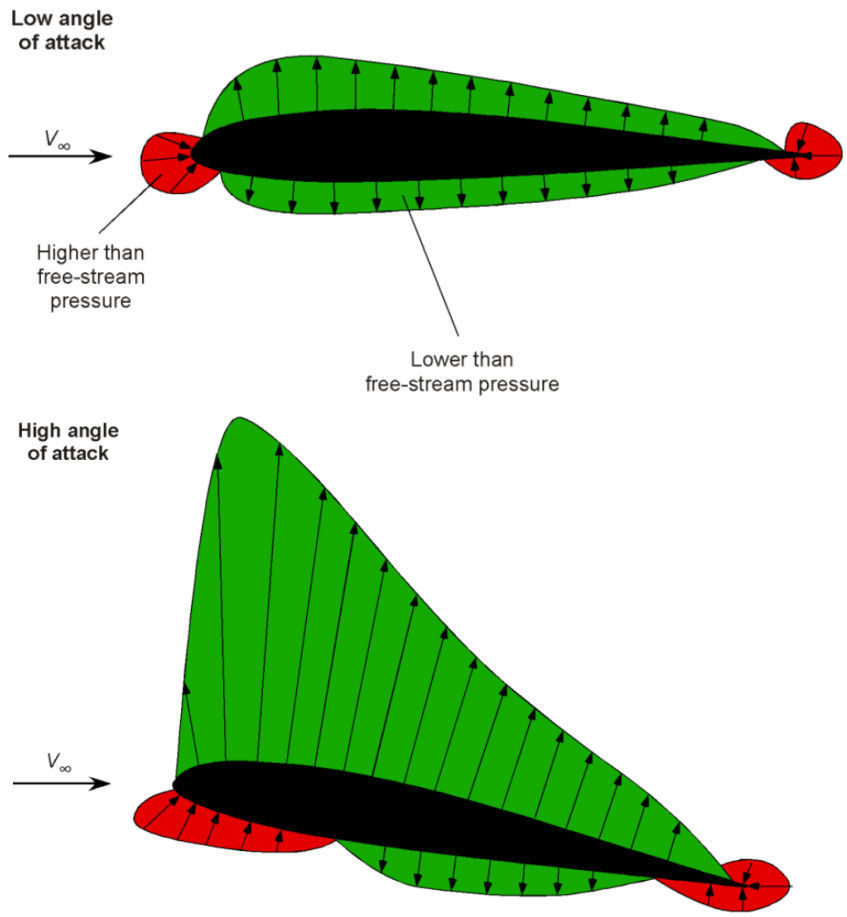

FIGURE 13. Pressure distributions around an aerofoil with low and high angle of attack (Leishman 2024, edited).

Despite the increase in drag, the overall performance and efficiency can be improved up to certain point where flow separation occurs. The development of flow separation is presented in figure 14. The onset of this flow separation is called stall or stalling. After the flow separation has started, a major increase in drag occurs. Additionally, as the flow separation increases, complexity and

irregularities of the vortices increase as well, making it challenging to anticipate and control.

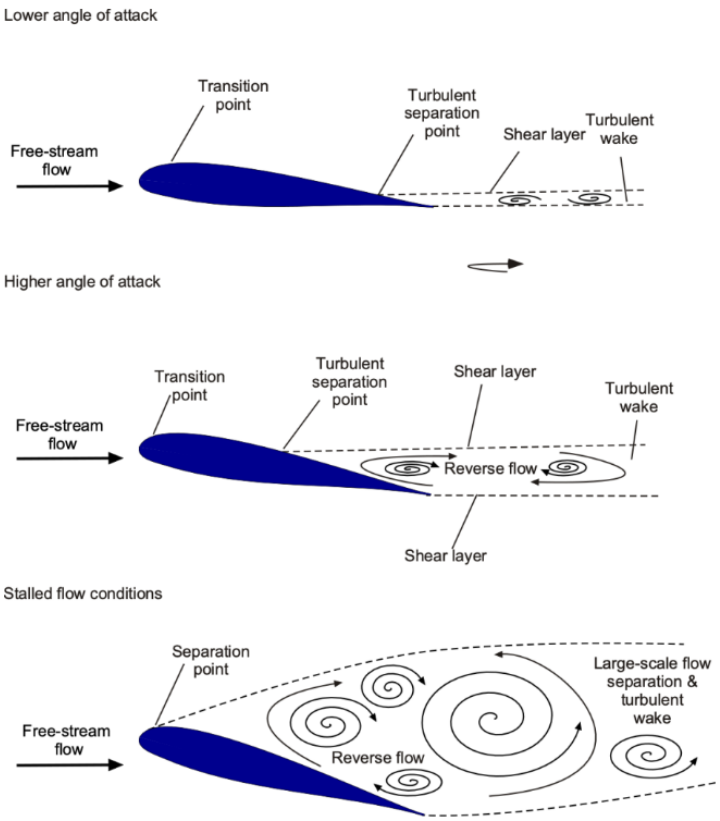

FIGURE 14. Development of flow separation (Leishman 2024, edited).

Altering geometric properties, of an aerofoil manipulate pressure distribution, therefore changing maximum values of lift and drag, stability and sensitivity. Cambered aerofoils generate lift even with zero angle of attack, where symmetric aerofoils generate zero lift.

2.4.3 Wing performance enhancement

Despite the high lift generation characteristics of a wing, efficiency of wings with small aspect ratio is often undesirably low in race cars. Aspect ratio describes the ratio between wingspan and chord, span measuring the distance between wing tip to its root, or alternatively the distance from wing tip to tip.

Due to major pressure differences between upper and lower surface of a wing, air tends to spill from high pressure to low pressure side, mixing and balancing these pressure regions, therefore generating so-called wingtip, or trailing vortices, drastically reducing efficiency of the wing, and increasing drag. This behaviour can be reduced and partially prevented by adding endplates to the wing sides.

Gurney flap is a thin sheet part located at the trailing edge of the wing, most commonly perpendicular to the chord line of the wing. The gurney flap generates counter-rotating vortices behind it, due to the extreme changes in contour for the flow to follow. These vortices delay the flow separation near the trailing edge, improving the suction (Wang, 2008). With gurney flap, higher angles of attack can be obtained before stall occurs. Effect on flow patterns with a gurney flap is shown in figure 15.

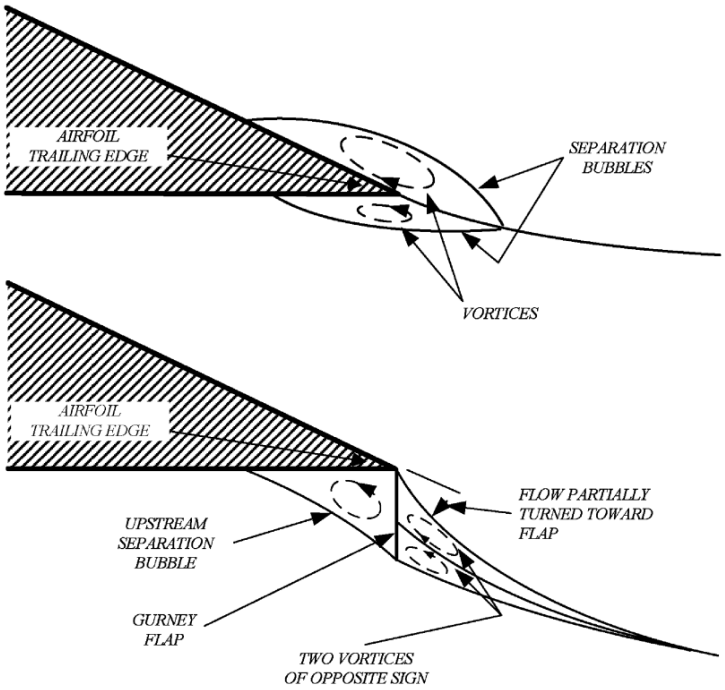

FIGURE 15. Flow patterns with and without the Gurney flap (Wang, 2008).

Increasing the height of the flap, up to 5% of the chord length in some cases, can increase downforce (Katz 2006, 41).

To improve flow attachment of a wing with high angles of attack, rear section of one can be divided into multiple separate smaller wings. This allows the high

energy free-stream flow to pass through the slots, energizing boundary layer, therefore improving flow attachment (Forster, 2015). Streamlines and pressure contours of a wing consisting of four elements, obtained from CFD results, are shown in figure 16.

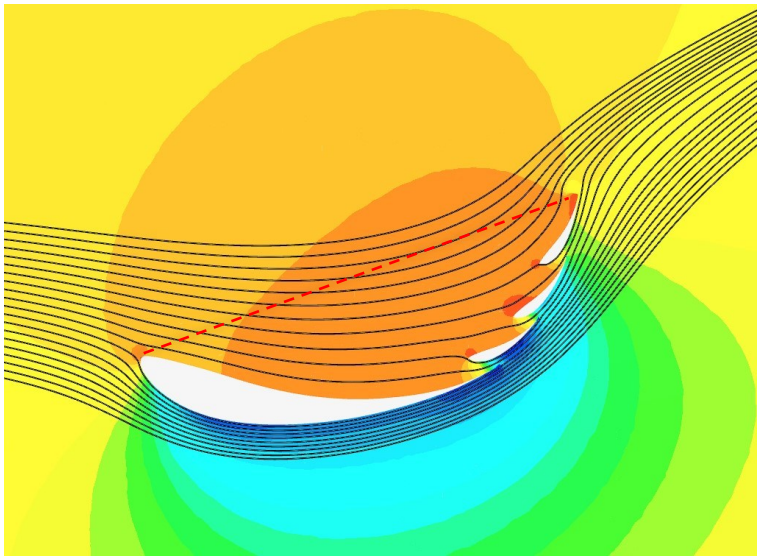

FIGURE 16. CFD results of streamlines and pressure contours of a four-element wing, from TFS24 design phase.

Pressure scale is defined from lower to higher pressure, from blue to red. Streamlines are in black and the red dotted line represents corresponding angle of attack and chord of the wing. The gurney flap on the fourth profile acts as described earlier. Such multi element wing allows higher angles of attack with reduced stall and to manipulate airflow to follow more aggressive camber.

2.5 Ground effect

Ground effect in a race car aspect, is a phenomenon, in which the performance of a wing is increased as the ground clearance decreases, which is related to Bernoulli's principle. This complies, until there is no more sufficient amount of mass flow under the wing, therefore reducing the amount of kinetic energy, which energizes the boundary layer and improves flow attachment on the wing surface.

Typical aerodynamic results for an inverted wing near ground plane is presented in figure 17, including the stall point below 0.1 clearance.

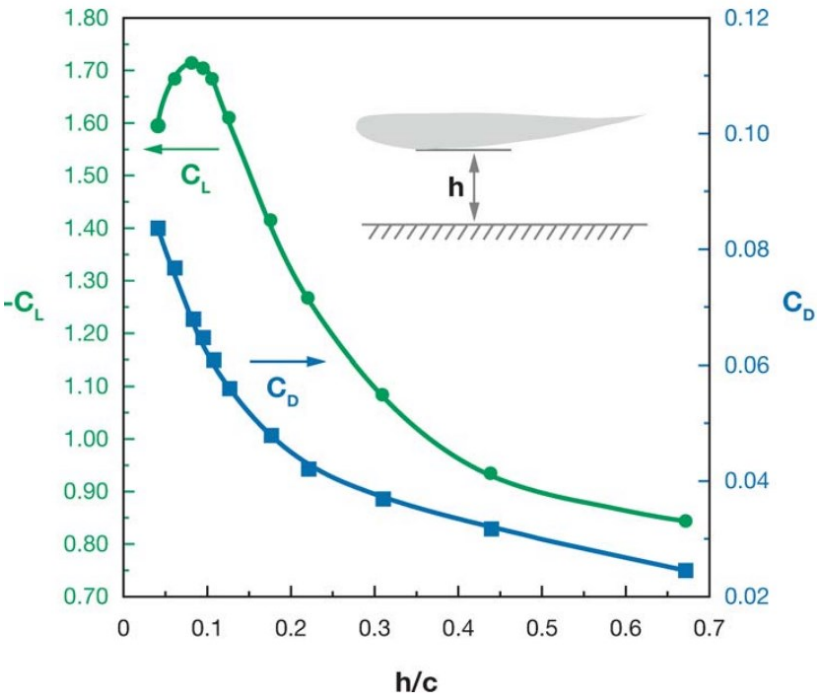

FIGURE 17. Downforce and drag coefficients versus ground clearance for a LS(1)-0413 aerofoil (Katz, 2006).

Additionally, aerodynamic components located in regions of disturbed airflow, so-called dirty air, are more likely to stall in small ground clearances than components in undisturbed flow. This difference is due to thinner boundary layer in undisturbed flows. Main sources of these disturbances are vehicle's body and its rotating wheels. (Katz 2006, 170.) The main aerodynamic contribution of wheels is indeed drag, which comprises approximately 40% of the total drag of a car (Zhang, X. & Toet, W. & Zerihan, J. 2006, 34). Regions of disturbed air induced by tires, tire wake, is crucial in underbody efficiency and overall performance.

According to Zhang & others (2006), due to ride height sensitivity of an underbody and a diffuser, undulations in the racetrack may cause fluctuations in downforce, resulting in car instabilities and affecting its performance. This matter should be considered when adjusting ride heights and suspension setups as well as front wing performance, as it feeds the intake air to underbody. (Zhang, X. & others 2006, 40.)

2.5.1 Diffuser

A Diffuser is a device which recovers the exit-pressure close to freestream velocity at the rear of a race car, after the underbody section. This is implemented by increasing cross-sectional using a diverging ramp. Ramp of the diffuser creates a negative camber effect to the vehicle's body, increasing the downforce generated by the underbody and as the flow of an underbody recovers to ambient pressure, drag induced by one is reduced as well, compared to a flat floor underbody without diffuser. Even though increase in downforce always induces drag, the lowest drag penalty can be achieved using underbody with a diffuser, compared to front and rear wings. (Ehirim, O. & Knowles K. & Saddington A. 2019, 1-2.) The basic geometry of an internal flow diffuser is shown in figure 18.

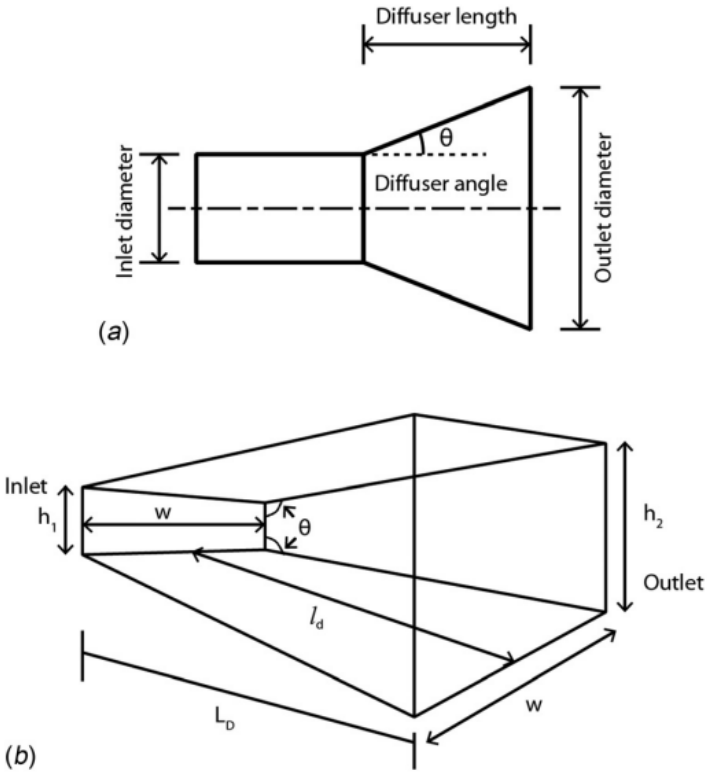

FIGURE 18. The basic geometry of (a) two-dimensional conical and (b) three-dimensional plane-wall diffuser (Ehirim, O. & others. 2019).

Experience with wind tunnel design has shown that diffuser section angles exceeding 10° will cause flow separation and random turbulence (Milliken & Milliken 1995, 100).

2.5.2 Barge boards and vortex generators

There are several methods for controlling tire wake, from simple plates and vanes to complex wing assemblies. Barge boards or turning vanes, are vertical plates mounted between front wheels and chassis, designed to control tire wake and to obtain cleaner flow from the front wing to the underbody. Barge boards can also be used for feeding air to the sidepods and to turn the tire wake away from the aerodynamic components on the chassis. (Formula 1 dictionary, n.d.)

Vortex generators in race cars, later referred as “VG’s”, are strakes designed for boundary layer transition and flow separation control. As the flow passes the edge of a strake, the sudden change in path to follow induces vortices behind it. Height of a small-scale VG is similar to height of a boundary layer concerned, whereas large-scale VGs are intended to manipulate the outer flow, instead of the boundary layer. (Katz & Morey 2008, 1.) These are visualized in figure 19 below.

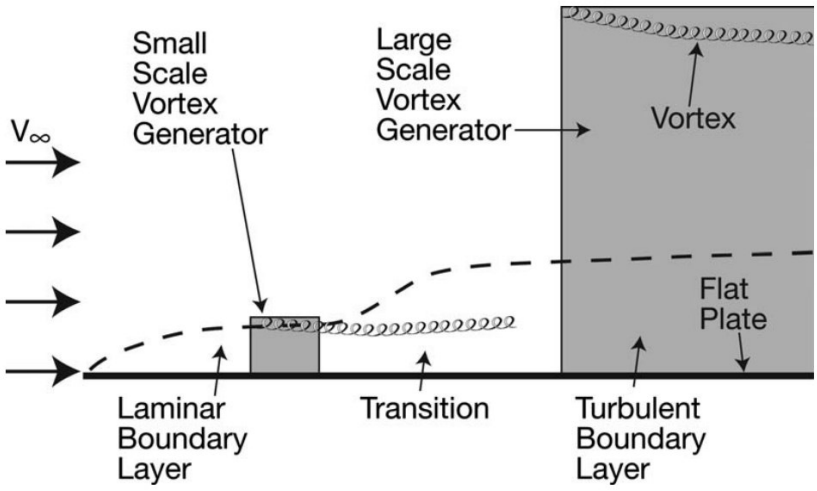

FIGURE 19. Large- and small-scale vortex generators (Katz & Morey, 2008).

Small-scale VGs can be placed before boundary layer transition points to prevent flow separation and to force transition from a laminar to a turbulent boundary layer. Alternatively, these VGs can be placed in a turbulent layer to energize one and to delay the onset of separation (Katz & Morey 2008, 1). Large-scale VGs are designed to create stable long-tip vortices to reduce the pressure along their

trail. These long vortices can improve the suction under the vehicle (Katz 2006, 47). In most cases, at least two VG plates per side are required to stabilize the vortex (Katz & Morey 2008, 2). An example of large scale VGs, placed at the front of an underbody is shown in picture 1.

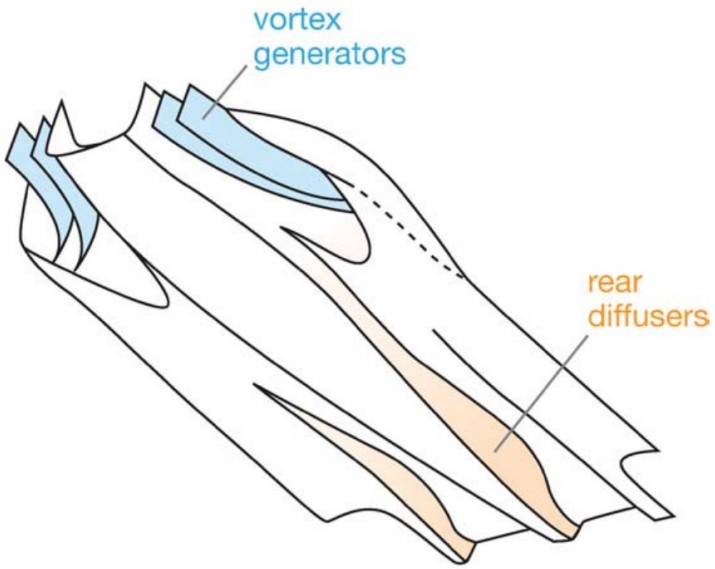

PICTURE 1. A typical 2000's Indy car underbody with vortex generators (Katz, 2006).

2.5.3 Vortex sealing

As explained earlier, wheels are a major factor in creating dirty air around the body. Additionally, as an underbody of a race car has a potential to produce significant amount of downforce with a low drag penalty, it's beneficial to maintain the effective area of the aerodynamic underbody relatively high. Simultaneously, performance of an underbody is often disturbed by the tire squirt from rotating front wheels.

Like wings, vertical walls of a diffuser create vortices due to pressure differences as well. Due to ground proximity of a diffuser, these vortices partially prevent dirty air from bleeding to the low-pressure region inside the diffuser. However, strong tire squirts can enter through such flow region. In this case, dividing diffuser to sections by adding vertical fins inside can captivate the disturbed flow to conserve performance on inner parts of the diffuser (Forster, 2015). Effect of the additional

fin is shown in figure 20, in which green represent vortices induced by outer walls and inner fins, red arrows act as dirty air, blue arrows as high velocity flow and black as a diffuser geometry and symmetry.

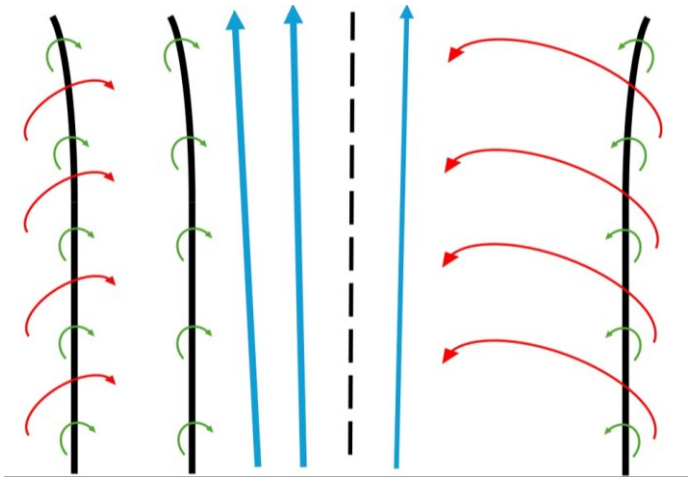

FIGURE 20. Top view of a diffuser with (left) and without (right) the additional fin.

By adding L-shaped extensions to vertical fins, location of a vortex core can be induced closer to the ground plane, thus improving the sealing effect (Forster, 2015). Vortex locations with L-shaped and straight diffuser is shown in figure 21.

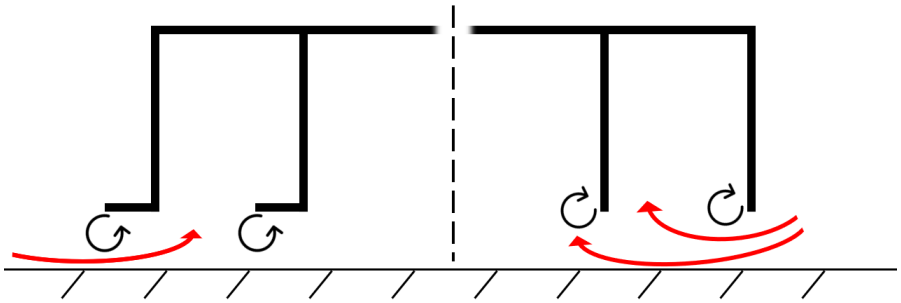

FIGURE 21. Rear view of a L-shaped (left) and straight diffuser.

2.5.4 Power ground effect

Active aerodynamic systems interacting in proximity to the ground, so-called power ground effect devices, can be used to significantly improve the performance of an underbody. Even though these devices are widely banned in

motorsports, Formula Student -class has yet to prohibit power ground effect. The most famous vehicle to implement power ground effect was Brabham BT46, also known as the “fan car”, designed by Gordon Murray (see picture 2).

PICTURE 2. Brabham BT46B (Somerfield, M. & Piola, G, 2020).

The fan car was equipped with a large fan driven from the gearbox, mounted at the rear to suck air from beneath the vehicle. The suction was enhanced with flexible skirts in contact with the ground. Brabham dominated in the Swedish GP in the 1978, driven by Niki Lauda. However, the fan car was forbidden immediately after. (Katz 1995, 247.)

2.6 Computational fluid dynamics

Computational fluid dynamics, CFD, refers to a numerical calculations and approximations of given physical case. CFD covers heat transfers, incompressible and compressible flows, internal and external flows, for example. Track testing and wind tunnel testing requires a great deal of resources, including either full scale model for track testing or accurate small-scale prototype for wind tunnel testing, as well as related environment and equipment. Therefore, CFD is an extremely valuable tool during the concepting and design phase of an aero package, due to cost-efficiency and relatively low calculation times.

Before running the analysis, a CAD-model is imported to the software and meshed to small elements. Several mesh refinements are required for more accurate calculations. After meshing the geometry, boundary conditions are defined for the problem and desired results are configured. Calculations are done iteratively as long as the accuracy of the iterations is at the desired level. Results can be then analysed numerically and visually in post processing.

Since CFD consists of highly complex equations and mathematical models regarding fluid dynamics and element methods, a detailed walkthrough of these was excluded from the scope of this thesis.

3 UNDERBODY PROJECT PLAN

A project plan for the underbody was created to maintain focus on essential tasks and to identify benefits and risks for the project from the team's point of view. The project plan was mainly created based on experience.

3.1 Starting point

Previous season's prototype, nicknamed TFS23 or "Saana", had a completely new aerodynamic package, visible in picture 3. The package included multi-element front wing assembly with three wings, rear wing assembly with four wings, inverted winglets on the front of the chassis and an underbody including single mid tunnel with diffuser and two side tunnels. TFS23 was the first one to implement a full sized underbody aerodynamics.

PICTURE 3. Render of TFS23.

Front and rear wing, sidepods, and the diffuser were equipped with quick-connectors and the underbody was bolted to the chassis. Winglets were bonded to

the chassis. However, the quick release of the rear wing was not ultimately functioning as designed at the time, due to additional components mounted between endplates. Aero package with other systems hidden is shown in picture 4.

PICTURE 4. Aerodynamic package of TFS23.

Saana's aerodynamic performance was multiplied compared to its predecessor according to CFD-simulations at the time. Nevertheless, track testing revealed significant differences in flow attachment between simulations and real-life test conditions. This was mostly due to extremely aggressive side tunnels and an inadequate boundary layer mesh in the CFD setup.

Numerical results of Saana's aero package with early and late simulation setups of TFS24 design phase are shown in table 2.

Table 2. Saana's CFD results, with early and late simulation setup.

Simulation setup	cL	cD	Underbody (N)
Early	4.37	1.46	194
Late	3.1	1.27	142

Velocity contours with the late setup are visible in picture 5. The flow starts to separate shortly after the choke point on side tunnels.

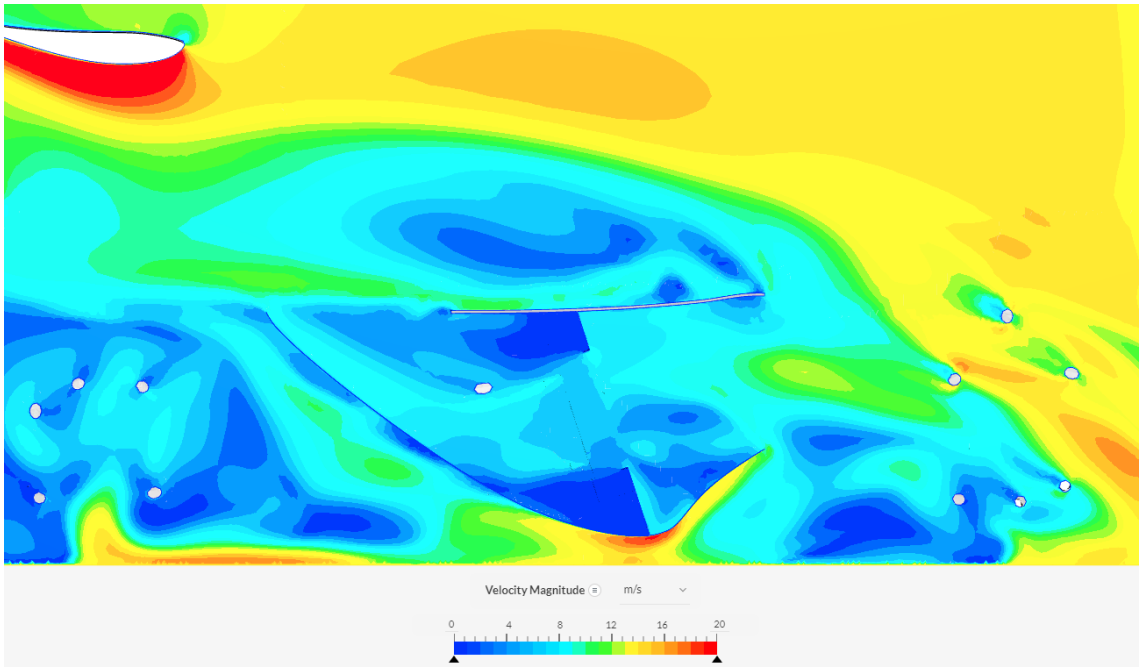

PICTURE 5. Saana's side tunnel velocity contours, late simulation setup.

Pressure contours of the Saana underbody are presented in picture 6. The mid tunnel and the diffuser section are both narrow and lacking in performance.

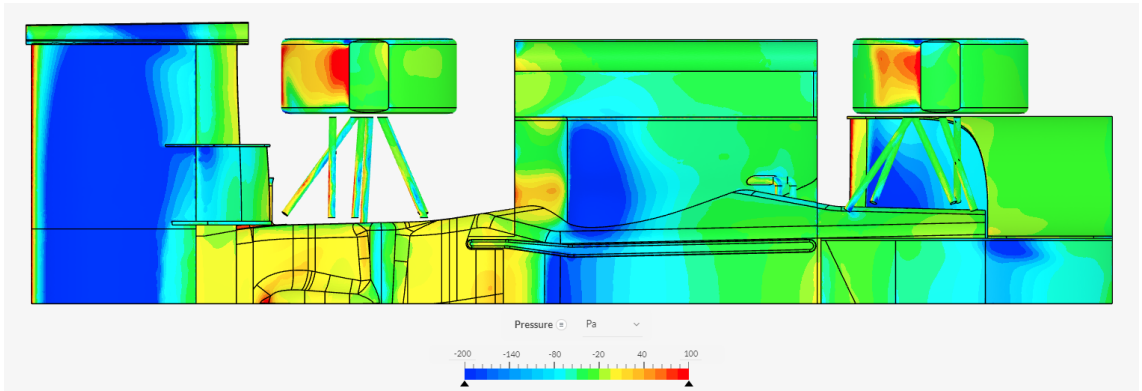

PICTURE 6. Saana's underbody pressure contours, late simulation setup.

3.2 Goals

Goals of the underbody project were obtained by experience, track testing, and feedback from the design judges from the 2023 season.

Goals & benefits for the underbody project were described as:

- Attached flow through entire length.
- Better rear wing performance.
- Aero balance of 60% at the rear axle.
- Mor stable driving experience.

Optional goals & benefits were added as well, regarding the power ground effect:

- Power ground effect to boost the performance of the underbody.
- Better efficiency
- More central/rearwards aero balance.
- Option to implement power ground effect to underbody geometry.
    - Reduces manufacturing costs if implemented in the future.

3.3 Project scope

Project scope was determined to avoid excess workload and to focus on relevant subjects of the project.

Project scope, in:

- Mechanical design
    - CFD-simulations
    - Mountings
    - Layup design
    - Mould design
- Electrical design (Optional)

    - Power ground implementation.

Project scope, out:

- Automatic aero balance control through power ground
- Self-designed thrusters
- Wind tunnel testing.

3.4 Resources & limitations

Resources for the project consisted of team members and budget available.

Resources:

- Mechanical designer
    - Concepting and design guidelines
    - Mechanical and aerodynamic design
    - Power ground effect design (optional)
    - High workload
- Electrical engineer (optional)
    - Electrical calculations
    - Wiring harness and controls of the power ground effect
    - Medium workload
- Manufacturing
    - 1500-3000€ (From low to high performance)
    - Mould
    - CFRP materials
    - Electrical components

Limitations of the underbody design were mainly determined by the official rules of Formula Student Germany. As the formula student vehicle must be open-wheeled, the wheel assembly must be unobstructed when viewed from the side. Additional restrictions around tires are visible in figure 22. Restrictions are shown in a case of steering being straight ahead. The minimum static ground clearance

of 30mm must be fulfilled with a driver sitting in the car. (Formula Student Germany 2024, 26).

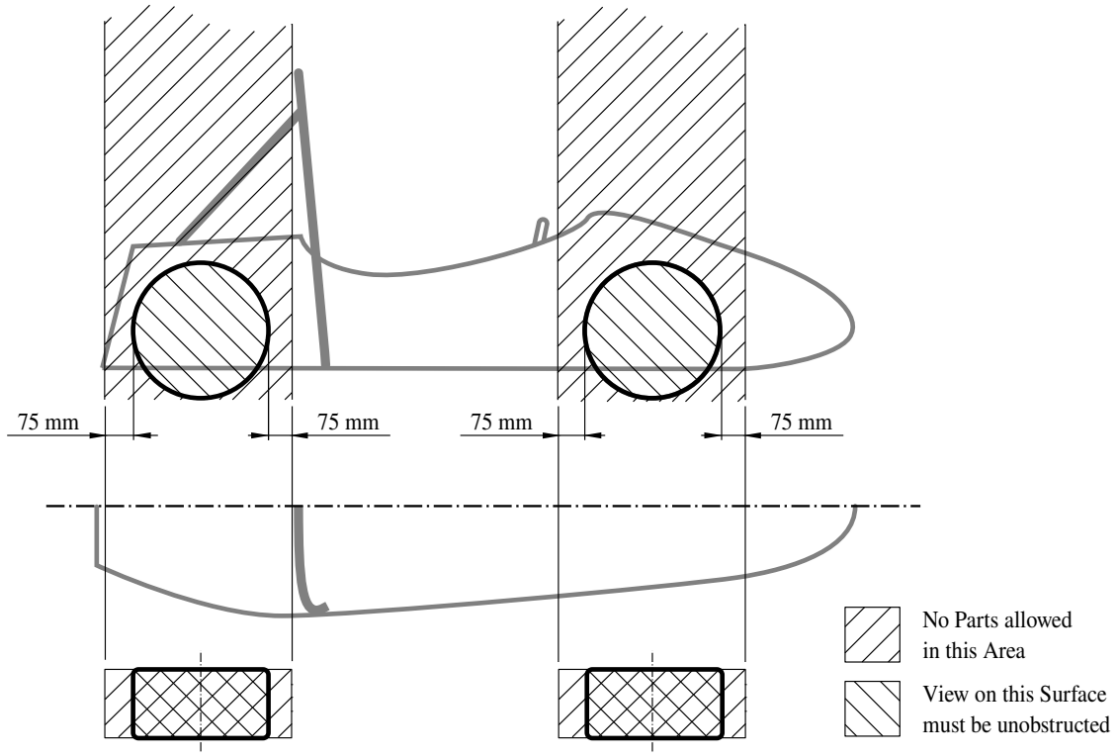

FIGURE 22. Keep-out-zones for the definition of an open-wheeled vehicle (Formula Student Germany, 2024).

Rules have several notes about the bodywork, regarding good engineering practices and safety issues. Two venting holes of minimum 25 mm diameter are required in the lowest part of any structure between the chassis and the ground, for preventing any accumulation of leaks.

Any bodywork facing forwards with tangency above 45° located in front of front wheels, must have minimum 38mm radius in all sides. Any forward-facing edge of bodywork or aerodynamic devices must have a minimum radius of 3 mm if a pedestrian may get in contact with one. (Formula Student Germany 2024, 27.)

Aerodynamic components defined by the rules are devices specially designed to guide the airflow around the vehicle, aiming to increase the downforce and/or lower the drag.

Restrictions for aerodynamic devices are shown in figure 23.

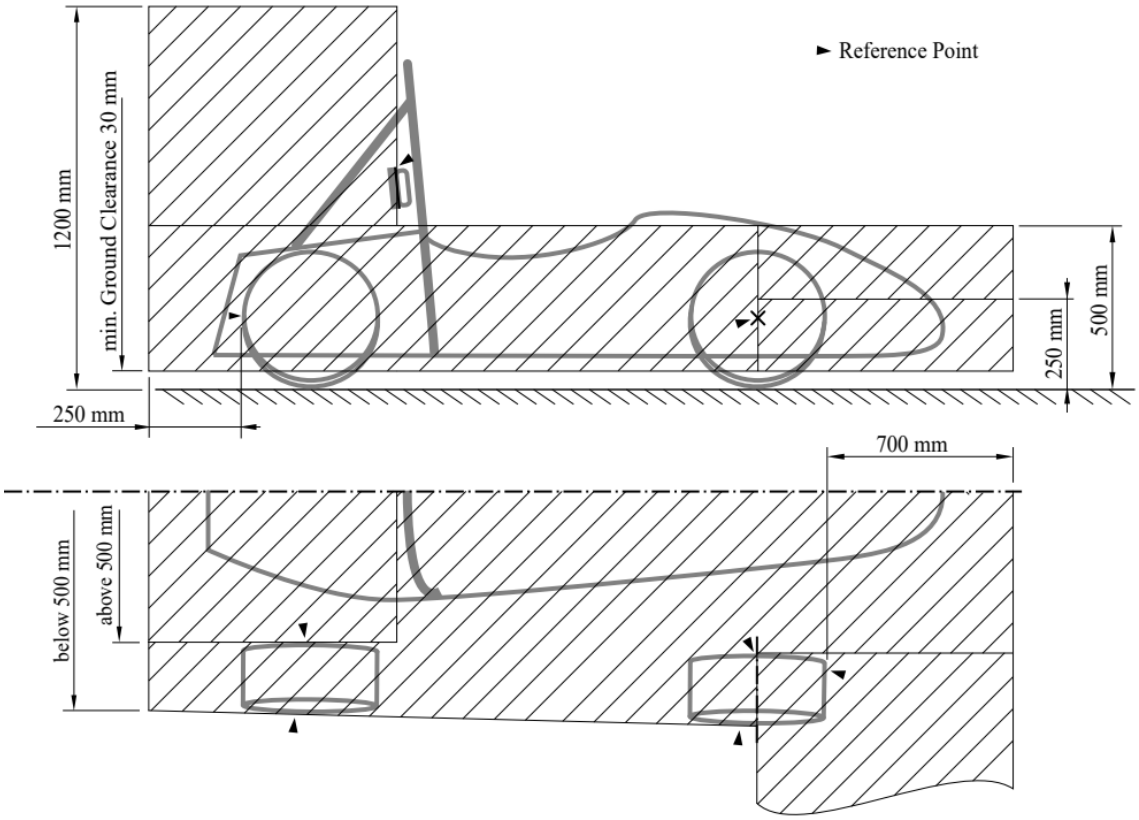

FIGURE 23. Maximum dimensions and positioning of aerodynamic devices (Formula Student Germany, 2024).

Reference point inside the roll hoop in figure 23 presents the driver head restraint support without padding, at its most rearward position.

Deflection of aerodynamic devices is limited by the rules as well. Deflection over surface of 225 cm^2 with a load of 200 N must not exceed 10mm in the load direction. Additionally, devices must not exceed deflection of 25mm at any point, in any load direction.

Risk assessment was implemented by updating FMECA-table during the whole project. The table covered failure modes, local and higher-level effects, probability, and severity and most importantly, mitigation.

4 DESIGN PROCESS

Aerodynamic design of the underbody was done iteratively during both the concepting and optimizing phase. After designing a new concept or iteration, results were obtained by using CFD. Results were then closely evaluated, both numerically and visually and notes were taken for the next iteration round. The iterative design cycle is shown in figure 24.

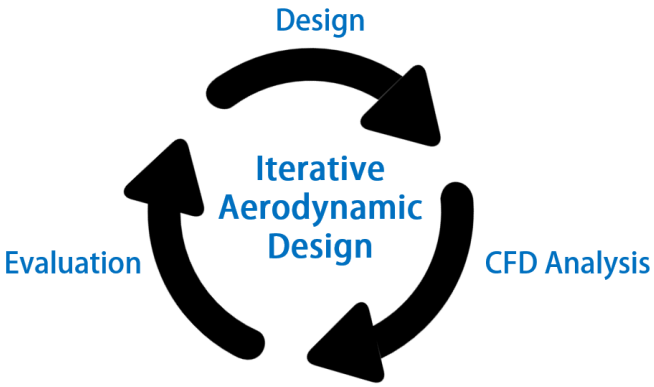

FIGURE 24. Iterative aerodynamic design, simplified.

Iterative design phase commonly consists of prototypes and regular testing before proceeding to next iterations. However, due to the season structure and limited resources of the team, testing phase will not take place before the design freeze and manufacturing of the car.

4.1 Geometry

The underbody was mainly analysed together with the simplified simulation model of the car to catch all the disturbances affecting the underbody performance. As the development of the aero package and simulation model was done simultaneously with the underbody project, the environment for analysing was constantly changing. Therefore, a certain number of simulations were done with the identical environment before updating the setup, to maintain comparability between iterations concerned.

The underbody blank was cut with the outer surface of the chassis and lower suspension cover for a proper fitment. Cut area is visible as a dark grey carbon fiber texture in picture 7.

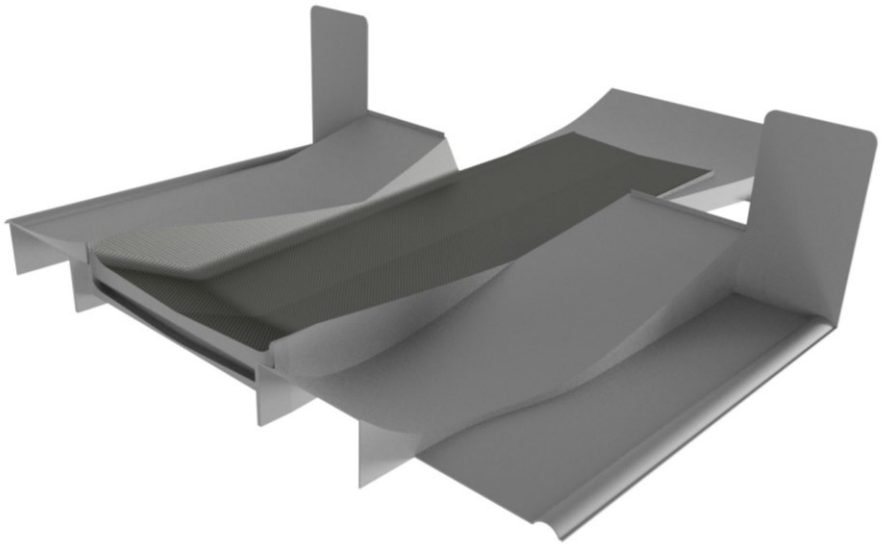

PICTURE 7. Underbody cut with chassis and lower suspension cover.

Tunnel sections were partially modelled using aerofoil profiles. Aerofoils were obtained using a plotter from Airfoil Tools -website. Aerofoil was selected from the database and desired parameters, such as chord, camber, and thickness, were entered to plotter (Airfoil Tools, n.d.). Plotted coordinates were then imported to CAD-software, Autodesk Inventor. Aerofoil from Airfoil Tools plotted in Inventor is visible in picture 8.

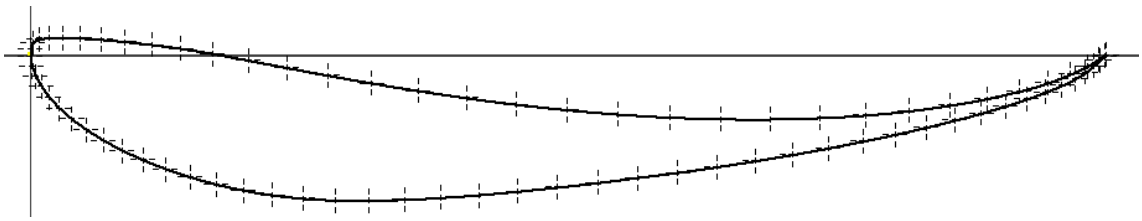

PICTURE 8. S1223 Aerofoil imported to Inventor.

4.2 Simulation model

Main components of the simulation model were a simplified chassis and a driver mock-up, suspension arms and rods without rockers, wheels, body panels, and substantially simplified powertrain components. Simulation model is visible in picture 9 below.

PICTURE 9. Simulation model of TFS24.

At early iterations, wheels and tires were only enclosed cylinders before updating to more detailed wheels. Uprights, driveshafts and hybrid gearbox were eventually added to simulation model as well.

As sidepods were under development as well, earlier iterations of the underbody were simulated without sidepods before guidelines for these were chosen. Shortly after sidepods, radiators along with block off -plates and fans were added to the simulation model as well.

Radiator assembly inside the transparent sidepod is presented in picture 10.

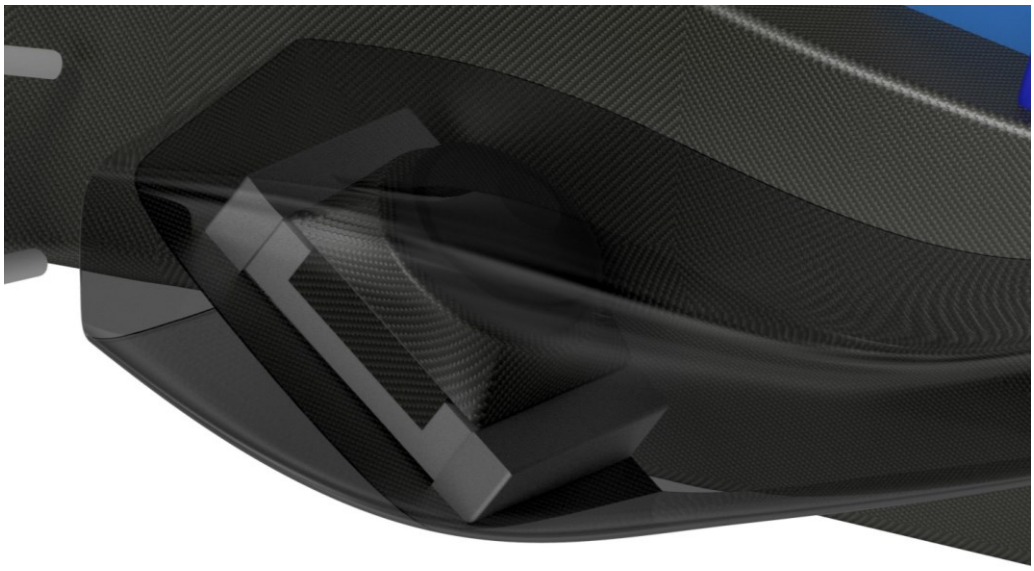

PICTURE 10. Radiator assembly in the simulation model.

4.3 Simulation setup

As previously mentioned, simulation setup was still under development as the underbody was designed. Therefore, only a general overview of the simulation setup was included in this chapter and any tweaks on the calculation parameters are dismissed. All CFD-analysis were done in the cloud, using an OpenFOAM based simulation software, SimScale.

4.3.1 Enclosure

After the simulation model geometry was imported to the SimScale, an enclosure was generated around the car. Sizing of the enclosure for external aerodynamics depends on several conditions and to find the most efficient sizing while achieving reliable results, independence studies on the enclosure and mesh is required. Due to limited calculation resources, enclosure sizing was determined based on guidelines from SimScale. Size of the enclosure can be approximated by using

the length of the car. Guidance values of these, according to SimScale, are presented in figure 25.

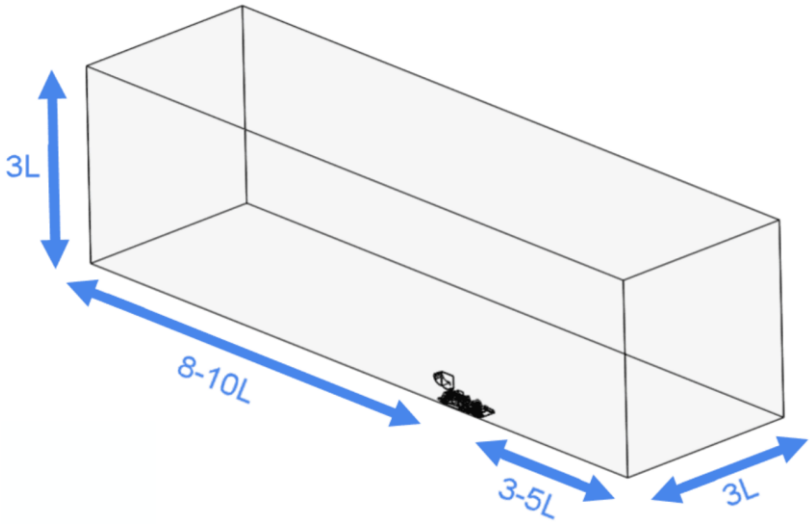

FIGURE 25. General guidelines for enclosure sizing (SimScale n.d. edited.).

Sizing was chosen as visible in table 3. Dimensions are measured from the origin of the car, which is located at the front axle on the centreline, at ground plane. When using symmetry, minimum value of Y was changed from -10 to zero, to centreline of the car.

Table 3. Enclosure size for the simulation model.

Enclosure size (m)			
X min	-26	X max	10
Y min	-10	Y max	10
Z min	0.015	Z max	9

Value of Z_{min} is positive to manipulate a slight deformation of tires. This bottom plane of the enclosure is shown in picture 11.

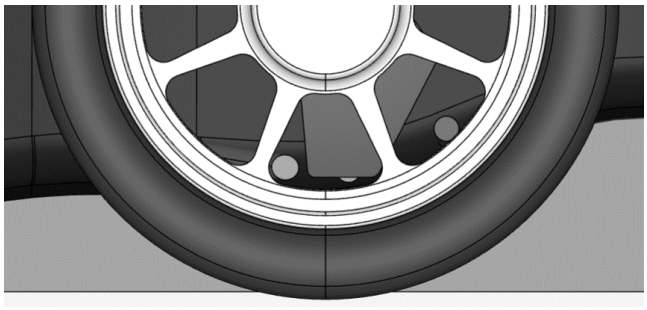

PICTURE 11. Bottom plane of the enclosure.

4.3.2 Parameters & boundary conditions

Simulations were done with an incompressible flow analysis, as flow velocities are assumed to be lower than 100 m/s, i.e. fluid compressibility is negligible. Turbulence model was chosen as k-omega SST, which is combination of k-omega and k-epsilon turbulence models (SimScale, 2023). The k-epsilon model performs well in free stream region and the k-omega offers good accuracy in boundary layer regions. Chosen turbulence model uses a blending function to switch between the k-epsilon and the k-omega models to obtain the maximum potential of both models. (SimScale, 2023). The blending region is visible in figure 26.

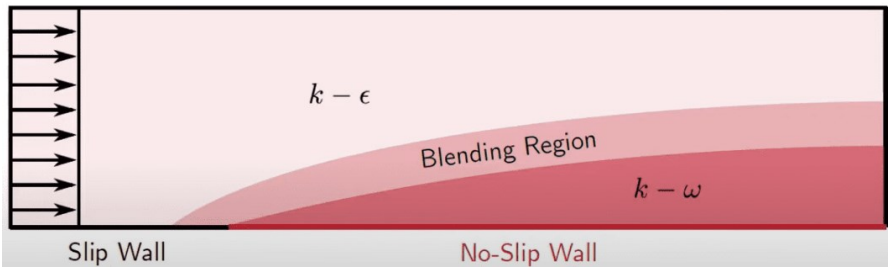

FIGURE 26. Blending region with k-omega SST turbulence model.

Air properties were changed from default values of 15°C to a more relevant 25°C, resulting in density of 1.168 kg/m^3 and kinematic viscosity of 1.57·10^{-5} m^2/s. Boundary conditions on enclosure faces are visible in figure 27.

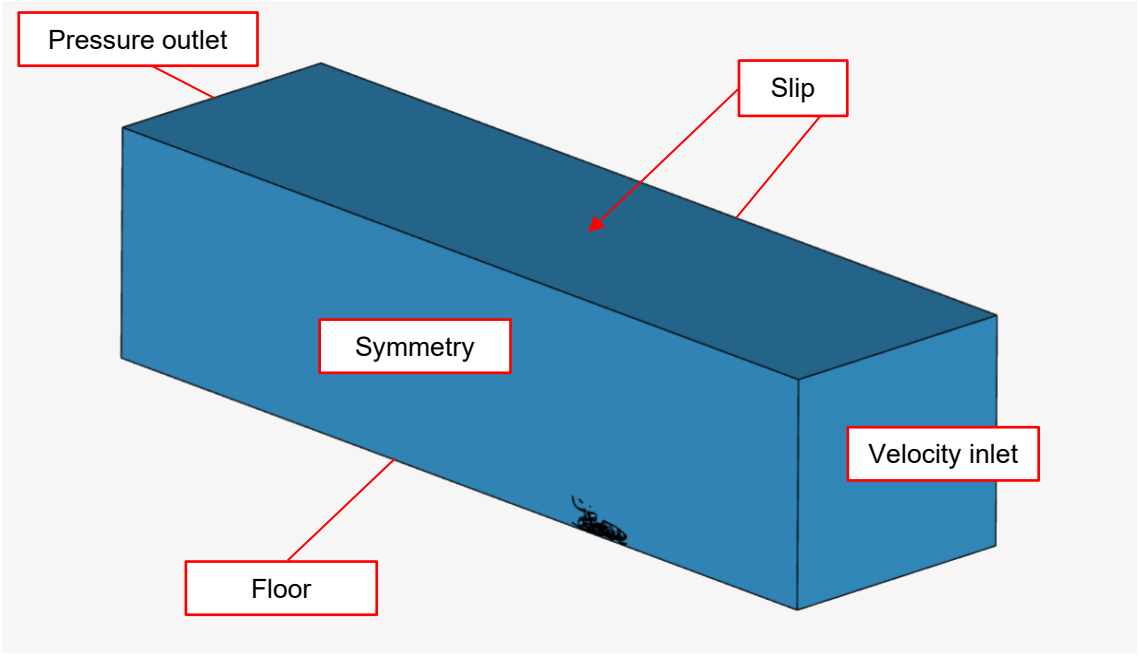

FIGURE 27. Boundary conditions, outside of the enclosure.

Velocity of the simulation was determined as 15 m/s, as it is the average speed of a vehicle on a Formula Student track. This velocity was assigned to the velocity inlet and the floor, which was assigned as a moving wall to act as a moving ground. Surfaces assigned as slip walls are handled as inviscid, so no boundary layer is developed. For the pressure outlet, gauge pressure is set to zero, resulting in a free exit velocity for the flow. Symmetry plane mirrors the domain to save resources. Front and rear wheels are assigned as rotating walls. Rotational velocity is calculated by (6)

$$\omega = \frac{v}{r} \tag{6}$$

Where:
ω = rotational velocity (m/s)
v = linear velocity (m/s)
r = wheel radius (m)

Driveshafts, when used, are assigned as rotating walls as well. The car is assigned as no-slip to develop boundary layers. Radiators and fans, when used, are excluded from no-slip condition to allow usage of porous media and momentum sources.

4.3.3 Advanced concepts

Radiators are assigned as porous media to emulate the air flow through the radiator core, using Darcy-Forchheimer coefficients. Radiator fans are emulated by fan models, consisting of tables for volumetric flow rates and fan pressures. These tables were obtained from the manufacturer.

For the power ground effect, thrusters were assigned as momentum sources, defined by average exit velocity. According to Claudel (2021), the exit velocity of a jet thruster can be calculated, given its thrust:

$$T = \rho \cdot S \cdot v^2 \tag{7}$$

Where:

T = thrust (N)

ρ = air density (kg/m^3)

S = thruster cross-section (m^2)

v = exit velocity (m/s)

Solving the velocity gives us:

$$v = \sqrt{\frac{T}{S \cdot \rho}} \tag{8}$$

This equation was implemented to fan thrusters used in simulation model. Accuracy of this approximation equation was compared to a reference high-end 93 mm thruster by Schubeler, DS-51-DIA HST, visible in picture 12.

PICTURE 12. DS-51-DIA HST 93mm (Schubeler, n.d.).

Schubeler offers performance charts of their products, including exit velocity and thrust (See appendix 1). The approximation equation with parameters of Schubeler concerned, results in exhaust velocity of 87.6 m/s, which is approximately 15% lower than the exhaust velocity presented in performance chart. As Schubeler is a premium manufacturer of highly optimized EDFs, compared to generic thruster manufacturers, this approximation approach was considered to offer sufficient accuracy for analysing power ground effect using CFD.

A generic thruster mock-up was created for the simulation model, presented in picture 13 below.

PICTURE 13. The thruster mock-up.

Additional cylindrical volume, the size of the silhouette of fan blades, was added to the fan assembly. This volume was assigned to momentum source created in SimScale. Section view of the fan assembly is shown in picture 14, additional volume highlighted in light green.

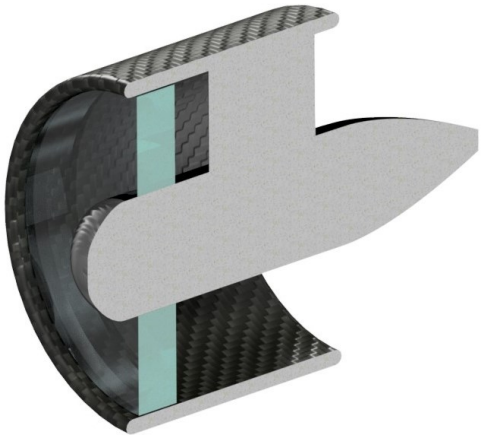

PICTURE 14. Section view of the fan assembly.

4.4 Meshing

Detail of the mesh has a significant impact on simulation results and accuracy. However, a highly detailed mesh requires major computational resources. Thus, a balance between mesh fineness and available resources should be studied. Computational resources can be used more efficiently by focusing on relevant geometry and wake regions. This can be implemented with surface and volume mesh refinements. As the development of simulation setup was a separate project of the team, it was considered as out of scope for this thesis.

Mesh was created with the standard SimScale algorithm, generating tetrahedral and hexahedral elements. Overall fineness varied from 5 to 6 in a scale of 1-10, depending on number of other refinements. Automatic boundary layers were turned off.

Several regional refinements with maximum cell edge length defined were added around the car to ensure more detailed mesh around wake regions. Region refinements are presented in picture 15.

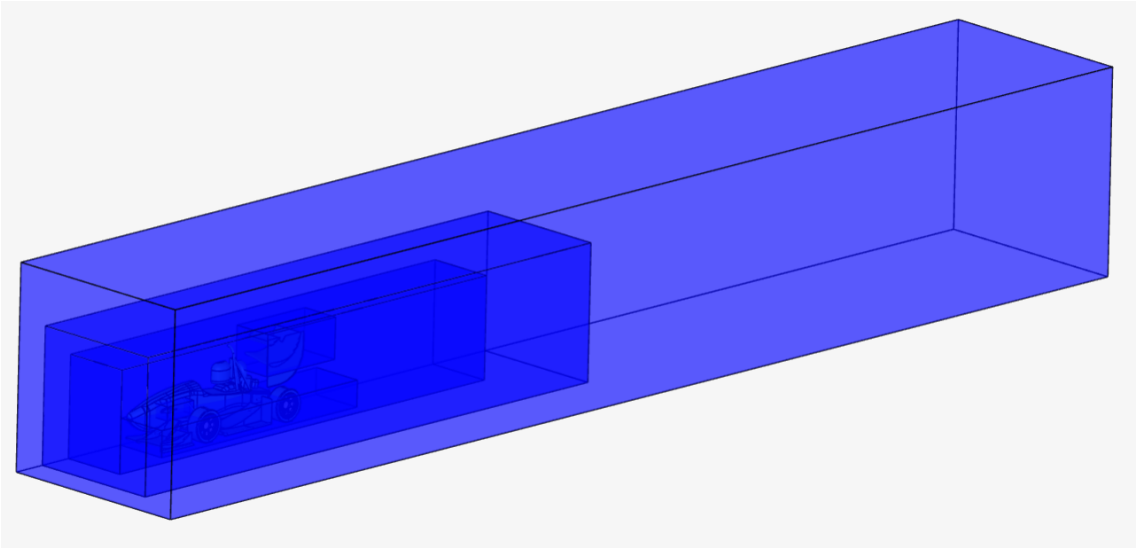

PICTURE 15. Regional refinements of the simulation model, using symmetry.

Maximum edge length varied from 10 to 80 mm, depending on focused component, and increasing with distance.

Overview of a generated mesh is shown in picture 16.

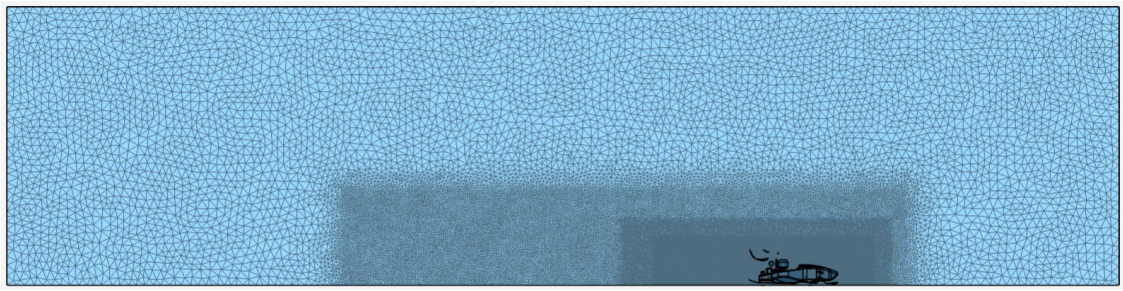

PICTURE 16. Overview of a generated mesh.

Parameters for boundary layers were calculated by using an inflation layer calculator (Fluid Mechanics 101, n.d.). As k-omega SST model was used, target y^+ -value was defined as 1. The y^+ -value is a dimensionless variable, representing the distance from the wall to the first grid cell's centre. Boundary layer meshed on a wing is shown in picture 17.

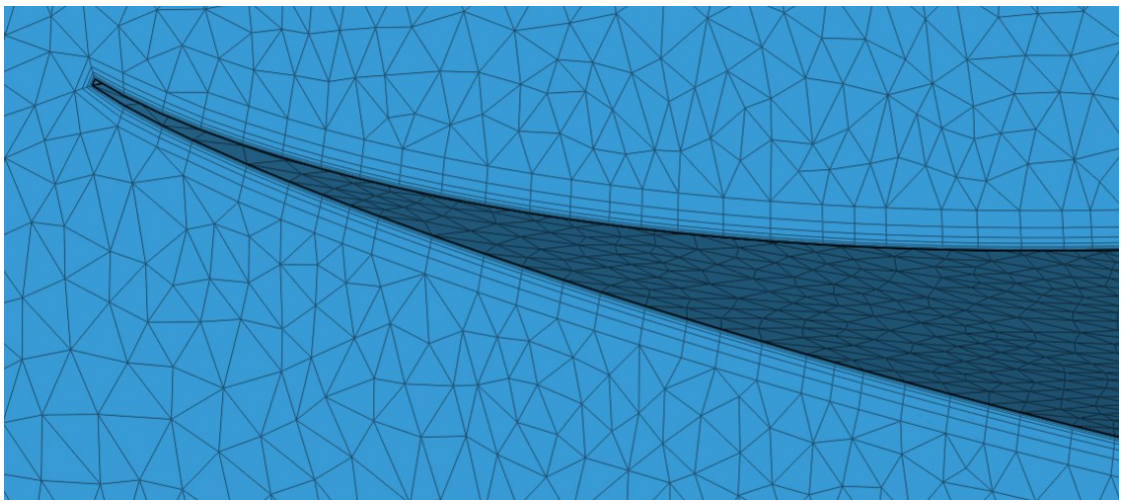

PICTURE 17. Boundary layer meshed on a wing surface.

Local element size refinements were added to surfaces such as aerodynamic components and the car body, for a more uniform and detailed mesh.

Surface mesh on the car is shown in picture 18.

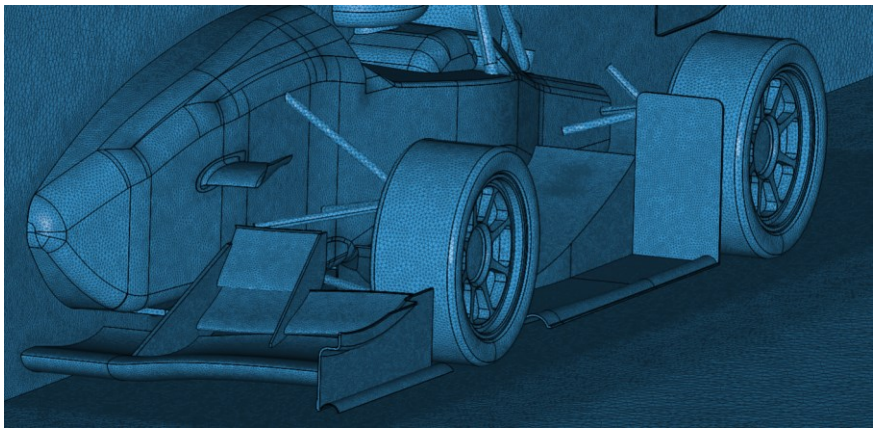

PICTURE 18. Surface mesh on the car.

After mesh was generated, its quality was verified from meshing log, which prints numerical values regarding properties of the mesh, such as aspect ratio of elements. On an irregular basis, the mesh was visually inspected as well. Additionally, when troubleshooting, visual inspection of the mesh is necessary.

4.5 Result control & post processing

Before performing the analysis, desired components were assigned to result control. These assignments were defined by selecting surfaces, shown in illustrative picture 19. With this operation, numerical results, such as pressure forces and moments in each coordinate axis, were written in desired interval.

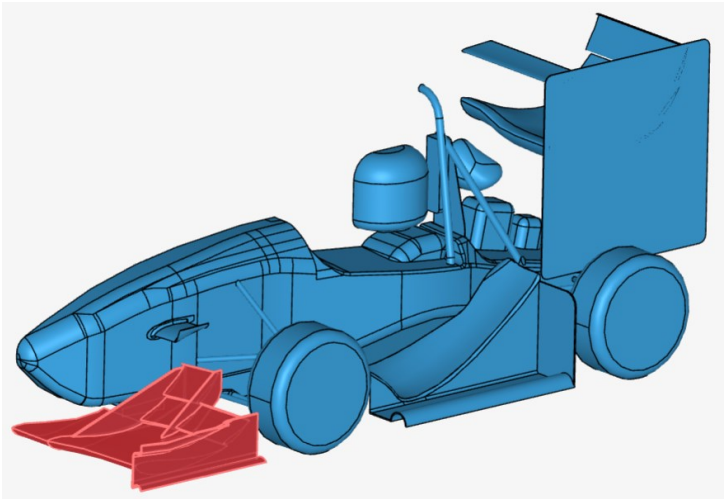

PICTURE 19. Front wing assigned to result control.

Results were written individually from the full car, front & rear wheels, front & rear wings, and underbody. Underbody results were occasionally divided into side and middle tunnels, depending on the design. Result graph of the full car in SimScale interface, including downforce and drag, in figure 28.

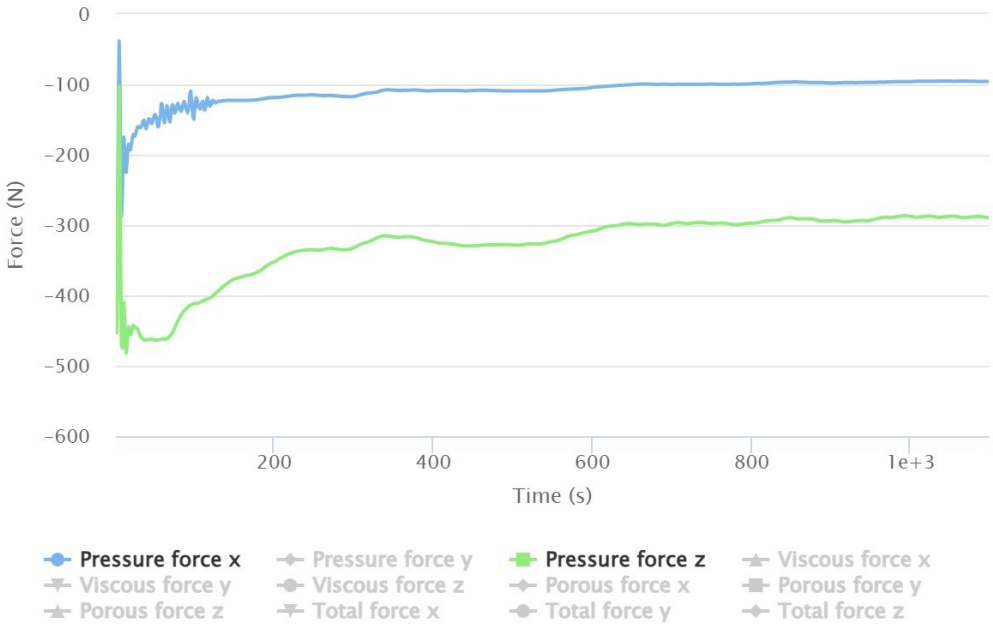

FIGURE 28. Saana, total downforce and drag measured from pressure forces.

Aerodynamic balance, also known as the centre of pressure, can be calculated from the moments and forces acting on the vehicle (Block, S. 2023). The equation for the balance at front axle is:

$$Balance_{front\%} = \frac{\left(\frac{M_y}{Wheelbase}\right)}{F_z} \tag{9}$$

Results were mainly obtained at the 1000th iteration, as simulations were sufficiently converged and increasing the simulation end time would result in linear increase in computational costs as well.

Convergence of the solution can be monitored with residuals, which describe the solution imbalances. Residuals should be as small as possible, to reach a numerical accuracy on the solution. (SimScale, 2020.) U_x, U_y, and U_z are velocities, p is pressure, and k and omega are variables of the turbulence model. For

example, convergence is reached at the 1000th iteration in figure 29 below. Convergences can also be monitored for boundary conditions, such as domain, inlets, outlet, and walls.

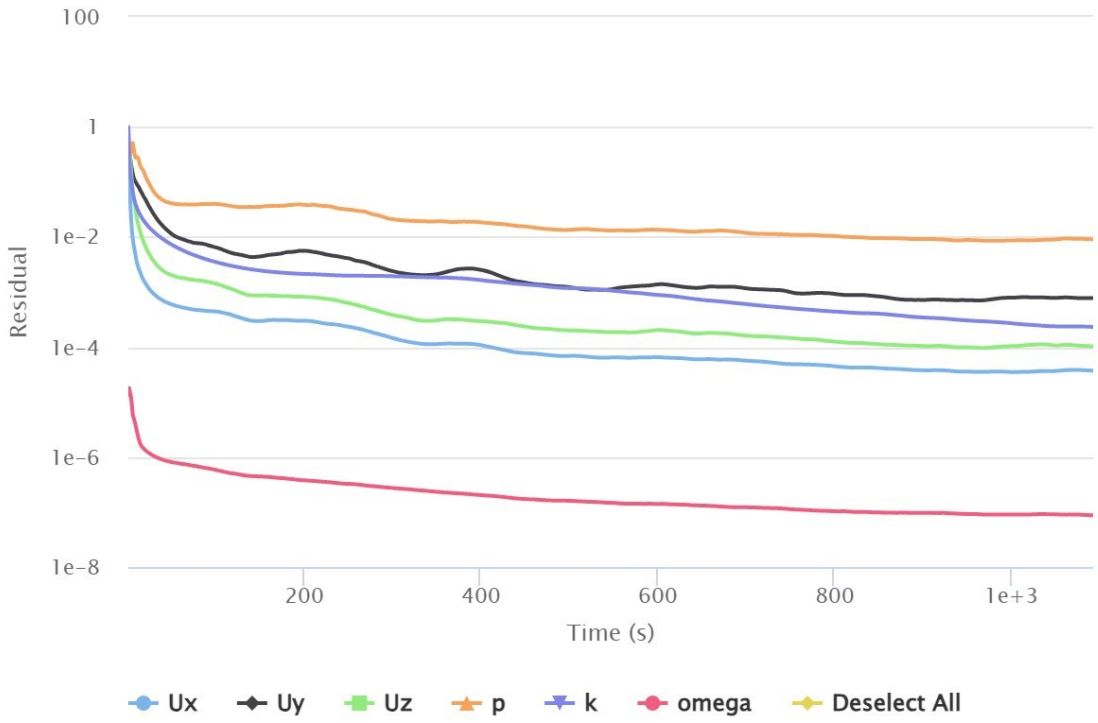

FIGURE 29. Saana, residuals.

After simulation is finished, results can be analysed both numerically and visually in post-processing. Useful and most common tools for external aerodynamics are surface colouring, cutting planes, iso volumes and particle traces. Particle trace generates streamlines along desired position, through the domain. Each filter can be coloured by velocities in magnitude or in desired direction, pressure, and kinetic energy, for example.

5 ITERATIVE DESIGN

As the simulation setup and aero package were constantly changing during the underbody project, these differences were considered during evaluation of underbodies. Effect of changes in simulation setup, geometry, and mesh, were evaluated with each iteration, respectively.

Since numerous iterations and minor tweaks were studied during the underbody project, irrelevant versions are dismissed or only briefly introduced, and more notable versions and milestones are presented and discussed in this thesis.

5.1 Concepting phase

Concepting phase included several approaches for the new underbody and the most promising ones proceeded for later iterations. Some design aspects from the last season were maintained in most of the concepts, such as half tubes on side tunnel footplates, and a straight backplate in front of the rear tire, as they were interpreted as simple and solid designs to improve overall efficiency of an underbody.

5.1.1 First concept

First relevant concept was to implement a wide, full length mid tunnel, with an aggressive intake to scoop air from upwash induced by front wing. The diffuser consisted of four channels, with higher angles in the middle sections. This is visible in pictures 20 & 21.

If the pressure scale is not determined separately in the context, it is always adjusted from -200 to 100 Pascals, as shown below. Tires of the simulation model were only solid mock-ups at the time.

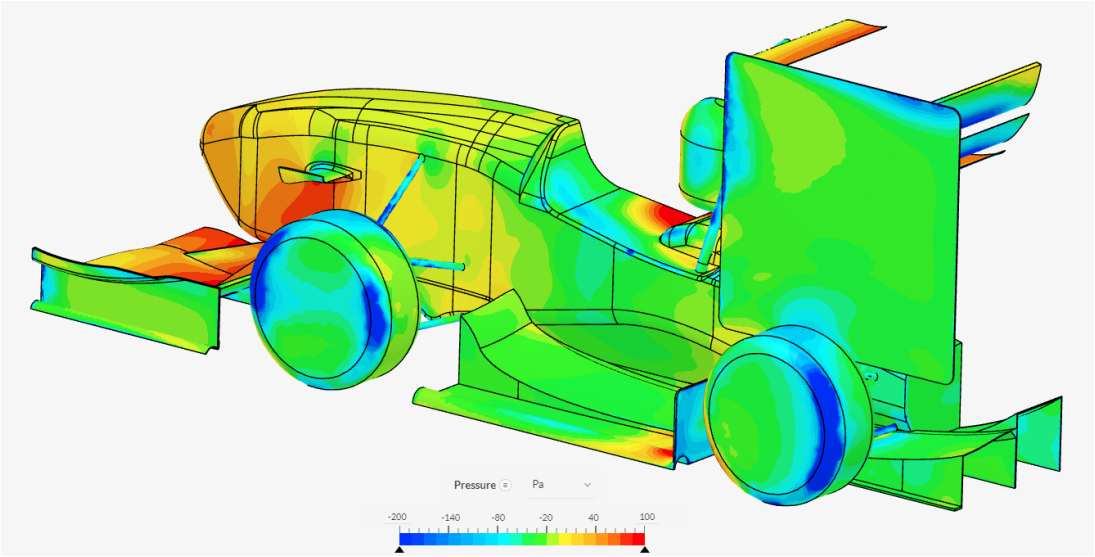

PICTURE 20. 1st concept with wide tunnel, overview.

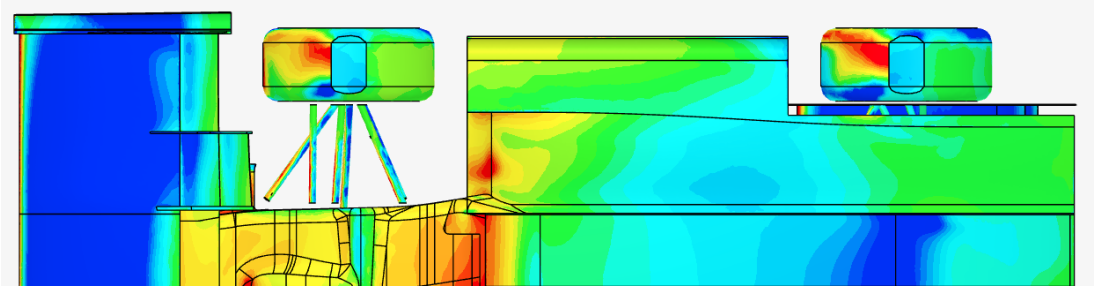

PICTURE 21. 1st concept, bottom pressure contours.

Mid tunnel low pressure region is uniformly distributed, with the choke point located at the rear axle. This underbody produced 150N of downforce, with the early simulation setup. Middle and side tunnels were divided to smaller sections with full length vanes, visible in picture 22.

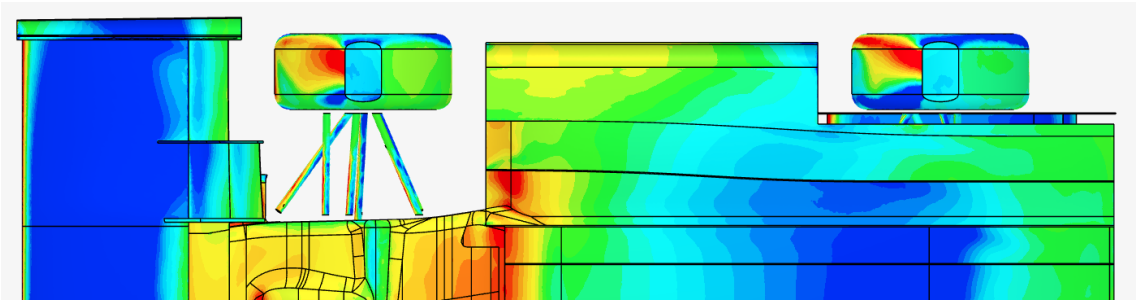

PICTURE 22. 1st concept with smaller sections, pressure contours.

Adding more sections improved the overall performance of the underbody, increasing the downforce from 150 to 175 N.

5.1.2 Second concept

The second concept was similar to the first one, except the lower intake and a curved vane on the outer mid tunnel section. Lower intake is shown in the picture 23.

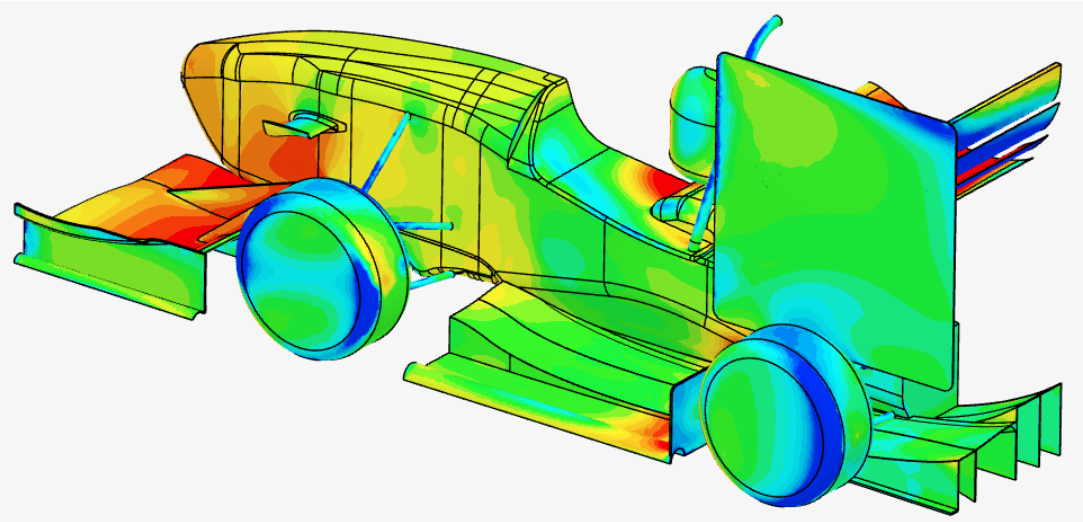

PICTURE 23. 2nd concept with a lower intake, overview.

Curved vane added a Y-directional choke on the inner side of the side tunnel section. A lower intake reduced mass flow, without affecting the flow attachment. These additions improved overall performance to 208 N. Curved vane is shown in picture 24.

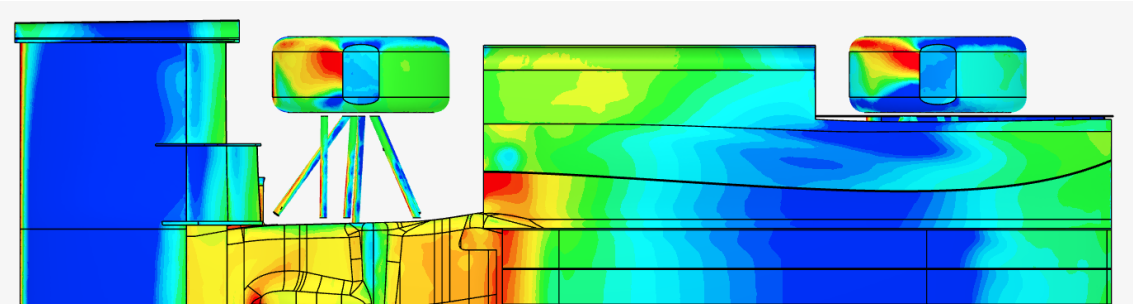

PICTURE 24. 2nd concept and curved vane, pressure contours.

5.1.3 Third concept

Side wings, consisting of two elements, were introduced in third concept, visible in picture 25. Wheels and rear wing were updated to simulation model as well.

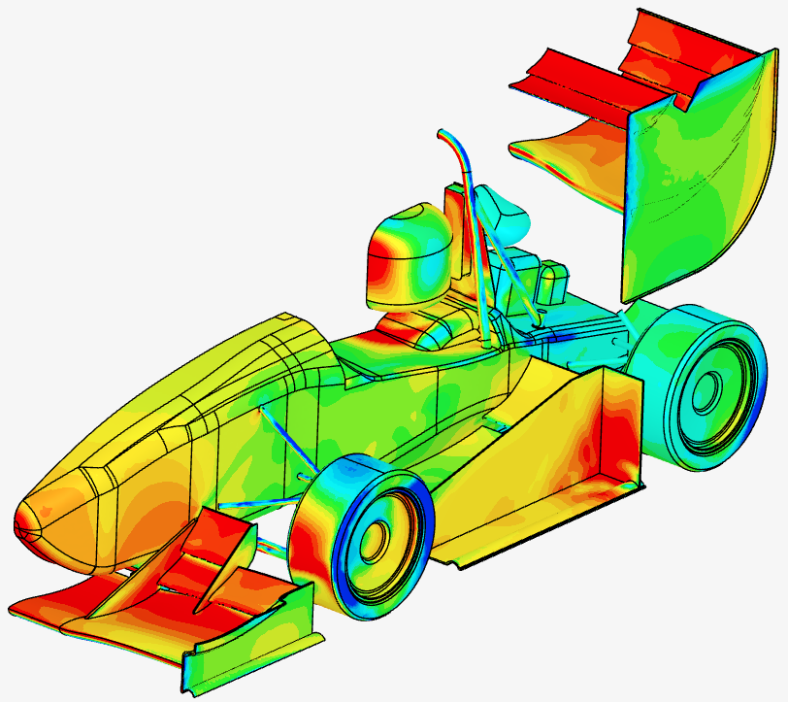

PICTURE 25. 3rd concept with side wings, overview.

The second element of side wing was positioned at low angle of attack, as there were no reference positions or angles to start with, see picture 26. Following velocity contours are always scaled from zero to 20 m/s, if not determined separately in the context.

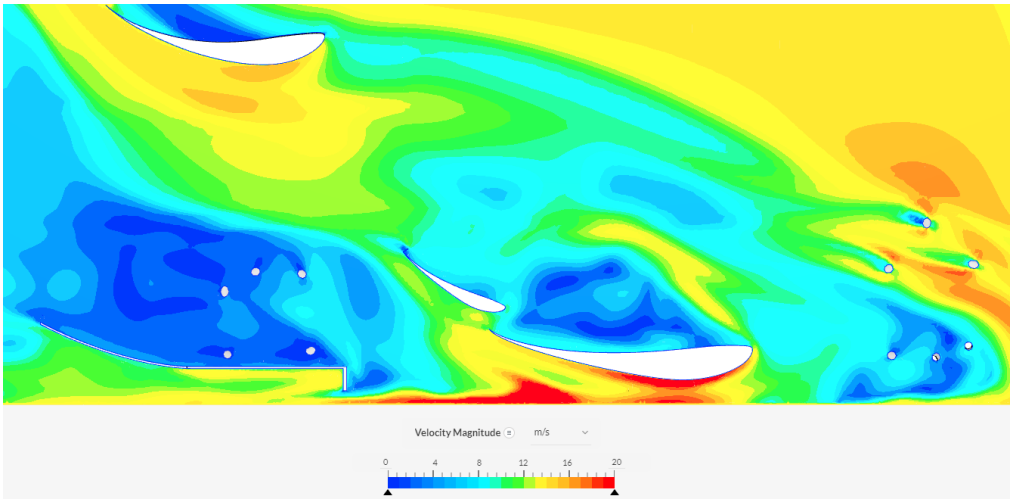

PICTURE 26. 3rd concept, side wing velocity contours.

This concept generated 220 N of downforce, with a potential to improve its performance by optimizing parameters of the wing assembly. However, adding radiators and sidepods would largely affect on the performance of a multi-element side wing assembly.

5.1.4 Fourth concept

Side wings were replaced with a single side tunnel in the fourth concept, visible in picture 27. The car is coloured with pressure contours and the cutting plane with velocity contours, in a same scale as previous figures, ambient pressure of zero Pascals and a free-stream velocity of 15 m/s are both in yellow for the ease of inspection.

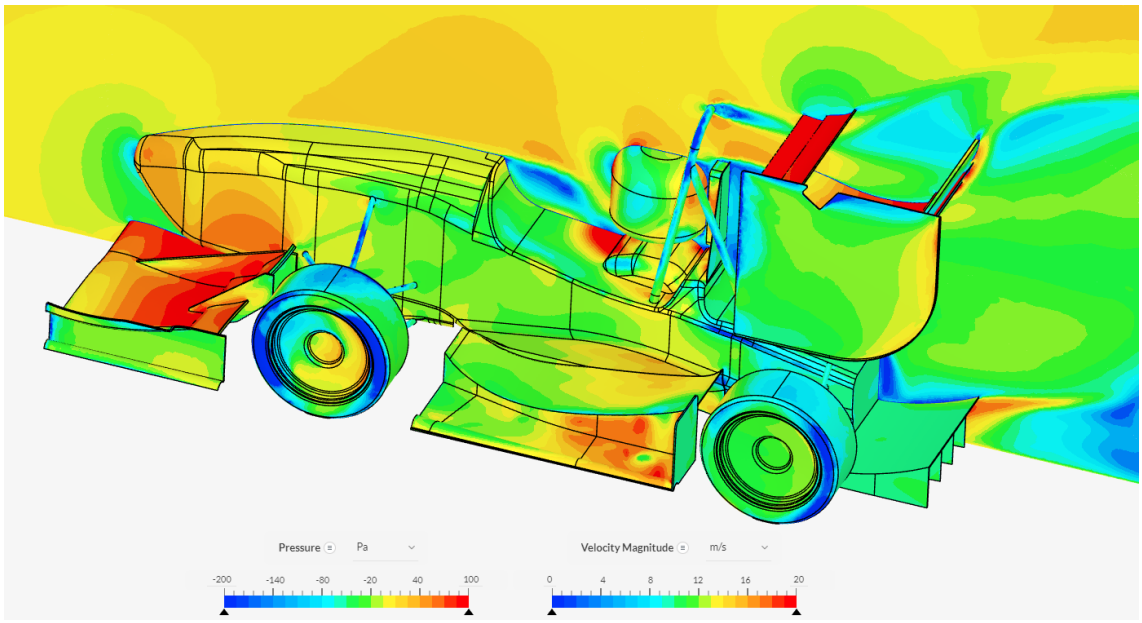

PICTURE 27. 4th concept with single side tunnel, overview.

The flow stays relatively attached along the side tunnel, while maintaining the velocity at and above ambient. The region of dead air above the side tunnel is greatly weakened, when compared to a previously presented multi-element side wing assembly in picture 25.

The fourth concept induced 235 N of downforce in total. The velocity contours of the fourth concept are visible in picture 28.

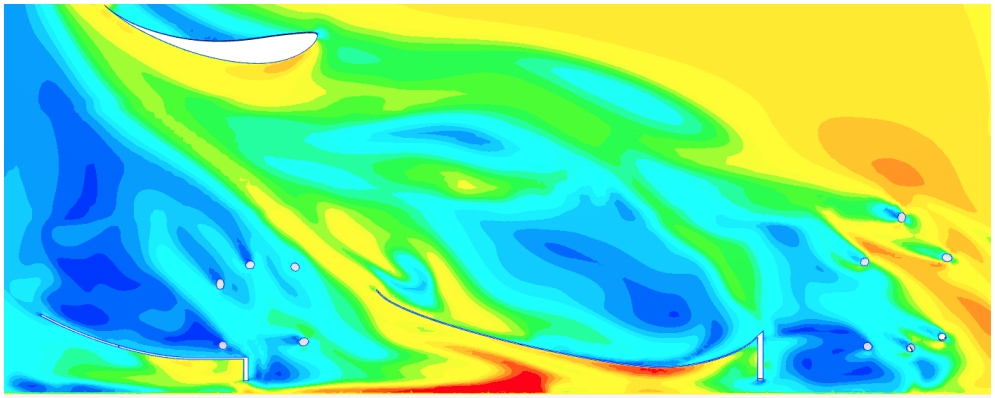

PICTURE 28. 4th concept with single side tunnel, velocity contours.

5.1.5 First impressions on power ground effect

Since there were already a few concepts that exceeded the performance of Saana's underbody, thrusters were added for both Saana's underbody and to the fourth concept. An independent fan assembly, powered by separate power supply was an obvious choice, since mechanical operated system would be highly inconvenient due to its complexity and dependency on powertrain speeds. Electric ducted fans, EDFs, were easily approachable systems while offering high amounts of thrust. In the simulation model, performance was equated to the EPF Mercury II -thruster, manufactured by EPF, shown in picture 29. According to the manufacturer (EPF, n.d), maximum peak thrust of the fan was 3.9 kg.

PICTURE 29. EPF Mercury II 90mm (EPF, n.d).

Comparison simulations were performed with the early simulation setup and without the thruster mock-up. Instead, a cylindrical geometry primitive was configured as a momentum source in the SimScale interface, visible in picture 30, highlighted in dark blue.

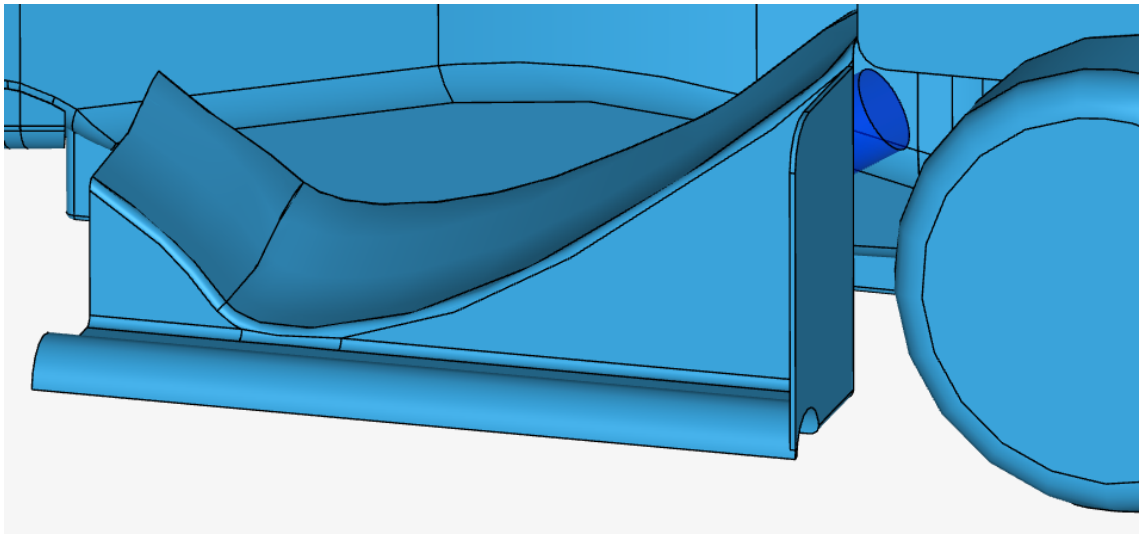

PICTURE 30. Geometry primitive as a momentum source, Saana's underbody.

Simulations were done with both underbodies, with 1, 2 & 3 kg of thrust implemented. Pressure and velocity contours are compared in picture 31.

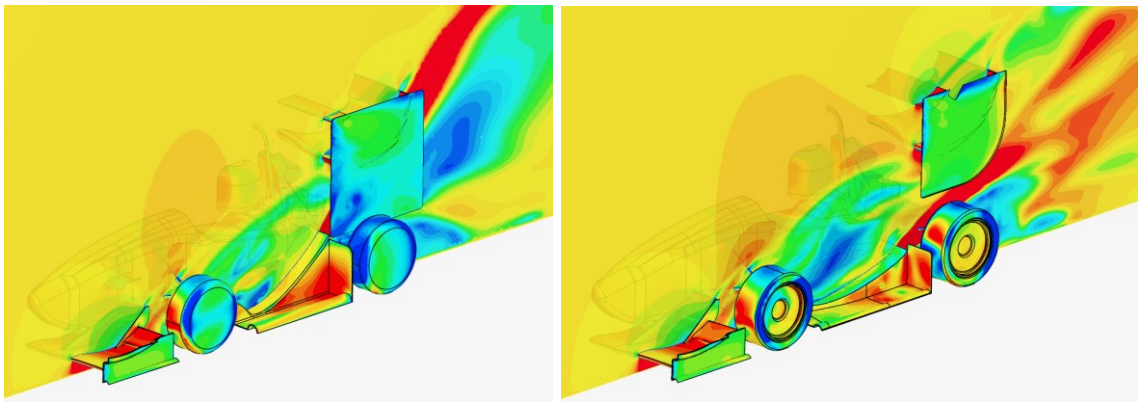

PICTURE 31. Saana (left) & 4th concept (right), 3 kg of thrust, pressure & velocity contours.

Saana's side tunnel at extreme angle of attack spills high-velocity flow to the outer side of the rear wing endplate, decreasing the pressure difference. However, rear wing endplates on the 4th concept are smaller as well, which in turn increases the difference between these underbodies. The efficiency of the Saana's backplate

is significantly higher, due to its height and the spilling mentioned earlier. A closer look inside side tunnels is visible in picture 32 below.

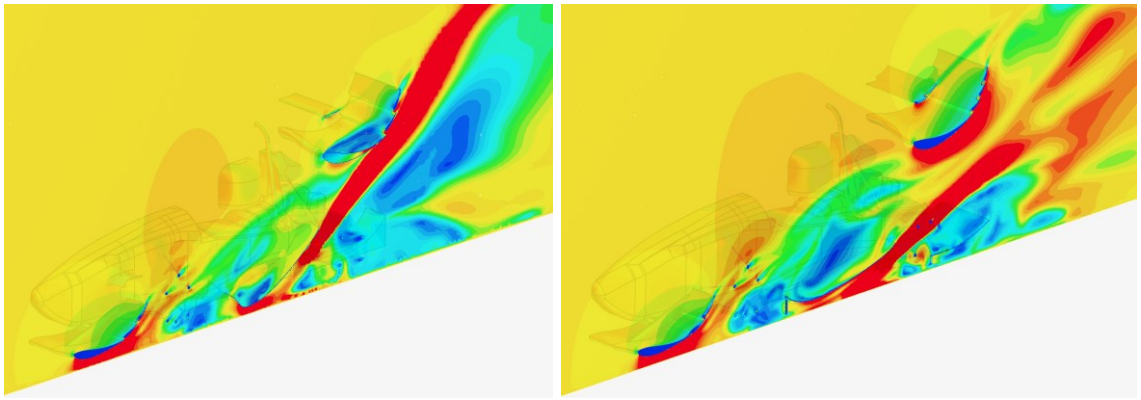

PICTURE 32. Saana (left) & 4th concept (right), 3 kg of thrust, pressure & velocity contours, clip model enabled.

High velocity jet of Saana's thruster towards rear wing main profile, suffocates incoming air from the upper side of wings. This devastating effect is avoided with the 4th concept side tunnel, as the high-velocity flow accelerates the air beneath the rear wing, without affecting its multi-element characteristics. The cutting plane also reveals an insufficient flow attachment after the choke point, regardless of high suction generated by the thruster. Numerical results of this comparison are shown in table 4.

Table 4. Comparison between Saana & 4th concept, with power ground effect.

Thrust (kg)	Saana			4th concept			Improvement in downforce (%)
	cL	cD	Underbody downforce (N)	cL	cD	Underbody downforce (N)	
0	4.37	1.46	194	4.25	1.55	236	21.6%
1	2.13	0.78	104	4.66	1.90	278	167.3%
2	5.28	1.83	274	5.08	2.24	318	16.1%
3	5.72	2.00	326	5.25	2.48	348	6.7%

Performance of the 4th concept underbody overcame Saana, with and without thruster. As thrust is increased, the suction of the thruster overcomes high curvature on Saana's side tunnel, therefore gradually reducing the gap between underbodies compared. This complies, except with a thrust around 1 kg, since large separation bubble is generated on the side tunnel surface, visible in picture 33. However, the total lift coefficient of the car was higher with Saana's aero package,

as the performance of the front wing was greatly higher at the time, due to development process of TFS24 front wing.

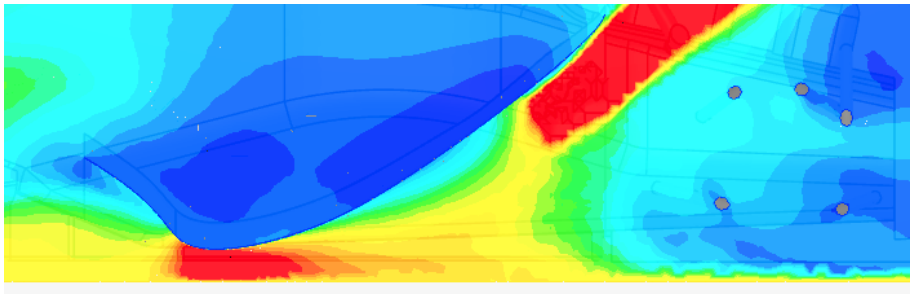

PICTURE 33. Region of dead air forming on Saana's side tunnel surface, 1 kg of thrust.

5.1.6 Fourth concept with an updated simulation setup

Simulation setup had major updates, including changes in mesh settings and more detailed wheel geometries. Several regional refinements were added, local element size limits were added and adjusted, and separate boundary layers for the body and aero components were created. Therefore, results from the 4th concept and Saana were gathered again. Saana was simulated with the same geometry presented earlier, with updated settings. The 4th concept was simulated with detailed wheels and updated settings. Detailed wheels with a particle trace through the front wheel are shown in picture 34.

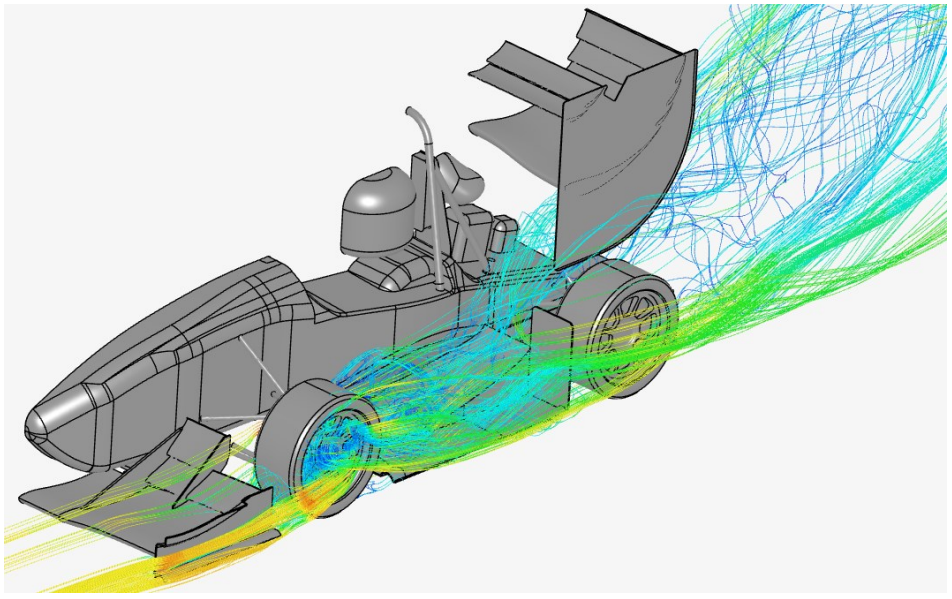

PICTURE 34. 4th concept with detailed wheels, particle trace coloured by velocity.

As detailed wheels allow flow to pass through cutouts, amount and strength of disturbances are greatly increased. Additionally, due to changes in simulation setup, performance of both underbodies was decreased. Regardless of disturbances created by detailed wheels in 4th concept simulation model, 175 N of downforce was generated, while Saana's underbody performed with 150 N of downforce.

5.1.7 Fifth concept

Intake height and angle of attack of side tunnels were increased from the fourth concept, visible in picture 35. Analysis was performed with the updated simulation setup. Uprights were added to the simulation model as well.

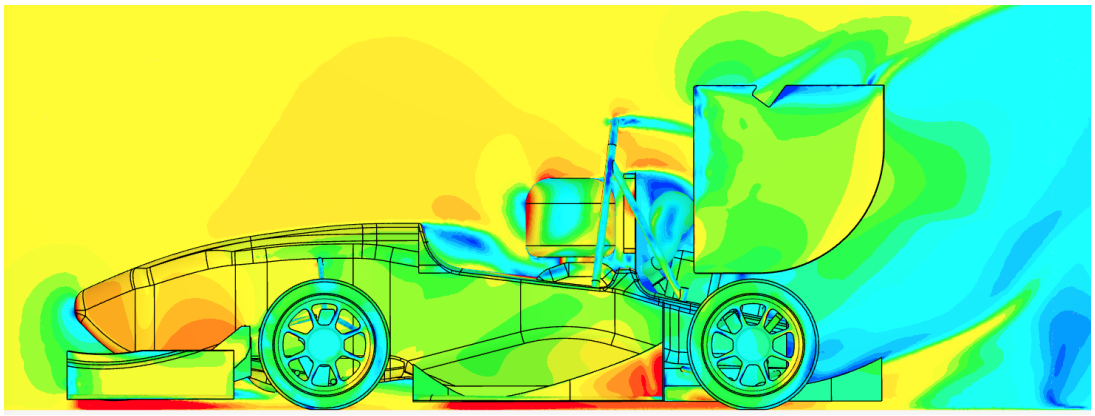

PICTURE 35. 5th concept, higher side tunnel intake and increased angle of attack.

Middle tunnel included expanding diffuser and curved vanes, visible in picture 36. Curved vanes generate local low-pressure areas, slightly extending suction from choke point at the front to the rear axle.

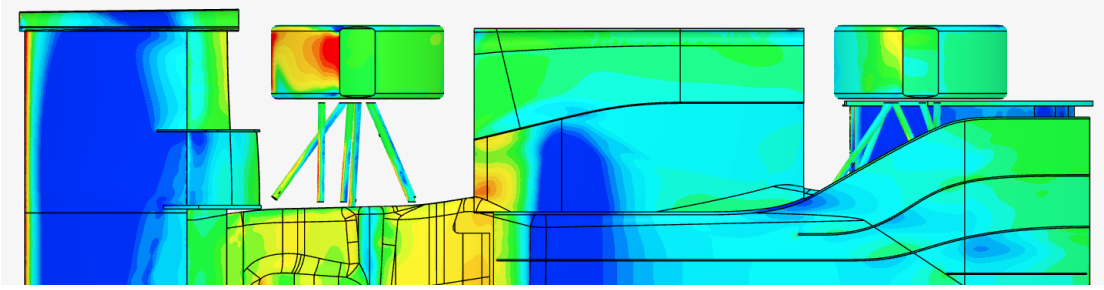

PICTURE 36. 5th concept, mid tunnel vanes, pressure contours.

Front and rear wheels induce long wake regions, reaching outer sections of the diffuser, velocity contours are shown in picture 37.

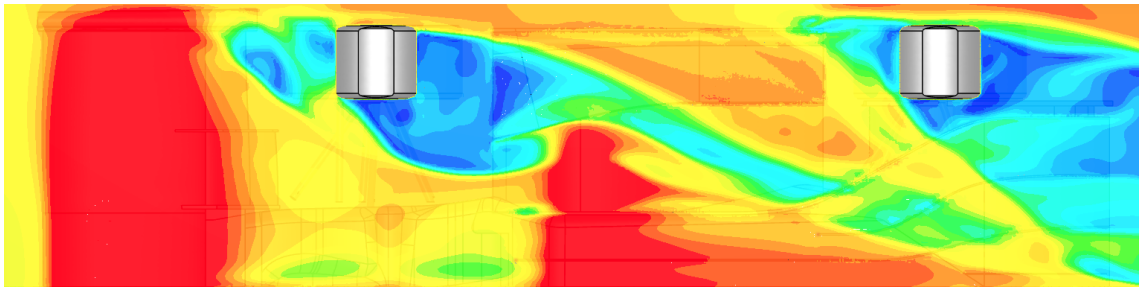

PICTURE 37. Wake regions induced by wheels, cutting plane 25 mm from the ground.

Inner section of the mid tunnel stays relatively undisturbed. Disturbances from wheels can still be identified when traversing closer to the diffuser surface. Regardless, flow tends to remain attached on first curves of the vanes, visible in picture 38.

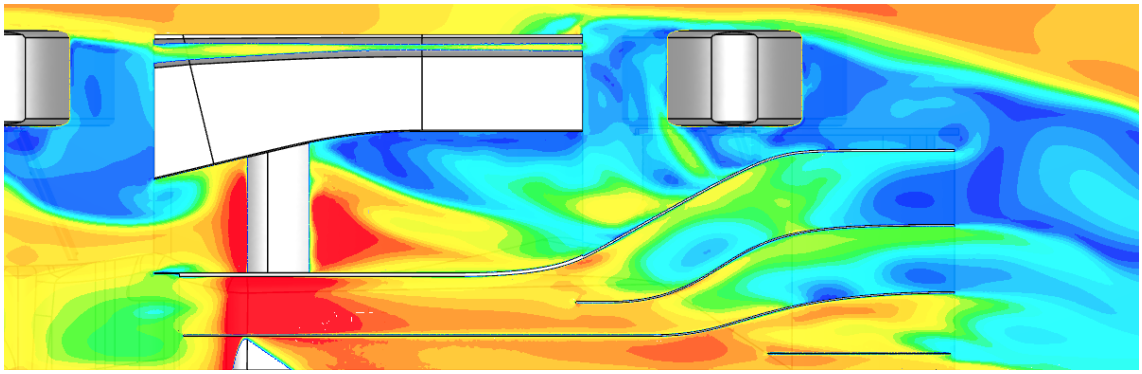

PICTURE 38. Wake regions induced by wheels, cutting plane 45 mm from the ground.

The fifth concept performed slightly better compared to the fourth concept, generating 190 N.

5.1.8 Evaluation of the concepts

Once there were three different main concepts created, these were evaluated and compared, before choosing designs to proceed with. Results were once

again analysed visually, and SWOT-analyses were performed to each main concept, respectively (see appendices 2-4).

Side wings possessed potential for a high downforce generation, but high risks and manufacturing costs were included as well. Continuous wide tunnel and separated tunnels were both solid performers and the power ground effect would be easily implemented, if chosen so.

Since separated tunnels were already studied in the previous season and the most likely risks were identified, the concept in question was chosen to be developed. Additionally, the middle tunnel was lacking in Saana's underbody. Since some guidelines to side tunnels were already known, effort from side tunnel design could be allocated to mid tunnel studies as well.

In a worst-case scenario with a zero budget for the underbody, design choice could be used as a precaution: Any design aspects gained during the underbody project with separate side tunnel could be improvised into Saana's underbody.

5.2 Iterations

Even though the main concept was chosen to be iterated, any potential designs or addons were not dismissed, maintaining the design phase open minded. First impressions of the power ground effect were highly potential, but the available budget for the underbody was still uncertain. Regardless, option for power ground effect was kept in the design process for an easier implementation in the future.

5.2.1 Side tunnel and diffuser vanes

First update to reach 200 N with the updated simulation setup was adding vanes to divide side tunnels, visible in picture 39. The thruster mock-up was added to the simulation model to act as a turned off EDF.

As the underbody was partially a further development of Saana's underbody, it was named accordingly. Since underbody of TFS23 was named Biggie Talls due to its aggressive side tunnels, this less aggressive underbody was named Biggie Average, later referred only as "BA".

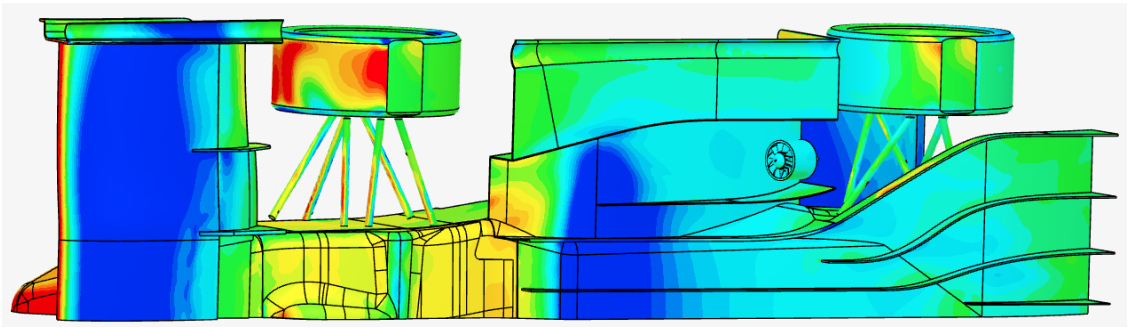

PICTURE 39. Pressure contours of BA 1.1, with an additional side tunnel vane.

The suction peak was extended on the inner section of the side tunnel, increasing total downforce, regardless of the thruster mock-up.

All vanes were reconfigured, and the diffuser was changed to a lower one in BA 1.3, visible in pictures 40 & 41. The rear wing was changed to a next concept at the time as well.

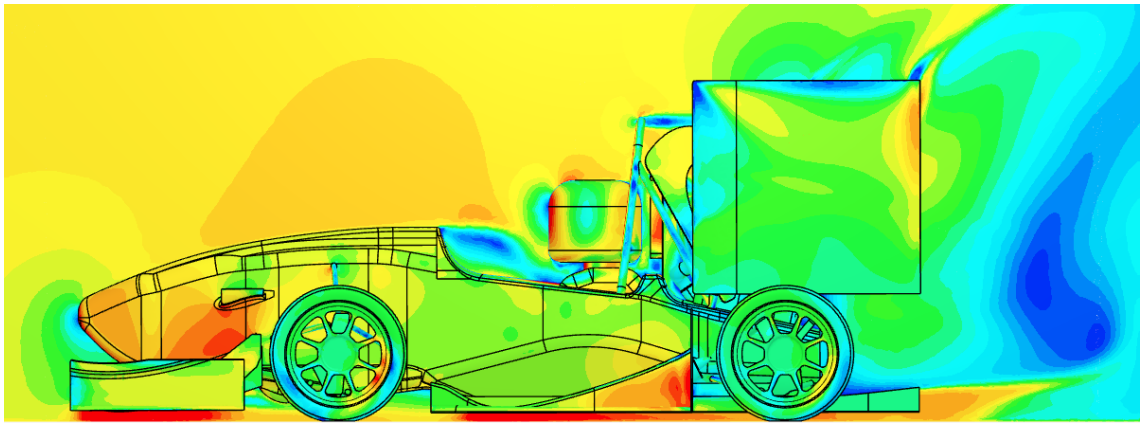

PICTURE 40. BA 1.3, with a mild diffuser angle (7°) and updated rear wing.

Side tunnel vane was extended further forward, diffuser vanes were split from mid tunnel vanes. Footplates were added to outer wall and outer vane of the diffuser.

Transition from middle tunnel to diffuser was executed without vanes to allow flow to reach each narrow section of the diffuser. This caused increase in pressure in the transition region. Regardless of this deficiency, BA 1.3 generated 218 N in total.

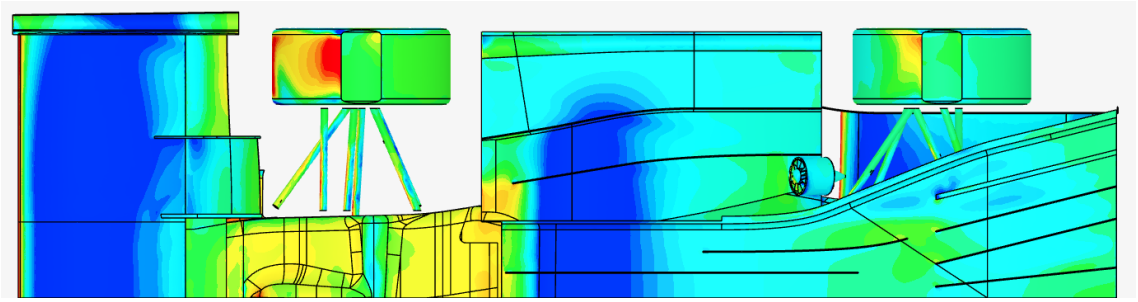

PICTURE 41. BA 1.3, new configuration of the vanes.

5.2.2 Diffuser heights

Single simulation of BA 1.3. consumed up to 8 hours before finishing. Therefore, multiple simulations of BA 1.3 were run simultaneously, regarding height of the diffuser. Numerical results are shown in table 5. Height is measured from the ground to the maximum height at the rear of the diffuser.

Table 5. Diffuser height simulations.

Index	Angle (°)	Height (mm)	Downforce (N)
1	7	130	218
2	9.5	140	222
3	12	150	212
4	14	160	216
5	16	170	222
6	18.5	180	214
7	20.5	190	214

All configurations varied in a range of 8 N, which can be interpreted as simulation inaccuracy. Thus, no increase in downforce was assumed.

However, flow started to separate with higher angles when traversing away from the car centreline, see pictures 42 – 44. Such large separation regions could affect more radically to the performance of the diffuser than captured in CFD.

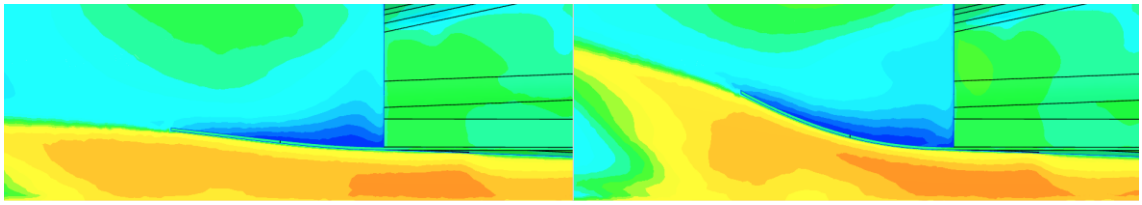

PICTURE 42. Diffuser angle 7° (left) & 20.5° (right), cutting plane at the car centreline.

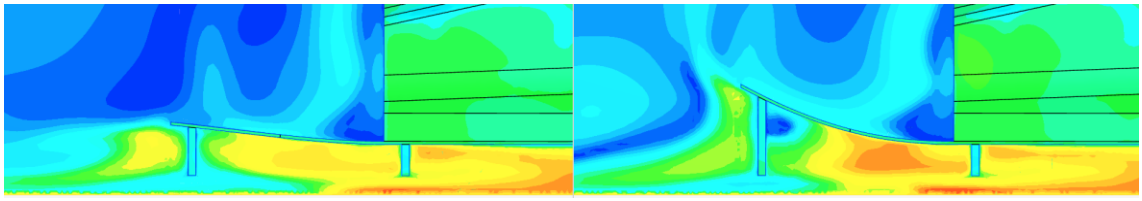

PICTURE 43. Diffuser angle 7° & 20.5°, cutting plane 200 mm from the car centreline.

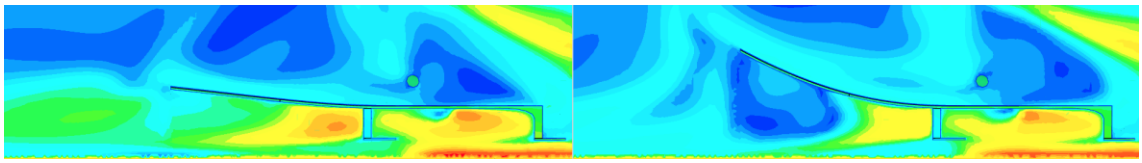

PICTURE 44. Diffuser angle 7° & 20.5°, cutting plane 300mm from the car centreline.

5.2.3 Second element for the side tunnel

Several changes were studied in BA 2, including an additional wing for the side tunnel, a rounded backplate, and completely replaced vanes on the diffuser, visible in pictures 45 & 46. Inner channel of the diffuser was changed to a higher angle, as it had been observed to have a cleaner flow.

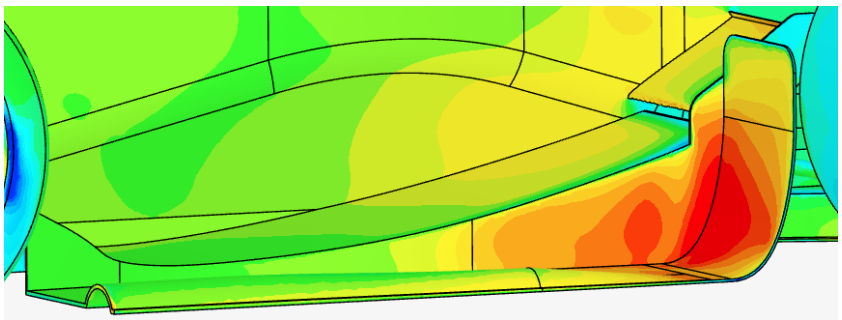

PICTURE 45. BA 2, Closer view on the side tunnel.

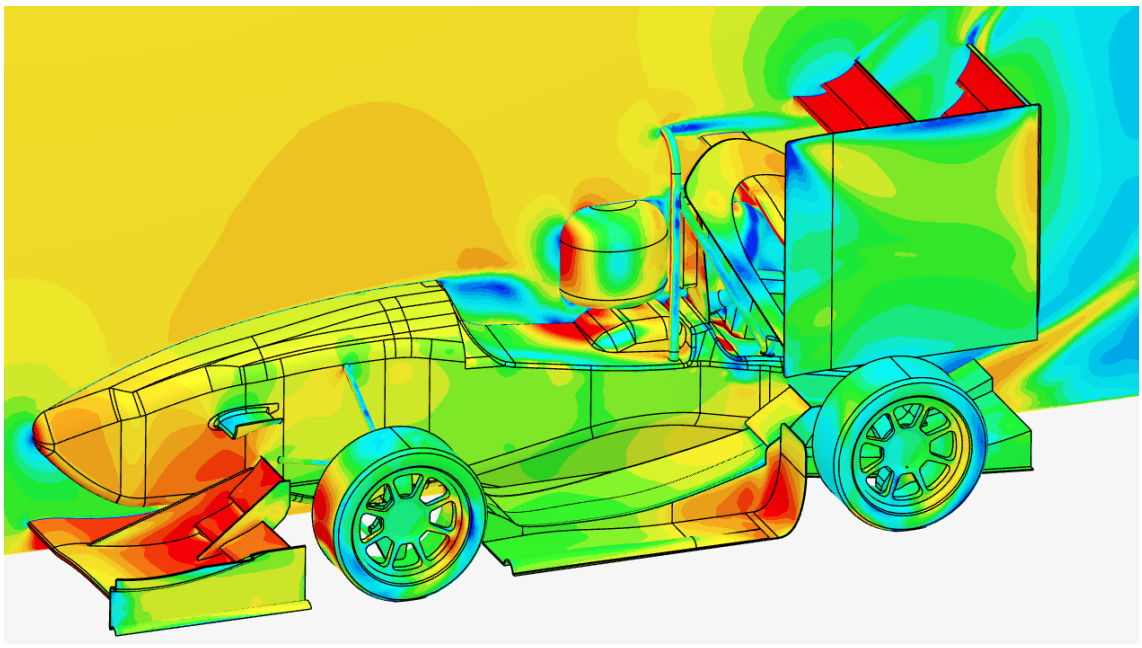

PICTURE 46. BA 2, Additional side tunnel wing, rounded backplate, and a multi-angle diffuser.

Bottom layout of the underbody is visible in picture 47. Side tunnel choke point was created both horizontally and vertically, aiming to improve suction locally. Diffuser had two main channels, inner & outer, which were sectioned again with vanes. Performance of the outer section of the side tunnel was quite modest, mostly due to disturbances from front wheel. Side tunnel vane in turn performed efficiently, partially isolating inner side tunnel from major tire wake regions. The highly expanding shape of the diffuser and its vane layout generated several sub-optimal small regions of higher pressure.

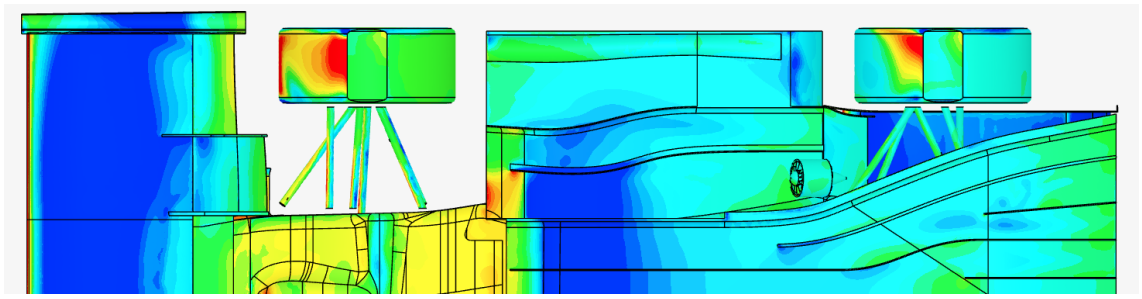

PICTURE 47. Bottom layout of the BA 2.

Due to placement of the thruster, benefits of the additional wing were low. The thruster decelerated flow in the critical transition region from the first element to the second one, shown in the picture 48. The thruster could be attached lower to

reduce this downside, but the lower position would strive to drag the flow away from the tunnel surface when turned on, therefore affecting efficiency of active runs. Overall performance of the BA 2 was decreased from BA 1.3, with total 212 N.

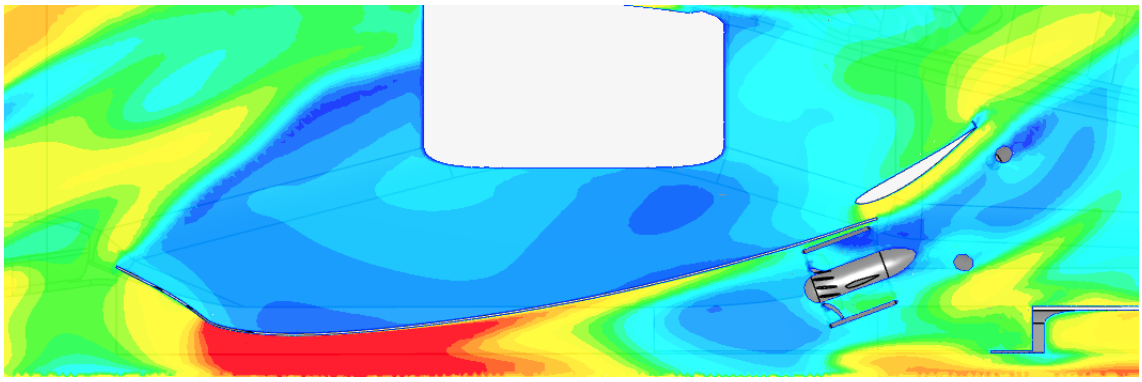

PICTURE 48. Thruster interference with the second element of the side tunnel.

Thruster could be optimised to interact efficiently with the second element, but optimization would require additional aerodynamic components to place the thruster behind the wing, or alternatively further rearward with ducts and tunnels. This process would consume vast amounts of design and calculation resources, as well as excessive costs during manufacturing. Thus, design of the BA 2 was suspended.

5.2.4 Additional diffuser

Since the complex, expanding diffuser was challenging to configure for reaching efficient flow along its entire surface, a simplified design was implemented, visible in picture 49. Side tunnel characteristics from BA 1.3 were included in the design.

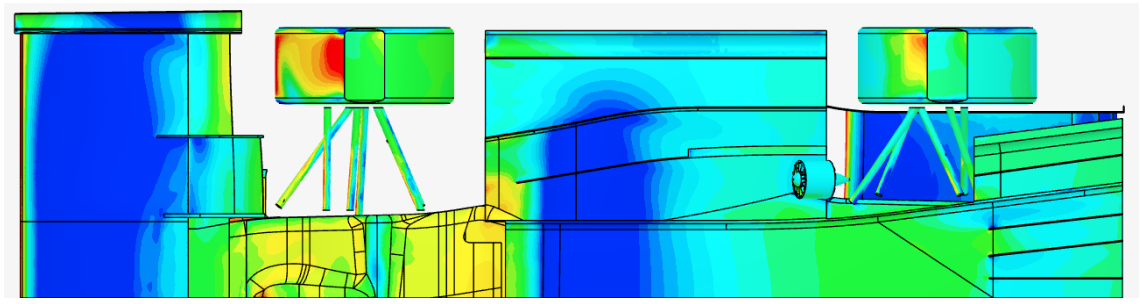

PICTURE 49. BA 3.2, simplified diffuser geometry.

Side tunnel maintained low pressure along its entire length and a narrow intake partially prevented tire wake from entering the outer section of the side tunnel.

As a new component to the simplified diffuser, a short diffuser with a separate inlet was introduced. The main purpose of this device was to guide tire wake away from the main diffuser. Velocity contours along the diffuser section are presented in pictures 50 – 52.

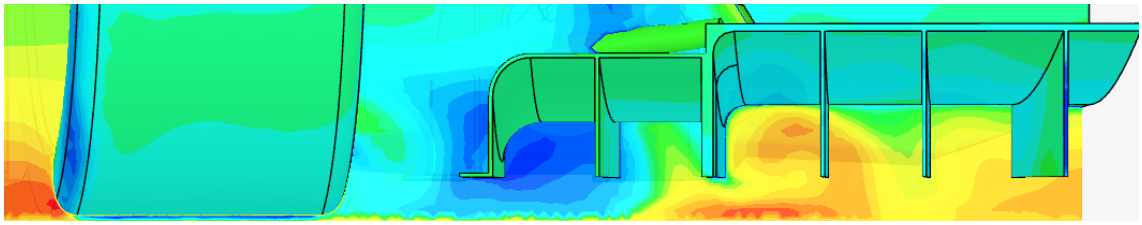

PICTURE 50. Velocity contours around the diffuser, 1600mm from front axle.

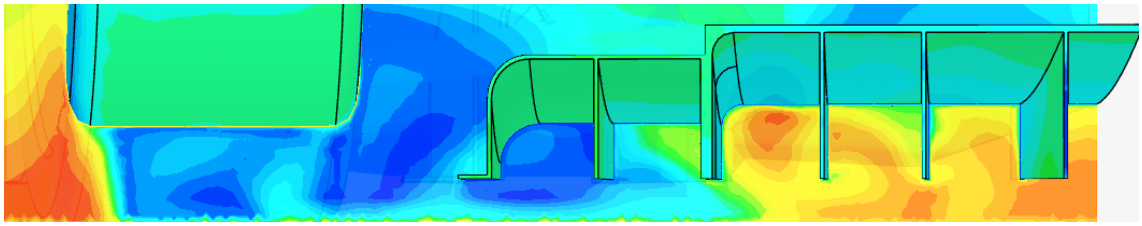

PICTURE 51. Velocity contours around the diffuser, 1700mm from front axle.

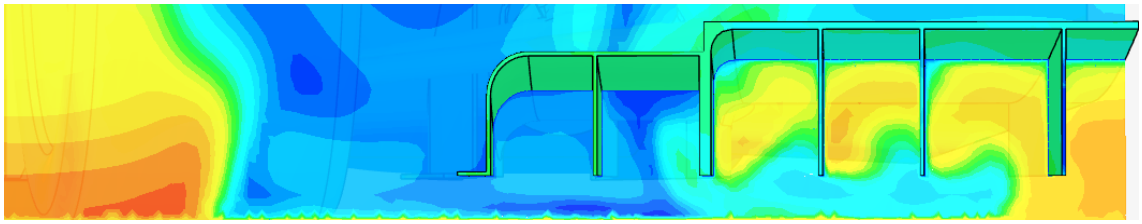

PICTURE 52. Velocity contours around the diffuser, 1900mm from front axle.

The additional diffuser captured part of the rear tire wake around its inlet, but eventually disturbances overcame this effect, when traversing towards the end of the diffuser. Also, some of the high velocity air was drained from the main diffuser to the additional one, seen in the picture 50. There were not improvements in total performance, as downforce induced by BA 3.2 was 210 N, practically identical to BA 2. However, these results were gained with a considerably simpler geometry.

5.2.5 Simple diffuser

Additional diffuser from previous design was removed in BA 4 and vanes were reconfigured, see picture 53. It was suspected with the previous underbody, that the thruster mock-up has only a minor effect on flow behaviour, except tunnels with second elements, so the thruster was suppressed from the assembly to save resources in meshing and calculation. A symmetric aerofoil was added to the mid tunnel to act as a vane and a jacking point for the car.

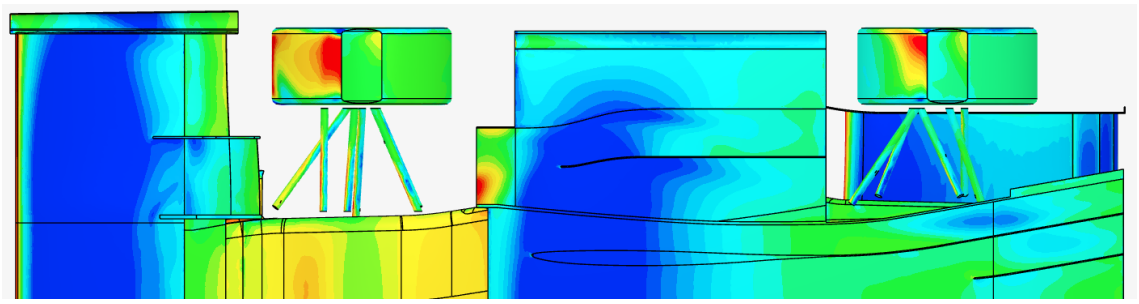

PICTURE 53. Simple diffuser and the jacking point on the BA 4.2.

Side tunnel was simulated with both 5° and 7° angles of attack and vane relocations were performed. No significant differences or any new findings were revealed during these iterations. Maximum downforce of 210 N was recorded.

5.2.6 Multi-angle side tunnels

A potential discovery was found with BA 5, with separated side tunnels, consisting of different angles of attack, shown in picture 54.

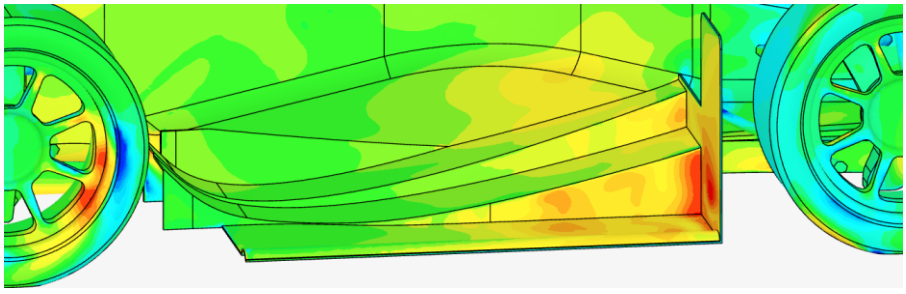

PICTURE 54. Multi-angle side tunnels, BA 5.

Inner section of the tunnel was set at 9°, as the incoming airflow was relatively clean closer to chassis. Higher angle extended the peak of low pressure further rearward. The outer section was set at 5°. Due to the increase in downforce, air was sucked from the sides to the outer section, visible in picture 55.

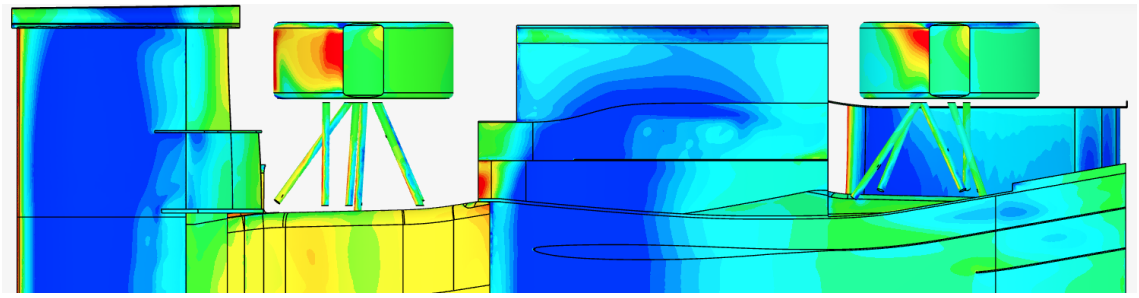

PICTURE 55. BA 5, with multi-angle side tunnels and a jacking point.

Local low-pressure regions were generated at the beginning of the diffuser, improving airflow of the middle tunnel. BA 5 outperformed previous designs with 236 N. Since this result was achieved without the thruster mock-up, design was simulated again with the thruster. Side tunnel performance slightly decreased, but flow patterns remained highly similar. Total output of the underbody decreased to 220 N.

5.2.7 Flat middle tunnel

Since side tunnel performance was solid despite the disturbances, sections were extended further to the sides to provide more effective surface, shown in picture 56. The diffuser was further simplified, consisting of only two sections. Rear wing was updated to the simulation model again.

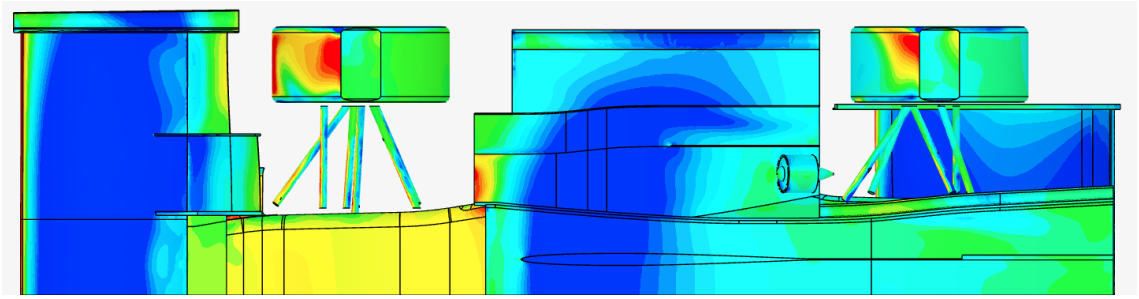

PICTURE 56. Extended side tunnels and simplified diffuser in BA 6.3.

Side tunnel vane was removed from the choke point region for a more uniform suction peak, the shorter vane acting as a mounting plate for the thruster. Straight inner section of the middle tunnel maintained low pressure along its length. Due to low curvature on the outer section, suction peak at the diffuser was weakened, compared to iterations of BA 5.

Downforce generation was at the same level with the BA 5, inducing 222 N, but the major difference came with the aero balance. Middle tunnel on BA 5 followed the curvature of the chassis, while BA 6.3 implemented a flat floor before the diffuser section, see pictures 57 & 58.

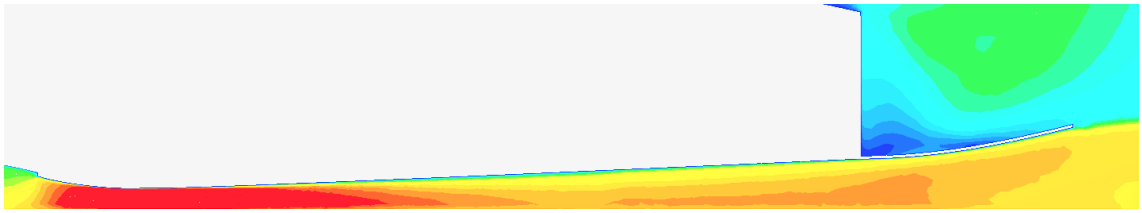

PICTURE 57. Middle tunnel curvature, BA 5.

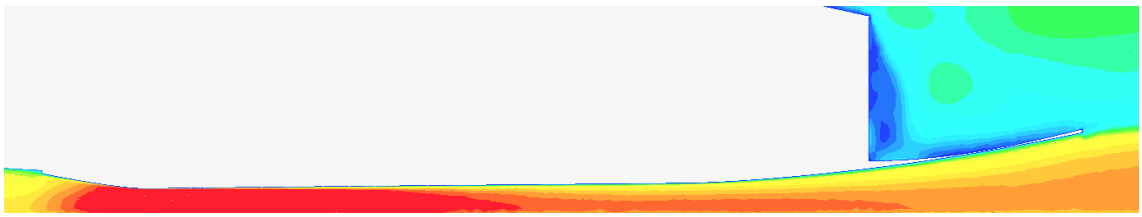

PICTURE 58. Middle tunnel curvature, BA 6.3.

Flat floor extended the fast-velocity region closer to the diffuser, altering the aero balance 2% further rearward. Together with the updated rear wing, simulation model with the BA 6.3 reached aero balance of 54% at the front axle. Aero balance with the BA 5 was at 58%.

First version of the sidepods was designed by another team member in aerodynamics and added to the simulation model. However, radiators and block-off plates were not assembled in place at the time. BA 6.4 with a simple multi-angle diffuser was also simulated with the sidepods and the updated rear wing, shown in picture 59.

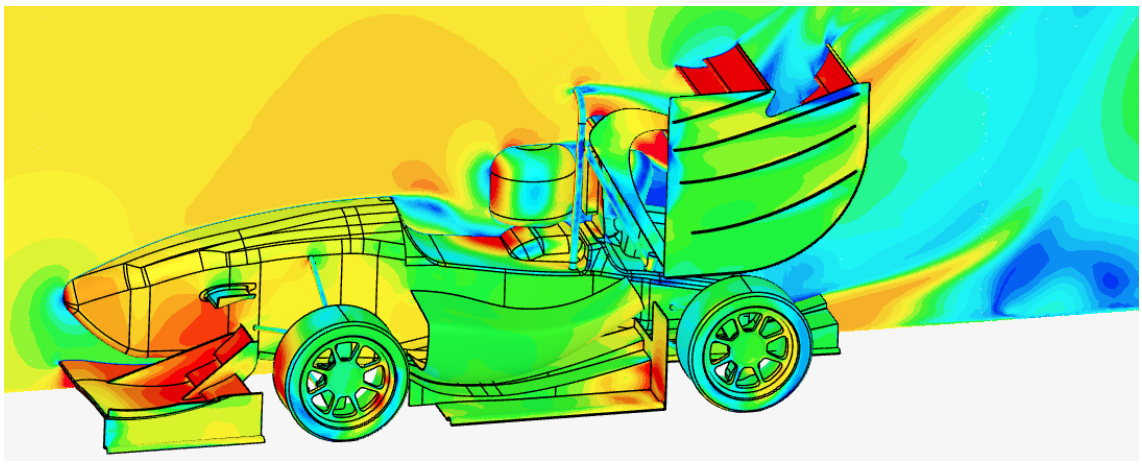

PICTURE 59. Overview of the BA 6.4 with the sidepods and the updated rear wing.

Flow patterns with and without the sidepods are presented in pictures 60 & 61.

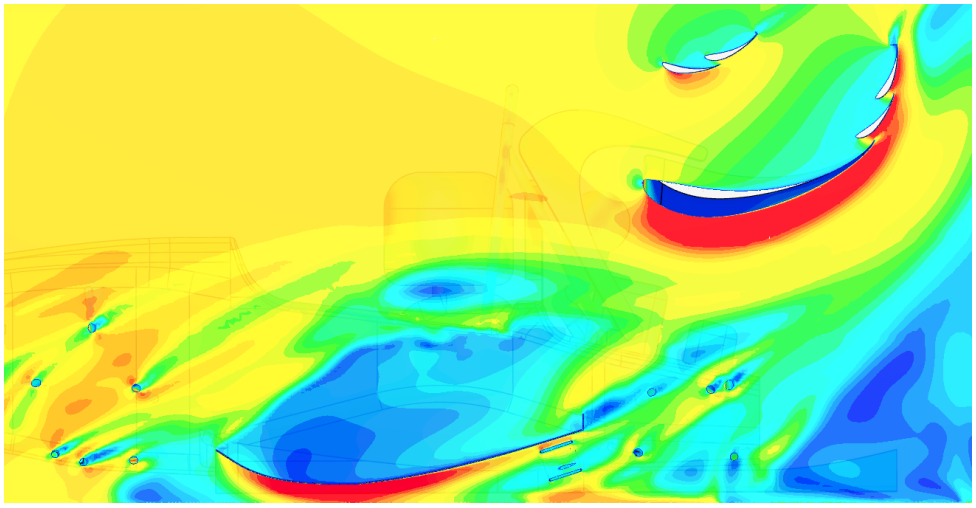

PICTURE 60. Flow pattern without sidepods, 350mm from the centreline.

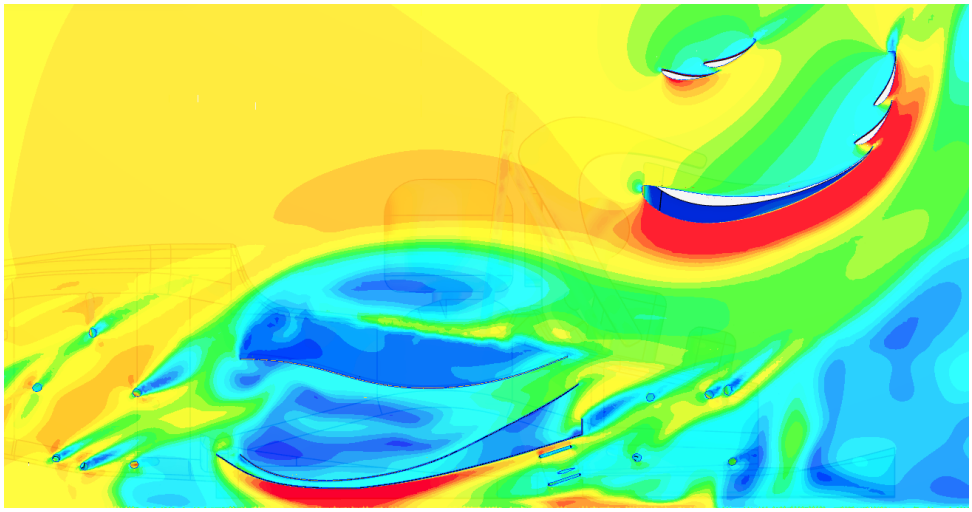

PICTURE 61. Flow pattern with sidepods, 350mm from the centreline.

Performance of the rear wing was improved with the sidepods, as a favourable eddy was generated at the top of the sidepod and the exit flow from the underbody was more focused. This in total moved aero balance from 54 % to considerably lower 50.2 %. Such a large-scale eddy in an open space was an uncertain improvement, as in reality its flow pattern could be largely different and would be greatly affected by the surrounding flows.

The diffuser with a higher angle at the middle section tweaked aero balance backwards by an additional 0.5 %. Velocity contours at the middle of the diffuser are shown in picture 62.

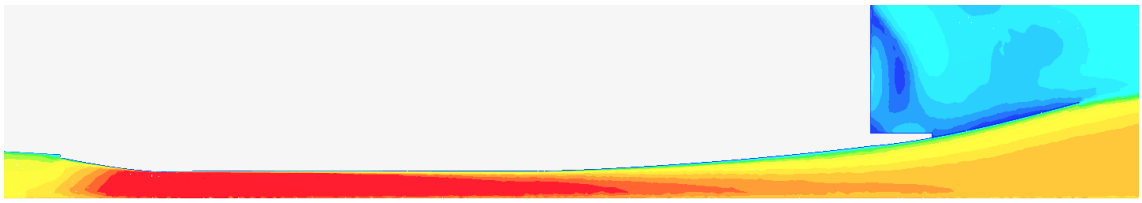

PICTURE 62. Multi-angle diffuser of BA 6.4, at the car centreline.

5.2.8 Iteration milestones

Iterations of the underbody and entire aero package were both following a proper trend for the balance and performance, determined at project plans. Results of the most relevant iterations (see appendix 5), were gathered into figure 30.

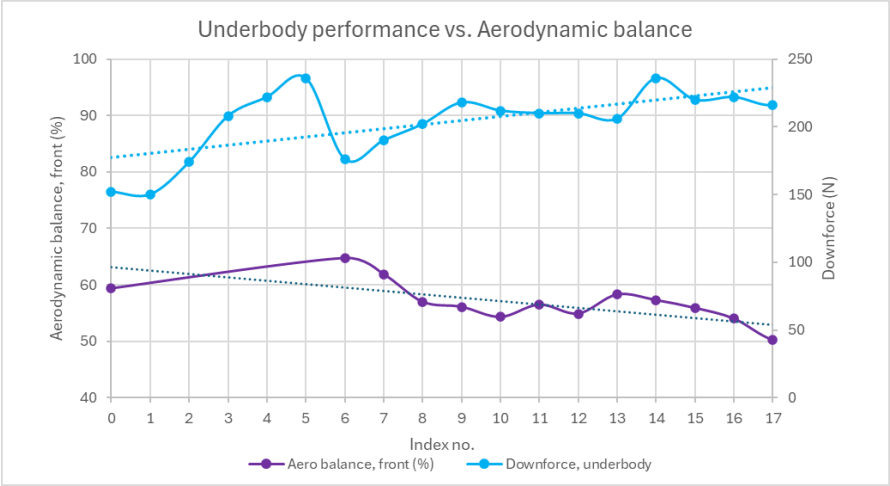

FIGURE 30. Development of underbody performance and aerodynamic balance.

The major decrease in performance was due to updates in simulation model and its setup, providing more accurate results, at index 6. Performance of the underbody, with lift & drag coefficients of the entire car were plotted (see appendix 5) together, visible in figure 31. It can be noted that the lift coefficient and underbody performance are mainly mutually aligned. The efficiency of the entire package was increased since lift coefficient was increased by 26% and drag coefficient by 11%.

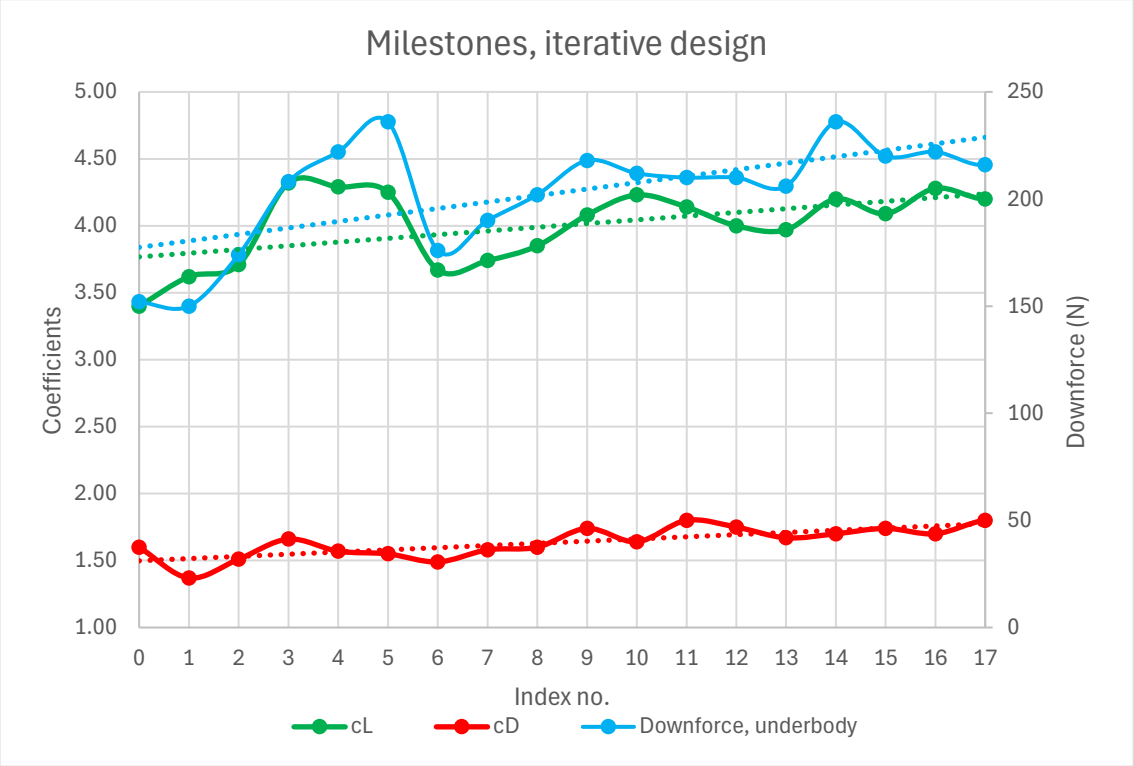

FIGURE 31. Milestones of iterative design.

5.3 Side tunnel adjustability

Since the side tunnel angle of attack was limited by the flow attachment and simultaneously power ground effect was limited by the angle of attack, a new option beneficial for both was studied. Adjustable angle for side tunnels was analysed. The BA 6.4 was used as a base model for the simulations, starting with stock option and proceeding until 6° of additional angle of attack, with an interval of 2°. Simulations were done both passive and active, with a 5 kg of thrust (see appendix 6).

Overview of the stock option and the additional 4° angle are shown in pictures 63 & 64.

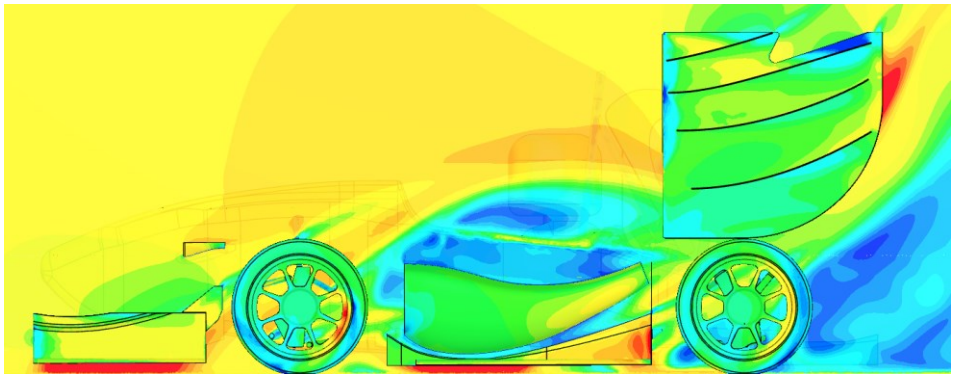

PICTURE 63. Passive run, without an additional angle.

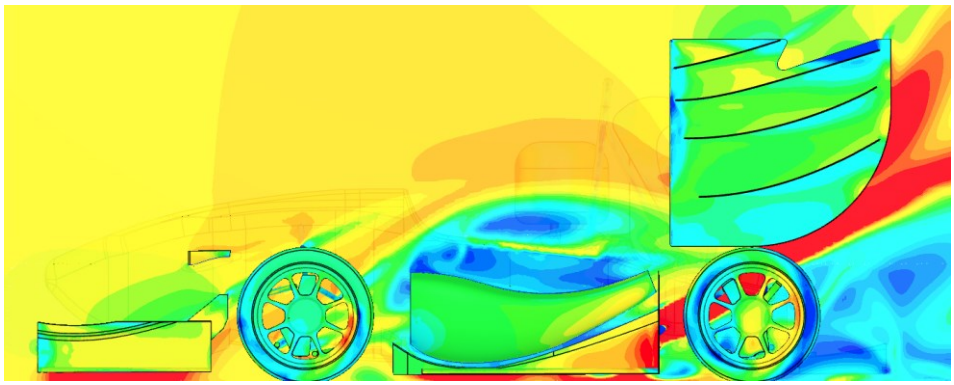

PICTURE 64. Active run (5kg), with an additional 4° angle.

Active underbody with increased angles improved the performance of the rear wing, improving aerodynamic balance, visible in figure 32.

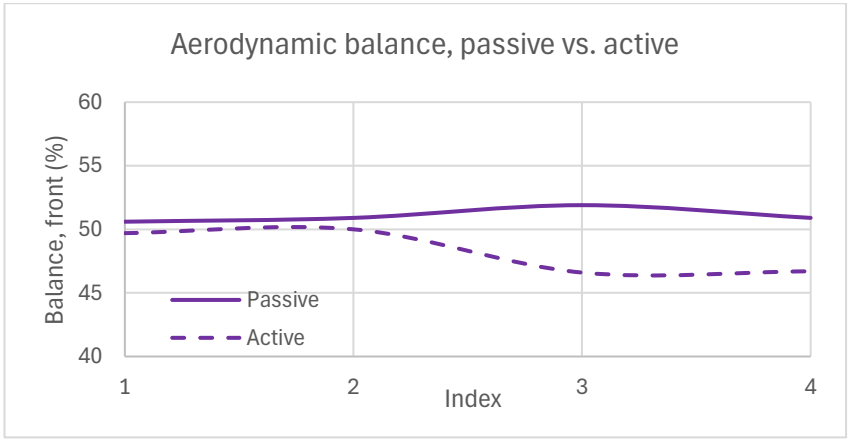

FIGURE 32. Aerodynamic balance, with passive & active runs.

With the passive runs, performance was decreasing at low rate when increasing the angle of attack due to flow separation. With the active underbody, a notable increase in downforce was reached with 4° of additional angle, see figure 33.

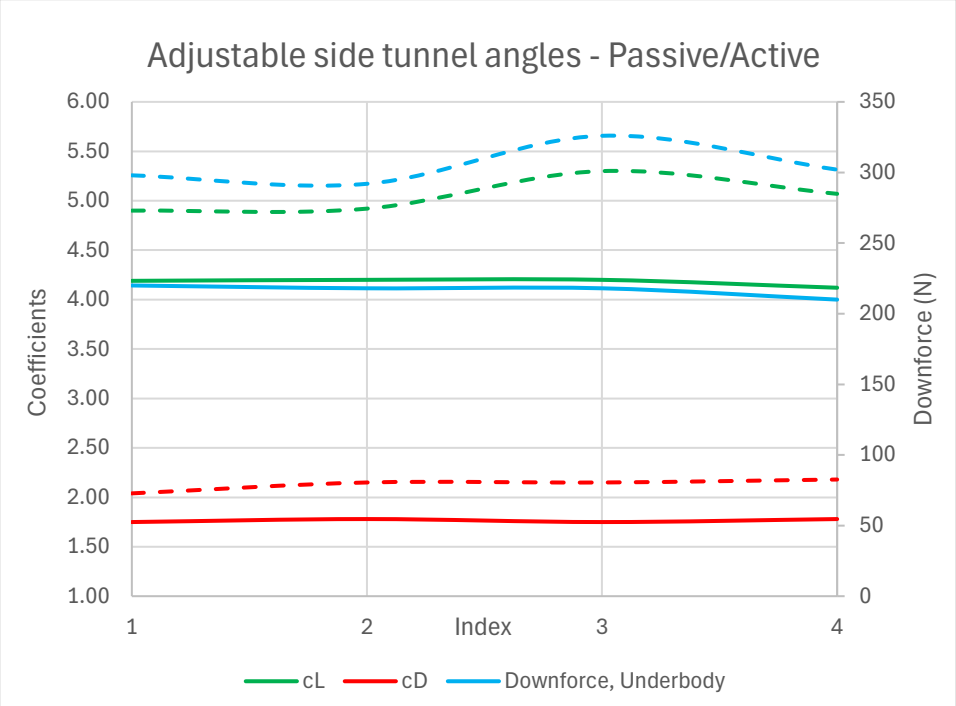

FIGURE 33. Active vs. passive runs with adjustable side tunnels. Active runs highlighted with dotted lines.

Even though passive runs with increased angles seemed to perform well in the simulations, they were recognized to still have inaccuracies. Therefore, adjustability was chosen to be included in the design. Additionally, adjustability would allow multiple side tunnel geometries and their flow patterns to be tested on the track, regardless of a limited testing season. Changeable side tunnel section was also considered, however multiple separate tunnel components would increase manufacturing costs and would complicate scrutineering in competitions. Thus, a single side tunnel component with adjustability option was chosen.

6 MECHANICAL DESIGN

After adjustable side tunnels were chosen to be pursued, mechanical design for the underbody was started. Since main scope of this thesis was on aerodynamic performance and its evaluation, mechanical design was reviewed in more general terms, focusing on the essential properties of the design. Therefore, detailed arguments about structural properties and materials engineering were excluded from this thesis.

6.1 Structural models

The entire aerodynamic package was designed to be manufactured mainly of carbon fiber composite structures, due to its superior strength-to-weight ratio. Carbon fiber reinforced polymers, abbreviated as CFRP, were used as solid sheets, as well as foam-core laminates. Aluminium was preferred with all inserts due to its low density, excluding threaded inserts with higher wear, which were designed from steel. All inserts, mounts, supports, and other sub-components were bonded, if not mentioned otherwise. Structural model of the underbody was created as a separate assembly, based on the characteristics of the simulation model part. The assembly consisted of four sub-assemblies, shown in picture 65.

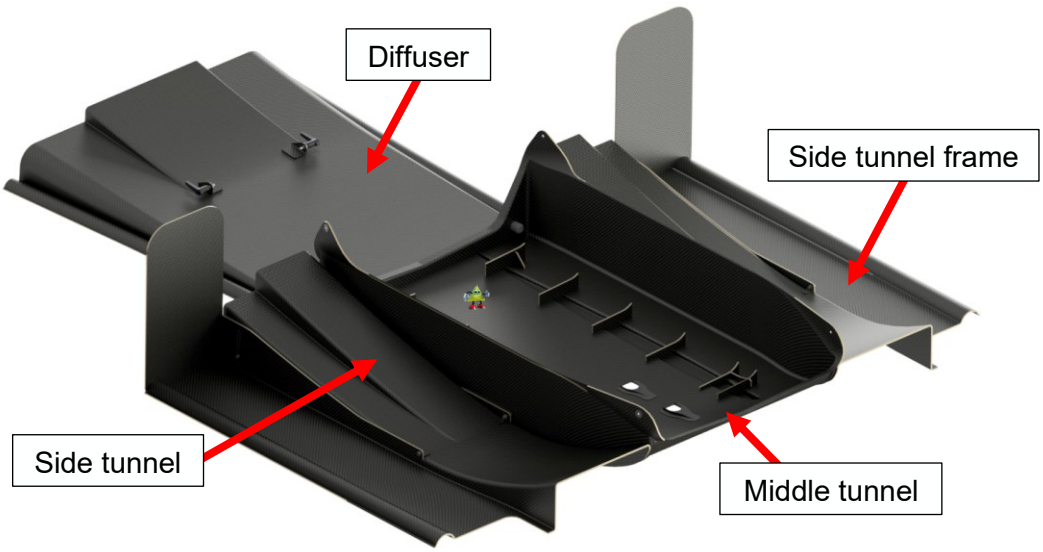

PICTURE 65. Structural assembly of the underbody.

6.1.1 Middle tunnel

The middle tunnel was shaped from its edges to fit the chassis geometry. Flanged aluminium inserts were added to the mounting points to prevent fiber abrasion. Due to the flat middle tunnel, additional support structures were required around the jacking points to transmit the forces properly to the chassis. Support structures were designed to be manufactured from foam core CFRP sheet and to be cut with CNC-milling. The middle tunnel is shown in picture 66. The positioning of the jacking points was determined by the chassis mounts and bolts to ensure sufficient clearances.

PICTURE 66. The middle tunnel.

Additional cross-braces were designed for the rear and front support structures to prevent buckling. Diffuser front mounting was located at the rear of the middle tunnel. The front mount and the rear cross-brace are visible in picture 67.

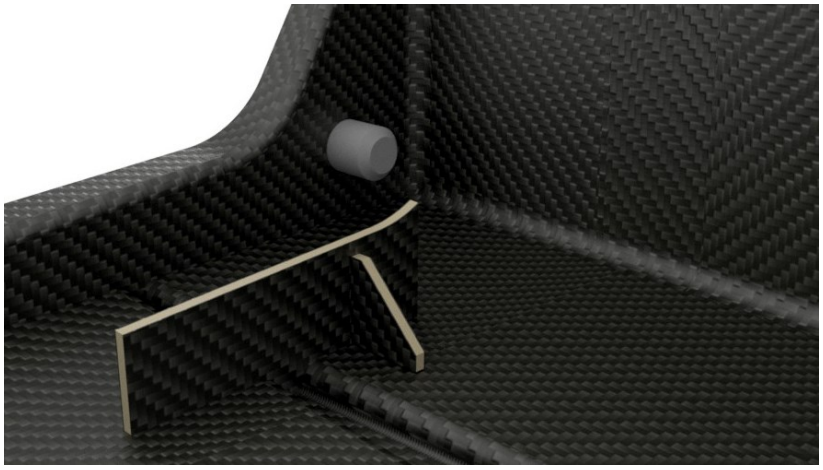

PICTURE 67. Diffuser front mount and the rear cross-brace.

According to the rules, at least two venting holes of 25 mm diameter must be in the lowest part of the chassis and through any structures covering them to prevent accumulation of liquids (Formula Student Germany 2024, 27). To suppress disturbances induced by these holes, NACA ducts were implemented in the middle tunnel (see picture 68). The ducts were designed to be 3D-printed from PLA for minimal manufacturing costs.

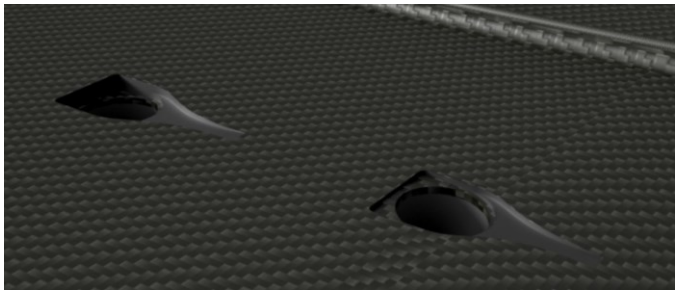

PICTURE 68. NACA ducts in the middle tunnel.

6.1.2 Side tunnels and frames

Side tunnel frames were designed as a separate part from the middle tunnel, for an improved manufacturability. Frame was designed to be laminated as a single part excluding the backplate, which was designed from a CFRP sheet. The right-side frame is shown in picture 69.

PICTURE 69. Side tunnel frame and the bonded backplate.

Grooves for side tunnel mounting were designed to be manufactured by hand. Inner wall of the frame was to be fixed to the middle tunnel by bonding. Side tunnel was to be laminated as a single part (see picture 70) and the side tunnel vane to be bonded from CFRP sheet (see picture 71).

PICTURE 70. Side tunnel.

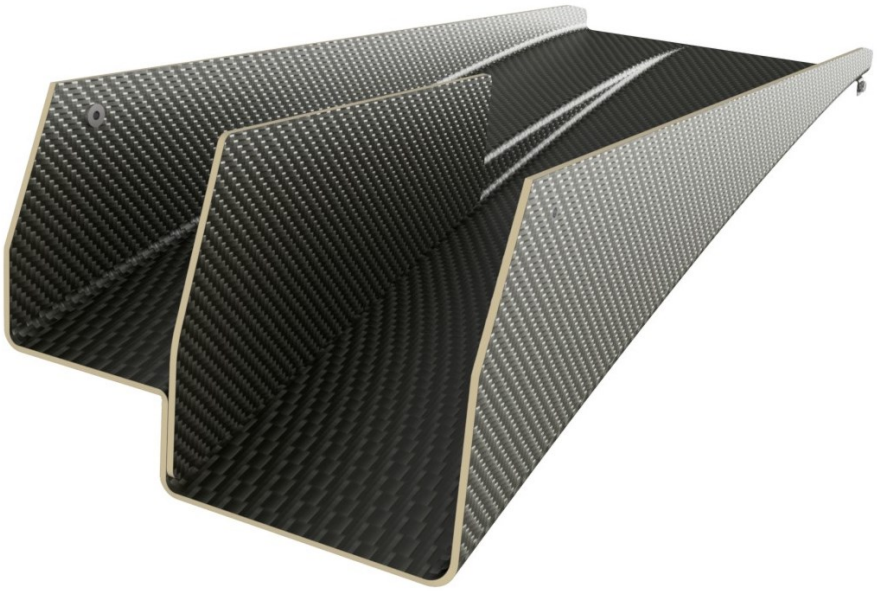

PICTURE 71. Side tunnel vane.

Side tunnel was to be mounted by using L-brackets and water-cut grooves, fastened with bolts. L-brackets with inserts were to be bonded to the side tunnels and threaded inserts to the frames. The inner side of the front mount included a spacer for a free rotation, and the outer side was to be tightened to desired position. This was due to the limited clearance around sidepods, when installed.

Additionally, an extension flap from flexible Diolen-CFRP hybrid was designed to the side tunnel front edge to seal the gap between the tunnel and the frame intake tunnel. This flexible flap was not modelled to make the model leaner to work with. The flap position and size are presented in picture 72.

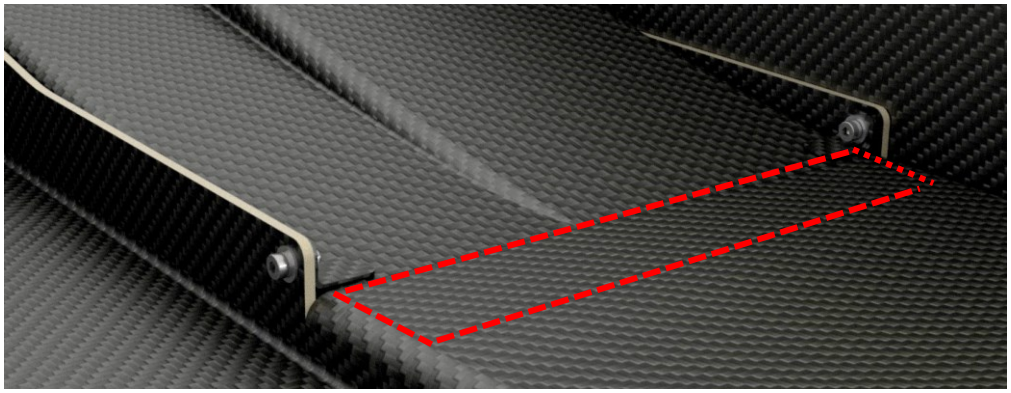

PICTURE 72. Side tunnel front mounting, the Diolen flap highlighted in red.

Side tunnel grooves were equipped with an additional adjustability for 1.5° lower angles than previously designed to act as a precaution in case of a weak flow attachment. The vanes and the edges of the side tunnel were trimmed to maintain required ground clearance in the lowest position as well. Side tunnel in a default position is shown in picture 73.

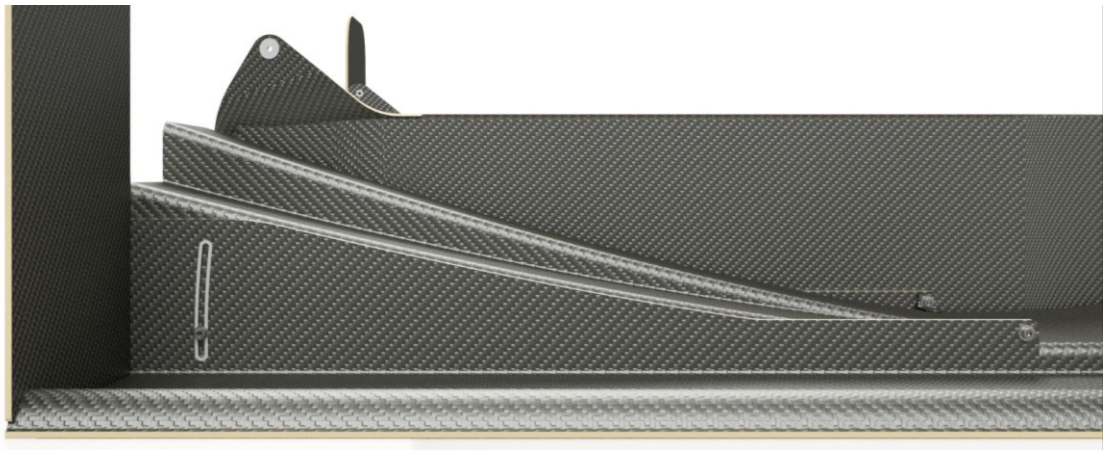

PICTURE 73. Side tunnel in the default position.

High angles were limited to the previously designed 6° for a quick configuration for active runs. Grooves were contoured with a constant radius for a stepless adjustment. Side tunnel in the elevated position is shown in picture 74.

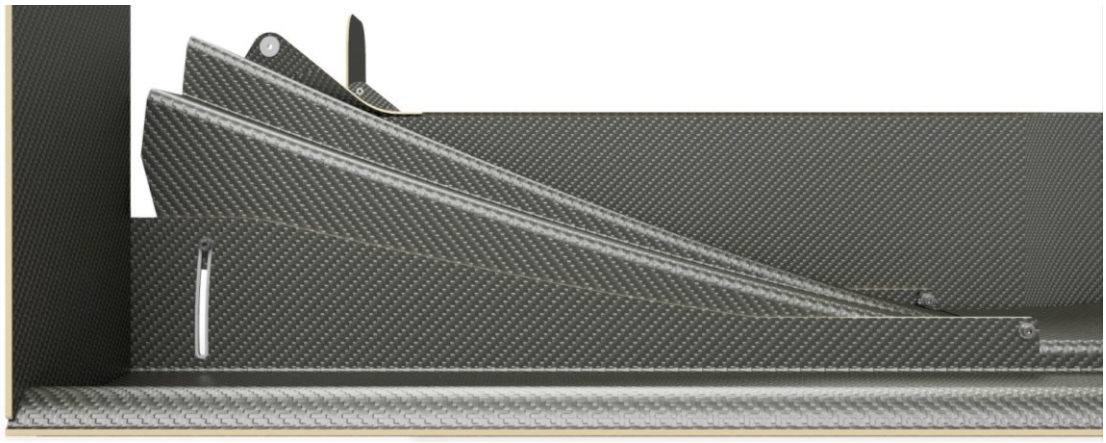

PICTURE 74. Side tunnel in the elevated position.

The open slot in the elevated position was assumed to have negligible effects with active runs, so no cover plates for the slots were designed.

6.1.3 Diffuser

Diffuser followed similar design aspects as previously presented components. However, the diffuser was designed with quick release mountings for the ease of maintenance. Overview of the diffuser is shown in picture 75.

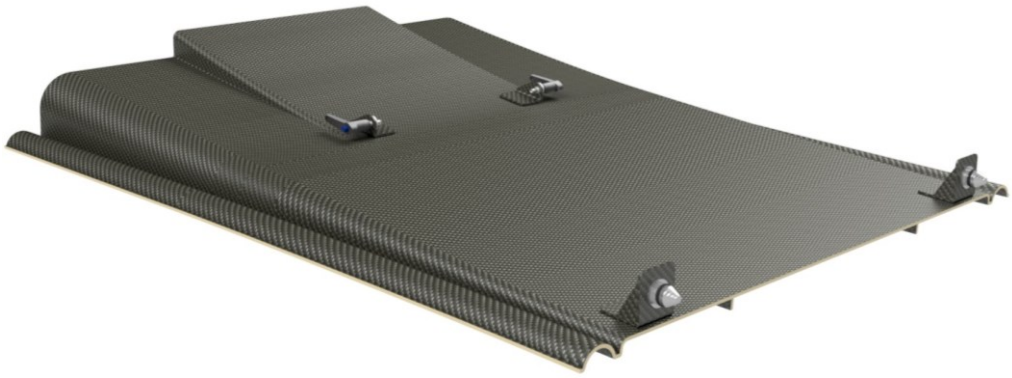

PICTURE 75. Diffuser.

The vanes on the diffuser were supported by the walls of the middle section, shown in picture 76.

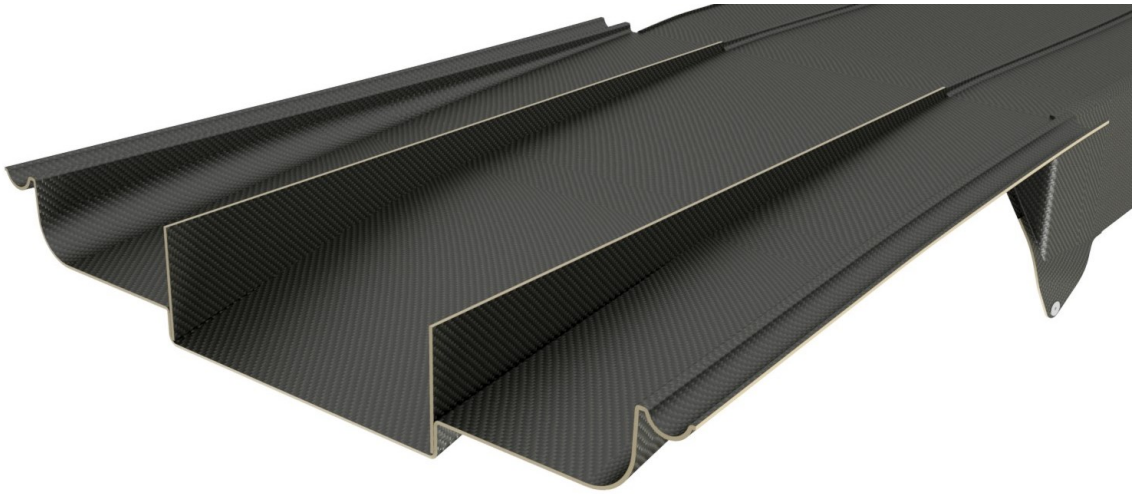

PICTURE 76. Diffuser vanes.

Front mounting of the diffuser consisted of a male piece with a backing plate, bonded to the L-bracket, and of a female piece, bonded to the middle tunnel, visible in picture 77. The front male piece was equipped with an O-ring for a tighter fitment. Additional CFRP braces were added to the L-brackets for stiffening.

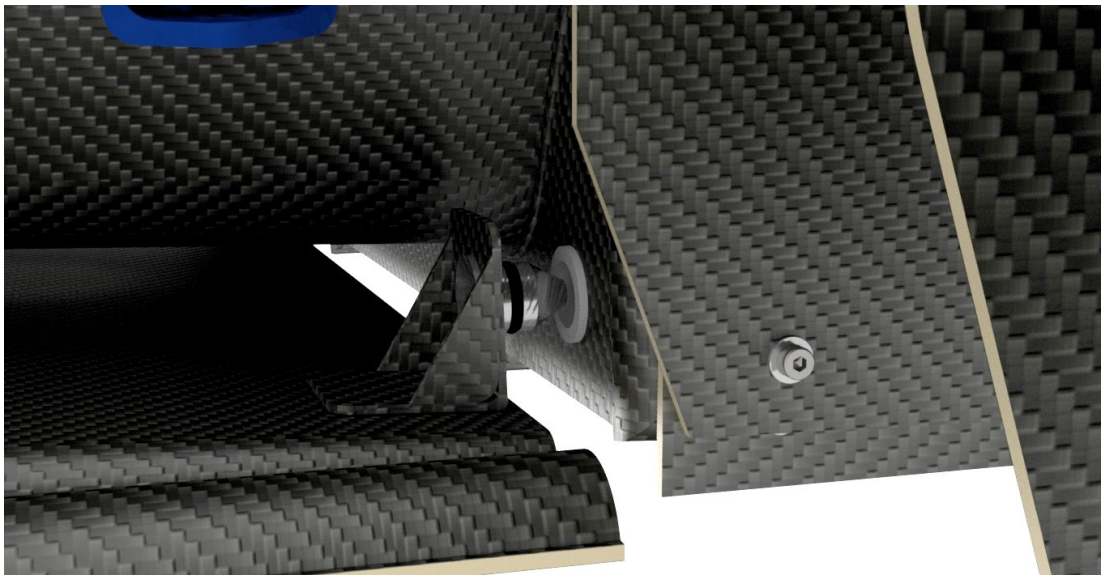

PICTURE 77. Diffuser front mounting (apart from the female piece for illustration).

The rear mounting included ball locks as a quick release system, visible in picture 78. The L-brackets were to be bonded to the diffuser and to the rear bulkhead of the chassis. Ball lock pins with the angled handles were chosen for the ease of release, as the muffler was in the close vicinity of the diffuser. However, any detailed suspension and powertrain components were hidden from the illustrative renders.

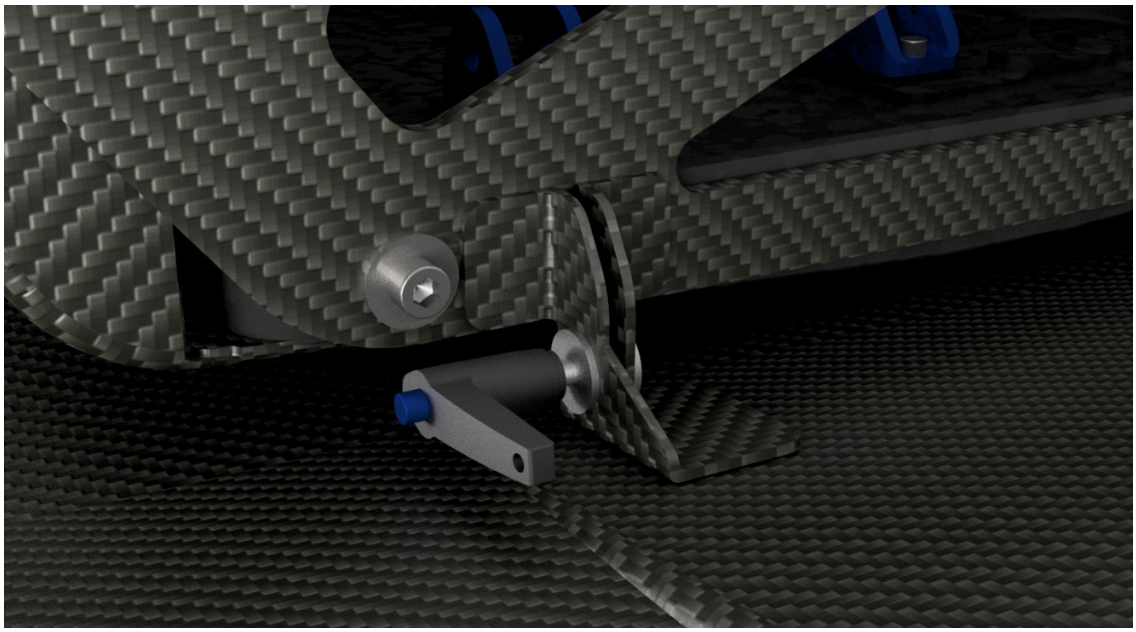

PICTURE 78. Diffuser rear mounting.

Both L-brackets were equipped with machined aluminium inserts for an accurate fitment for the ball locks.

6.2 Moulds

Minimum 1° of draft was used in all moulds on the relevant faces of the mould and more draft was preferred where possible. All moulds were designed to be manufactured from a low-density foam material for minimal material costs.

To ensure flush transition from middle tunnel to diffuser vanes, jacking points tapered off towards the rear. The rear sections of these were designed to be 3D-printed and bonded to the machined mould, as any thin walls of the foam mould

would break down during laminating. Middle tunnel and its printed sections are visible in picture 79.

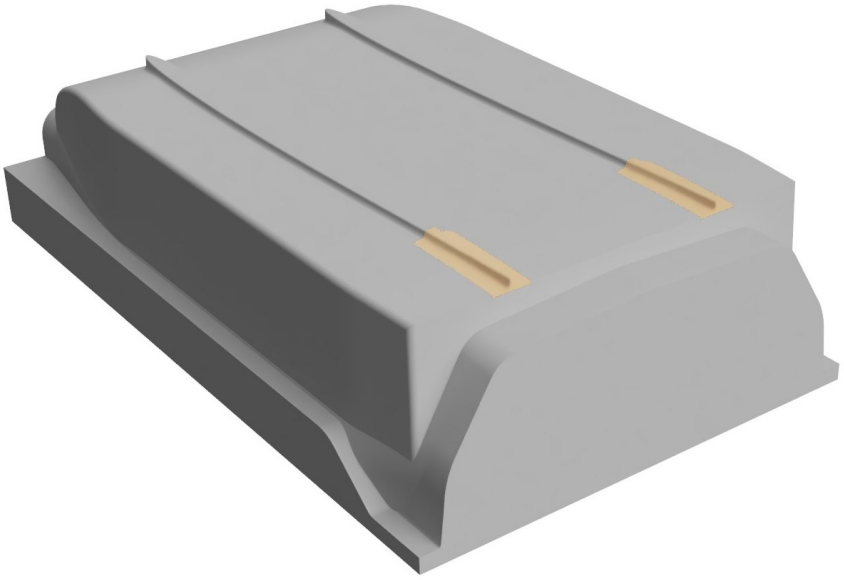

PICTURE 79. Middle tunnel mould. Printed sections highlighted in beige.

The diffuser mould did not require any additional changes, visible in picture 80.

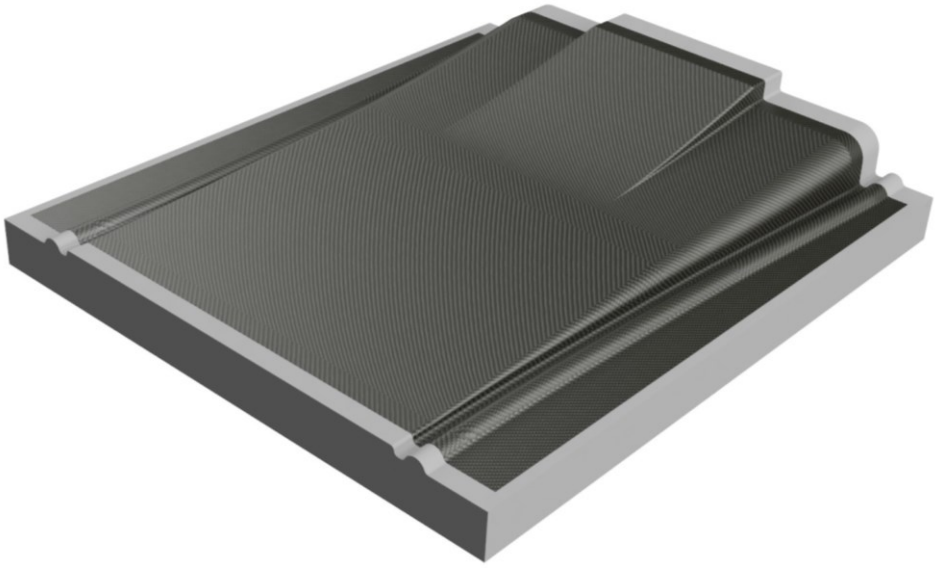

PICTURE 80. Diffuser mould.

Side tunnel mould was designed to have trimming lines machined by the tool radius, so additional offset was included at the edges of the final part, visible in picture 81.

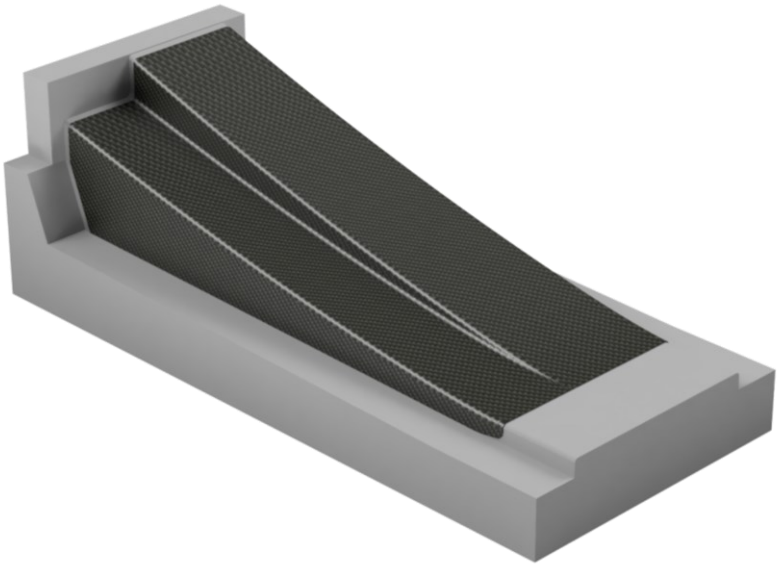

PICTURE 81. Side tunnel mould, right side.

Sharp edges of the side tunnel frame mould were designed to function as trimming lines for the manufacturer. The mould is shown in picture 82.

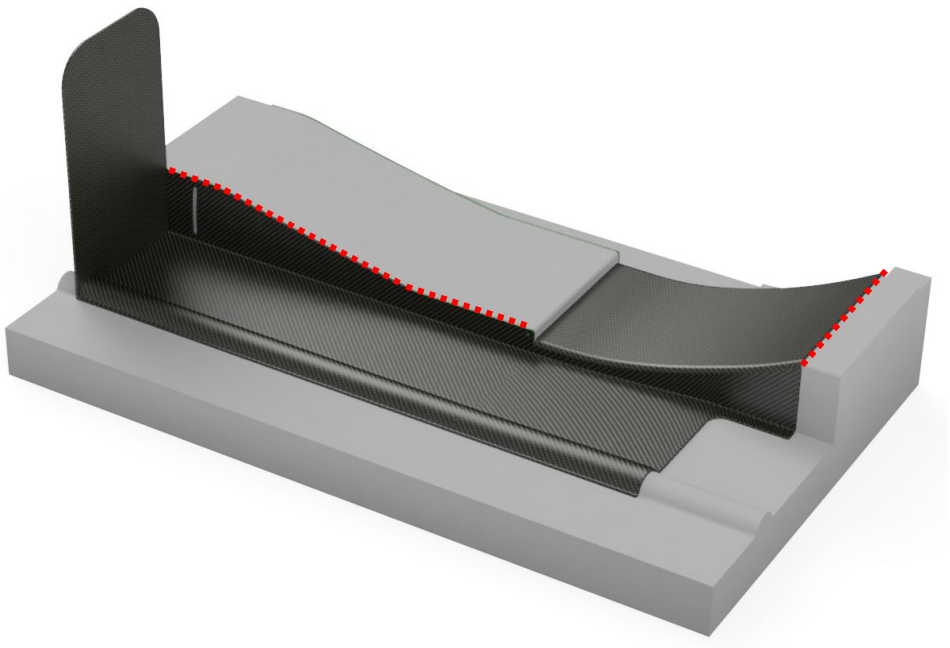

PICTURE 82. Side tunnel frame mould, right side. Red lines represent trimming lines.

7 RESULTS

Results presented in this thesis were noted to be indicative due to the ongoing development of the entire aerodynamic package and the unvalidated simulation setup. Therefore, the results reflect the data at the time and not the final performance of the prototype.

Since a more accurate vehicle model using a highly detailed software was still under development at the time, lap time simulations were performed with a simplified software, OptimumLap. The general data included total mass and driven type. Tire data consisted of rolling resistances and longitudinal & lateral frictions. Engine power was given based on a performance chart obtained from dyno. Gear ratios and transmission type were assigned as well. Track was given as a two-dimensional path, without changes in altitude. The path was created based on a real racetrack from a competition. While other factors remained unchanged, aerodynamic coefficients were changed according to the simulations.

After running the simulations, results can be analysed with several factors, such as throttle, brake, engaged gear and vehicle speed. The key values for comparing the entire aerodynamic performance were vehicle speed and the elapsed time.

Simulations were performed with the TFS23, TFS24, and the TFS24 with an underbody performance from TFS23, visible in figure 34. The TFS24 aero package with the TFS23 underbody resulted in a 0.54 s decrease in lap time. The TFS24 aero package performed with the lap time decreased by 1.5 seconds.

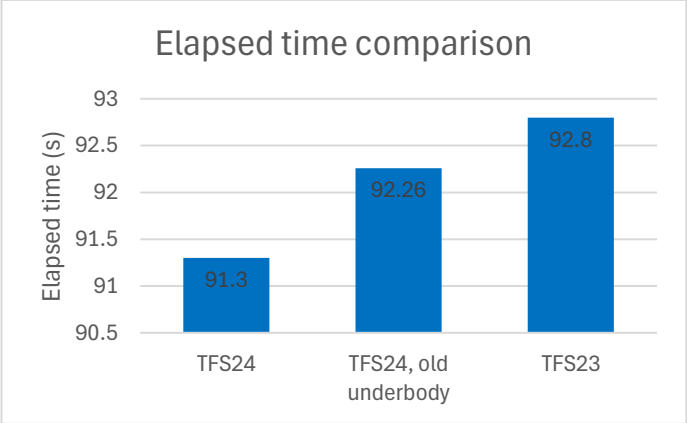

FIGURE 34. Elapsed time comparison.

The differences in vehicle speeds were minimal but significant in terms of the lap times. Vehicle speed contours in the track are presented in picture 83.

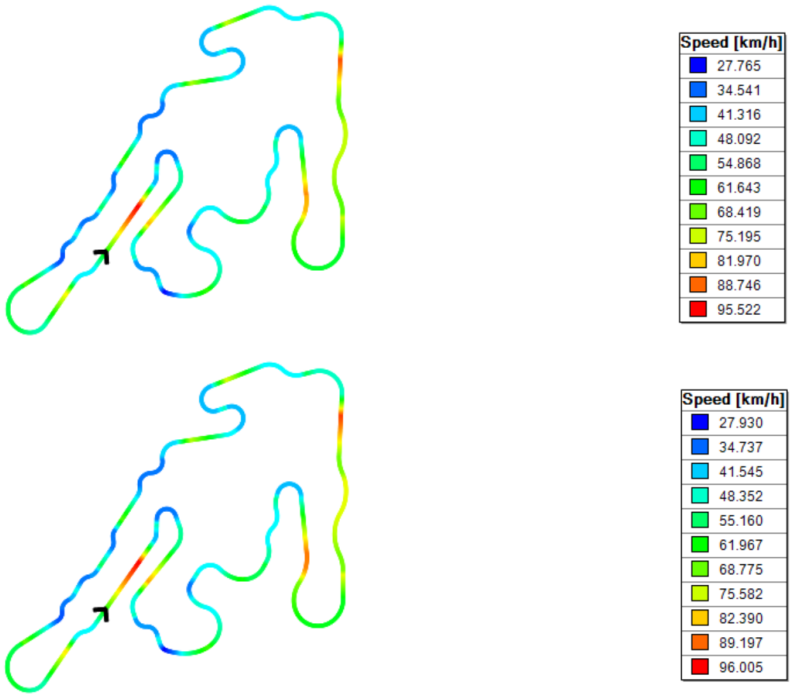

PICTURE 83. Speed contours, TFS23 (top) vs. TFS24 (bottom).

An example of lap times was gathered from the 2023 FS Austria competition. Results with differences are visible in table 6.

TABLE 6. Autocross results (Formula Student Austria, 2023).

Rank	Time (s)	Difference to 1st (s)	Difference to previous (s)
1	**54.561**	**0.00**	**0.00**
2	55.777	1.22	1.22
3	56.564	2.00	0.79
4	59.662	5.10	3.10
5	59.766	5.21	0.10
6	60.694	6.13	0.93
7	63.142	8.58	2.45
8	63.193	8.63	0.05
9	64.496	9.94	1.30
10	64.887	10.33	0.39

Rank	Time (s)	Difference to 1st	Difference to previous
1	**54.561**	**0.0%**	**0.0%**

2	55.777	2.2%	2.2%
3	56.564	3.7%	1.4%
4	59.662	9.3%	5.5%
5	59.766	9.5%	0.2%
6	60.694	11.2%	1.6%
7	63.142	15.7%	4.0%
8	63.193	15.8%	0.1%
9	64.496	18.2%	2.1%
10	64.887	18.9%	0.6%

Average difference to a previous competitor was 1.15 s among the top 10 participants. According to this, an increase in ranking would be uncertain but indeed probable with the TFS24 aerodynamic package.

Active runs of the TFS24 aero package with a thrust of 4 and 6 kg were simulated as well. As the analysis included only one lap to simulate the autocross event, thrusters were assumed to perform with max thrust for the entire event. Active run with the 4 kg thrust decreased lap time by an additional 0.53 seconds. The 6 kg run decreased TFS24 lap time by 0.92 seconds.

If all other factors would be assumed as constant, active runs with either 4 kg or 6 kg would potentially increase ranking in competitions. As the simulations were widely approximated and simplified, differences in lap times might increase or decrease with the more detailed simulation software.

8 CONCLUSIONS & DISCUSSION

The underbody reached most of its given goals with a significant improvement in performance, compared to its predecessor. The most critical deficiency from the previous protype, the flow attachment, was substantially improved. The adjustability option contributes to ensuring this success. Additionally, multiple configurations from the CFD can be compared to real conditions on the track with a single underbody assembly.

The disturbances induced by the side tunnel stall from previous design are eliminated, slightly improving the rear wing performance. Option to use the power ground effect with increased side tunnel angles further improve rear wing performance as well.

Aerodynamic balance for the new package is considerably improved but does not meet its given goals of the optimal 40% balance at the front axle. This matter was discussed with the suspension & steering department and will be compensated by the suspension settings to achieve desired handling characteristics.

More stable driving experience is achieved with the sectioned tunnels and the improved flow attachment. The performance of the middle tunnel was improved, which contributes to providing a more constant suction with varying conditions. However, aerodynamic performance should be evaluated with detailed yaw- & roll-simulations and track testing to confirm the stability through an entire event.

8.1 Aerodynamics development

Several challenges arose regarding simulation errors and convergence with the simulation model geometry. This was partially due to the complexity of body panel modelling and other poor geometries. To avoid these issues in the future, simulation model should be entirely remodelled using leaner design methods to allow a cleaner geometry for the mesher.

The research on the simulation model and CFD is already ongoing and showing a proper trend. Continuous development and documentation should be maintained with these matters.

Aerodynamic testing and validation have been non-existent until last season and has been a major shortage in the design events of competitions. As the testing time before competitions is limited, testing phase should be planned and prepared well in advance.

Active aerodynamics has shown its potential and should be further studied. Using thrusters in the side tunnels has its pros and cons and alternate concepts would be worthwhile exploring, such as placements around the diffuser or before the underbody. A more detailed approach to simulate thrusters could offer more pragmatic results.

Concepts dismissed in this thesis do not necessarily underperform but have been skipped for a variety of reasons. A short span of view indicated high potential in using multi-element underbody.

8.2 Mechanical development

The underbody and its subcomponents are still somewhat lacking in manufacturability, as the entire assembly consists of multiple contoured parts. An alternative approach to implementing side and middle tunnels to the chassis might considerably reduce manufacturing costs and time. Side tunnels could be mounted directly to the chassis, separately from the middle tunnel.

Next time the chassis is redesigned, regions of middle tunnel should be discussed together with the departments concerned. Bottom of the chassis could be used as a middle tunnel, eliminating the need for jacking points and separate moulds for aerodynamic middle tunnel.

Structural design of the aerodynamics has been done based on experience of the senior members of the team, thus the optimisation has sometimes been

absent. As the members of the team are constantly changing, some excessive and insufficient design and errors occasionally occur. The department head is ultimately responsible for the necessary education. However, the use of supportive software when designing lay-ups and structures might reduce the risk of human error.

To obtain trustworthy material data for the supportive software, comprehensive material tests should be performed with the layups of aerodynamic parts, in addition to chassis structural tests.

8.3 Further research

Results of the aerodynamic performance and its effect on lap times are coarse approximations with major uncertainty. Development of the CFD-simulations contributes to obtaining more reliable data on aerodynamic performance, but more detailed lap time simulations are needed to act as a proper guideline when determining goals and desired properties for aerodynamic packages in the future.

Comprehensive aerodynamic maps and detailed lap time simulations would highlight essential areas for development when driving at the limit and in other critical driving situations. The importance of this is emphasized as the driver training and overall performance of the vehicle is improved in the future.

REFERENCES

Airfoil Tools, n.d. Airfoil plotter. Read on 25.4.2024.
http://www.airfoiltools.com/plotter/index

Bernard, P. 2015. Fluid Dynamics. Cambridge: Cambridge Press.

Claudel, C. 2021. Quora. Read on 2.5.2024.
https://www.quora.com/Can-you-calculate-the-exit-velocity-of-a-jet-engine-and-are-the-thrust-equations-for-rockets-applicable-to-jet-engines

Ehirim, O. & Knowles K. & Saddington A. 2019. A review of ground-effect diffuser aerodynamics. Journal of fluids engineering 141 (2).

EPF, n.d. Mercury 90mm series. Mercury II 90mm (Narrow) 700KV-CCW (12S Li-Po). Read on 3.5.2024.
http://www.epf.com.tw/store/index.php?route=product/product&path=7_12_18&product_id=330

Fluid Mechanics 101, n.d. Calculators. Inflation layer calculator. Read on 2.5.2024.
https://www.fluidmechanics101.com/pages/tools.html

Formula Student Austria, 2023. Archive. Read on 12.5.2024.
https://fsaustria.at/past-events/2023-2/

Formula Student Germany. N.d. About, Concept. Read on 3.3.2024.
https://www.formulastudent.de/about/concept/

Formula Student Germany, 2024. Formula Student Rules v1.1. Read on 23.4.2024.
https://www.formulastudent.de/fsg/rules/

Formula 1 dictionary, n.d. Barge boards. Read on 15.4.2024.
https://www.formula1-dictionary.net/barge_boards.html

Forster, K. 2015. Why do diffusers have strakes/fins? Kyle Engineers 2.4.2015. YouTube.
https://www.youtube.com/watch?v=hgXni_LUgwc

Forster, K. 2021. Race Car Aerodynamics: The Definitive Course.
https://courses.jkfaero.com/

Houghton, L. & Carpenter, P. & Collicott, S. & Valentine, D. 2013. Aerodynamics for Engineering Students, 6th edition. Waltham: Butterworth-Heinemann.

Houghton, L. & Carpenter, P. & Collicott, S. & Valentine, D. 2015. Aerodynamics for Engineering Students, 7th edition. Waltham: Butterworth-Heinemann.

Katz, J. 1995. New Directions in Race Car Aerodynamics: Designing for Speed. Cambridge: Robert Bentley Automotive Publishers.

Katz, J. 2006. Aerodynamics of Race Cars. Cambridge: Robert Bentley Automotive Publishers.

Katz, J. & Morey, F. 2008. Aerodynamics of Large-Scale Vortex Generator in Ground Effect. Journal of Fluids Engineering 130 (7).

Leishman, G. 2024. Introduction to Aerospace Flight Vehicles, January 2024 Release. Florida: Embry-Riddle Aeronautical University.

Milliken, W & Milliken, D. 1995. Race Car Vehicle Dynamics. Warrendale: SAE International.

Schubeler, n.d. DS-51-DIA HST (93mm). Read on 2.5.2024. https://www.schubeler.com/product/ds-51-dia-hst/?v=f0aa03aaca95

SimScale, n.d. Tutorial: Incompressible Flow around a Formula Student Car. Read on 25.4.2024. https://www.simscale.com/docs/tutorials/formula-student-car/

SimScale, 2020. Documentation. Knowledge base. How to check convergence of a CFD simulation? Read on 4.5.2024. https://www.simscale.com/knowledge-base/how-to-check-convergence-of-a-cfd-simulation/

SimScale, 2023. Documentation, K-Omega turbulence models. Read on 29.4.2024. https://www.simscale.com/docs/simulation-setup/global-settings/k-omega-sst/

Somerfield, M. & Piola, G. 2020. Banned: The full story behind Brabham's F1 "Fan Car". Motorsport. Read on 16.4.2024. https://www.motorsport.com/f1/news/banned-tech-brabham-bt46b-fan/4808234/#gal-4808234-m0-niki-lauda-brabham-bt46b-15429240

Wang, J. 2008. Gurney Flap – lift enhancement, mechanisms and applications. Read on 11.4.2024. https://www.sciencedirect.com/science/article/pii/S0376042107000784#aep-section-id69

Zhang, X. & Toet, W. & Zerihan, J. 2006. Ground effect aerodynamics of race cars. Applied mechanics reviews 59 (1), 33-49.

APPENDICES

Appendix 1. Performance Chart, DS-51-DIA HST 93mm (Schubeler, n.d.)

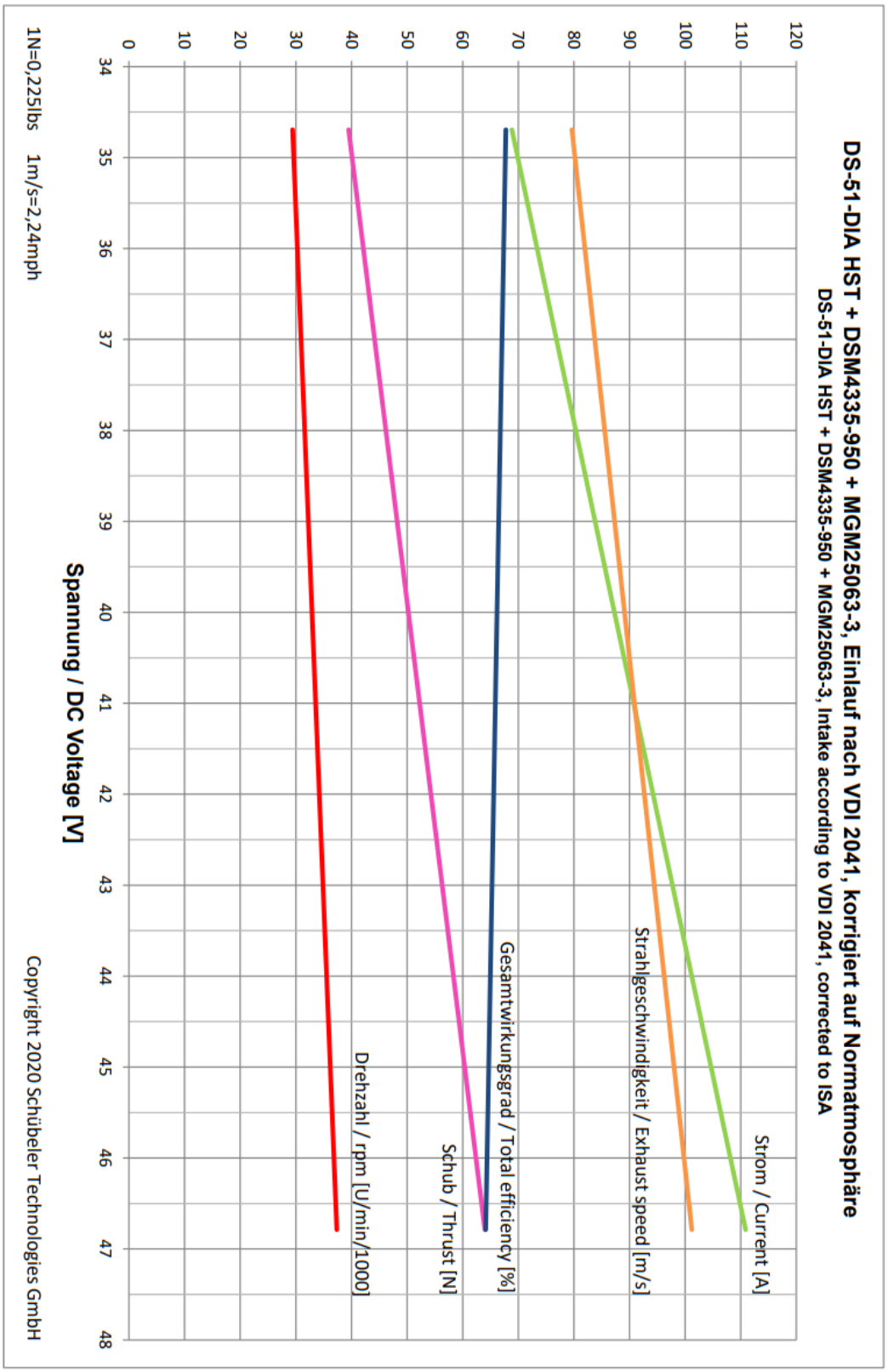

Appendix 2. SWOT-analysis, 1st & 2nd concept.

1st & 2nd concept, full-length & wide

Strengths	Weaknesses
• Choke point effortlessly focused on desired location, due to uniform tunnels • Ease of flow control, due to simplicity	• Challenging to reach higher angles of attack, due to space restrictions & limitations

Opportunities	Threats
• Vanes not optimised • Diffuser not optimised • Area for additional winglets, due to low profile • Power ground effect implemented on the rear-end	• Continuous tunnels more sensitive to distributing disturbances along full length • Optimising vanes and diffuser requires a large amount of effort

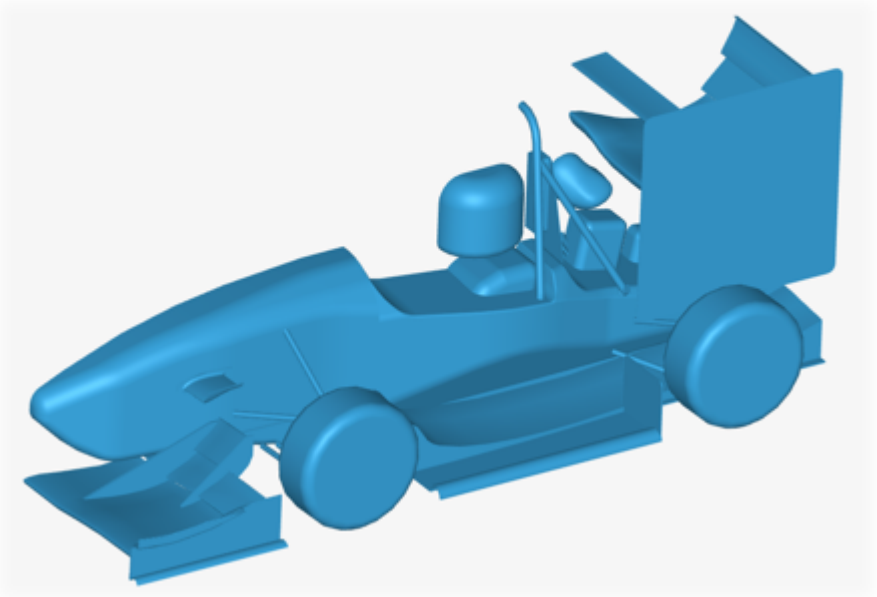

Appendix 3. SWOT-analysis, 3rd concept.

3rd concept, multi-element side wings

Strengths

- Official aerofoils can be used, with all the performance charts available
  - Selig & NACA, for example
- High camber with short length possible

Weaknesses

- Implementing sidepods will affect performance
- Requires clearance in Z-direction to perform properly
- Requires both lower and upper surfaces to be aerofoil-shaped

Opportunities

- Adding elements to the wing assembly
- Positions & angles not optimised
- Potential for a high downforce generation
- Possible to boost rear wing with high total camber

Threats

- Poor performance with sidepods implemented
- Complex moulds
- Laborious to optimise, due to complex side tunnel geometry

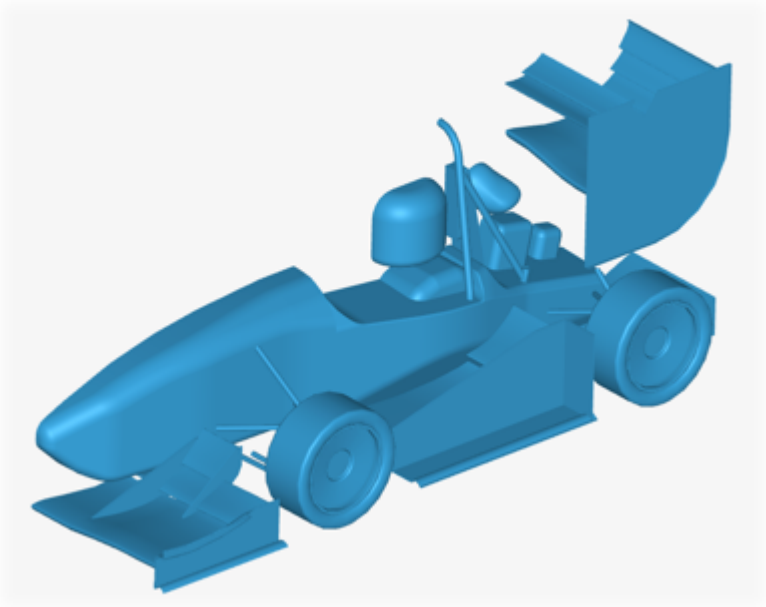

Appendix 4. SWOT-analysis, 4th & 5th concept.

4th & 5th concept, separate side and middle tunnels

Strengths

- Upper surface less sensitive to disturbances, compared to multi-element "tunnel"
- Simple geometry
- Easy to implement power ground effect to side tunnels

Weaknesses

- Challenging to energize the flow inside the tunnel
  - Sensitive to stall

Opportunities

- Sufficient performance with a reasonable amount of optimising
- Separated tunnels performing partially independently of each other
  - Prevents disturbances from spreading out from one tunnel to another

Threats

- Insufficient performance of side tunnels with low angle of attack
- Poor flow attachment with high angle of attack

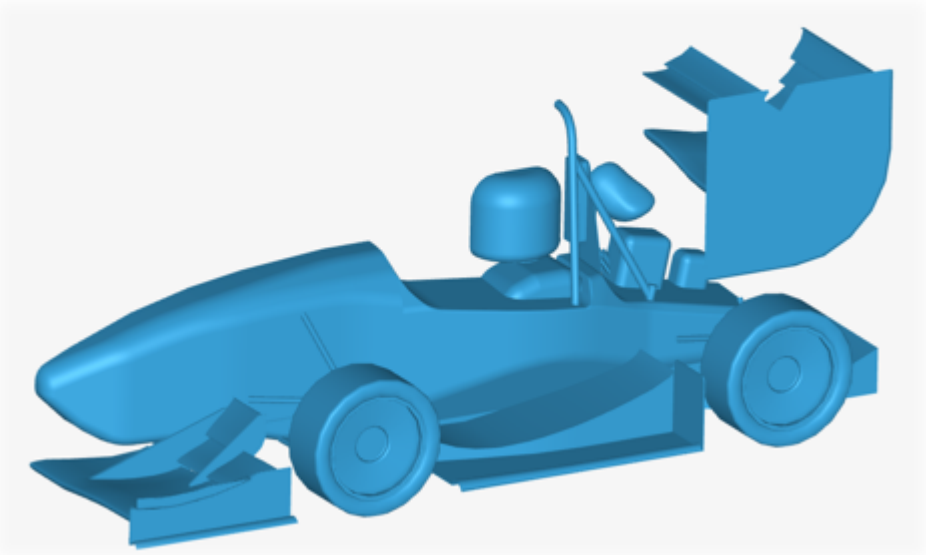

Appendix 5. Milestones of iterative design, performance table.

Index no.	Index	cL	cD	Downforce, total	Drag, total	Downforce, underbody	Aero balance, front (%)	Notes
0	Saana	3.40	1.60	447	210	152	59.4	TFS23 Aerodynamic package, updated simulation setup.
1	1st concept	3.62	1.37	476	180	150	-	Full length, wide tunnel.
2	1st concept	3.71	1.51	488	198	174	-	Full length, wide tunnel. Smaller sections added.
3	2nd concept	4.32	1.66	568	218	208	-	Low intake, curved vane on the inner tunnel.
4	3rd concept	4.29	1.57	564	206	222	-	Side wings with two elements.
5	4th concept	4.25	1.55	558	204	236	-	Side wings replaced with a single side tunnel.
6	4th concept	3.67	1.49	482	196	176	64.8	Same as above, updated simulation setup and detailed wheels.
7	5th concept	3.74	1.58	492	208	190	61.9	Higher intake height and aoa, updated vanes.
8	BA 1.1	3.85	1.60	506	210	202	57.0	Biggie Average, with additional vanes.
9	BA 1.3	4.08	1.74	536	228	218	56.1	Reconfigured vanes, lower diffuser.
10	BA 2	4.23	1.64	556	216	212	54.3	Second element added to the side tunnel.
11	BA 3.2	4.14	1.80	544	236	210	56.5	Additional diffuser, with a separate inlet.
12	BA 4 - aoa 5°	4.00	1.75	526	230	210	54.9	Simple diffuser, mid tunnel vane as jacking point.
13	BA 4 - aoa 7°	3.97	1.67	522	220	206	58.3	Same as above, with a higher side tunnel aoa.
14	BA 5	4.20	1.70	552	224	236	57.3	Separate side tunnel aoas (5 & 9°).
15	BA 5 - passive thruster	4.09	1.74	538	230	220	55.9	Same as above, passive thruster added.
16	BA 6.3	4.28	1.70	562	224	222	54.0	Flat middle tunnel, simplified diffuser.
17	BA 6.3	4.20	1.80	552	236	216	50.2	Same as above, added sidepods.
18	BA 6.4	4.28	1.78	562	238	228	49.8	Added sidepods, updated RW, multi-aoa diffuser.

Appendix 6. Adjustable side tunnels performance table, passive & active runs.

	Index	cL	cD	Downforce, underbody (N)	Balance, front (%)	Additional angle (°)
Passive	1	4.19	1.75	220	50.6	0
	2	4.20	1.78	218	50.9	2
	3	4.20	1.75	218	51.9	4
	4	4.12	1.78	210	50.9	6
Active	1	4.90	2.04	298	49.7	0
	2	4.92	2.15	292	50	2
	3	5.30	2.15	326	46.6	4
	4	5.07	2.18	302	46.7	6